Super-resolution microscopy of plasma membrane receptors and intracellular pathogens

Hochauflösende Mikroskopie von Plasmamembran Rezeptoren und intrazellulären Pathogenen

Doctoral thesis

for

a doctoral degree at the Graduate School of Life Sciences,

Julius-Maximilians-Universität Würzburg,

Section Biology & Biomedicine

Authored by:

Ralph Götz

from

Munich

Würzburg, 2020

Members of the Thesis Committee

Chairperson: Prof. Dr. Jörg Schultz

Primary Supervisor: Prof. Dr. Markus Sauer

Second Supervisor: Dr. Michael Hudecek

Third Supervisor: PD Dr. Sören Doose

Date of Public Defence: ……………………………………….…………

Date of Receipt of Certificates: ……………………………………

Summary

Humans tend to believe in what they can see with their own eyes. Hence, visualization methods like microscopy have always been extremely popular since their invention in the 17th century. With the advent of super-resolution microscopy, the diffraction limit of ~200 - 250 nm could be overcome to enable more detailed insights into biological samples. Especially the single molecule localization microscopy method dSTORM offers the possibility of quantitative bioimaging. Hereby, the repetitive photoswitching of organic dyes in the presence of thiols is exploited to enable a lateral resolution of 20 nm. Another, recently introduced super-resolution method is expansion microscopy (ExM) which physically expands the sample to increase the resolution by the expansion factor from four to even twenty. To enable this, the sample is embedded into a hydrogel, homogenized using an unspecific proteinase and expanded in distilled water. Within this thesis, both methods were used to shed light on plasma membrane receptor distributions and different bacterial and fungal pathogens.

In the first part of this thesis dSTORM was used to elucidate the "Receptome", the entirety of all membrane receptors, of the cell line Jurkat T-cells and primary T-cells. Within this project we could successfully visualize and quantify the distribution of the plasma membrane receptors CD2, CD3, CD4, CD5, CD7, CD11a, CD20, CD28, CD45, CD69 and CD105 with receptor densities ranging from 0.8 cluster/µm² in case of CD20 and 81.4 cluster/µm² for the highly abundant CD45 in activated primary T-cells at the basal membrane. Hereby, we could also demonstrate a homogeneous distribution of most receptors, while only few were clustered. In the case of CD3-clusters were detected in Jurkat T-cells and in primary activated T-cells, but not in naïve ones, demonstrating the activation of this receptor.

This was followed by the application of dSTORM to three different clinical projects involving the receptors CD38, BCMA and CD20 which are immunotherapeutic targets by monoclonal antibodies and CAR T-cells. In the first two projects dSTORM was applied to determine the receptor upregulation upon exposure of various drugs to MM1.S cells or primary multiple myeloma patient cells. This increase in membrane receptor expression can subsequently enhance the efficacy of therapies directed against these receptors.

Within the CD20-project, the superior sensitivity of dSTORM compared to flow cytometry could be demonstrated. Hereby, a substantially higher fraction of CD20-positive patient cells was detected by dSTORM than by flow cytometry. In addition, we could show that by dSTORM CD20-positive evaluated cells were eradicated by immunotherapeutic CAR T-cell treatment.

These studies were followed by whole cell super-resolution imaging using both LLS-3D dSTORM and 10x ExM to exclude any artifacts caused by interactions with the glass surface. In 10x ExM signal amplification via biotinylated primary antibodies and streptavidin ATTO 643 was essential to detect even single antibodies directed against the heterodimer CD11a with

standard confocal microscopes. Albeit probably not quantitative due to the process of gelation, digestion and expansion during the ExM protocol, even some putative dimers of the receptor CD2 could be visualized using 10x ExM-SIM, similar to *d*STORM experiments.

Within the second part of this thesis, expansion microscopy was established in bacterial and fungal pathogens. ExM enabled not only an isotropic fourfold expansion of *Chlamydia trachomatis*, but also allowed the discrimination between the two developmental forms by the chlamydial size after expansion into reticulate and elementary bodies.

Hereafter, a new α-NH$_2$-ω-N$_3$-C$_6$-ceramide was introduced enabling an efficient fixation and for the first time the use of lipids in both, 4x and 10x ExM, termed sphingolipid ExM. This compound was used to investigate the ceramide uptake and incorporation into the cell membrane of *Chlamydia trachomatis* and *Simkania negevensis*. For *Chlamydia trachomatis* the combined resolution power of 10x ExM and SIM even allowed the visualization of both bacterial membranes within a distance of ~30 nm.

Finally, ExM was applied to the three different fungi *Ustilago maydis, Fusarium oxysporum* and *Aspergillus fumigatus* after enzymatic removal of the fungal cell wall. In case of *Ustilago maydis* sporidia this digestion could be applied to both, living cells resulting in protoplasts and to fixed cells, preserving the fungal morphology. This new protocol could be demonstrated for immunostainings and fluorescent proteins of the three different fungi.

Zusammenfassung

Menschen neigen schon immer dazu, vor allem das zu glauben, was sie mit eigenen Augen sehen können, weswegen mikroskopische Methoden seit ihrer Erfindung im 17. Jahrhundert schon immer sehr beliebt waren. Mit der Einführung der hochauflösenden Mikroskopie konnte das Auflösungslimit von ~200 - 250 nm durchbrochen werden, was genauere Einblicke in biologische Proben ermöglichte. Insbesondere die Einzelmolekül-Lokalisations-Mikroskopie Methode *d*STORM bietet hierbei die Möglichkeit der quantitativen Bildgebung. Sie nutzt das wiederholte Schalten organischer Farbstoffe in Anwesenheit von Thiolen, was eine Auflösung von bis zu 20 nm möglich macht. Eine weitere kürzlich entwickelte hochauflösende Mikroskopiemethode ist die Expansionsmikroskopie (ExM), in welcher die Probe isotrop vier- bis sogar zwanzigfach vergrößert wird, womit sich auch die Auflösung um diesen Faktor vergrößert. Um dies zu ermöglichen, wird die Probe in ein Hydrogel eingebettet, mittels einer unspezifischen Proteinase homogenisiert und in destilliertem Wasser expandiert. Innerhalb dieser Arbeit wurden beide Methoden genutzt, um sowohl die Verteilung von Plasmamembran Rezeptoren als auch unterschiedliche bakterielle und pilzliche Pathogene zu beleuchten

Im ersten Teil dieser Arbeit wurde *d*STORM genutzt, um das „Rezeptom", die Gesamtheit aller Membranrezeptoren, sowohl von Jurkat T-Zellen als auch von primären Patientenzellen zu entschlüsseln. In dieser Arbeit konnten die Rezeptoren CD2, CD3, CD4, CD5, CD7, CD11a, CD20, CD28, CD45, CD69 und CD105 erfolgreich visualisiert und quantifiziert werden, welche Dichten von 0,8 Cluster pro µm² im Falle von CD20 und 81,4 Cluster pro µm² für den stark exprimierten Rezeptor CD45 in aktivierten primären T-Zellen auf der basalen Membran aufwiesen. Hierbei konnten wir für einen Großteil der Rezeptoren eine homogene Verteilung nachweisen, wohingegen nur wenige andere Rezeptoren Cluster zeigten. Für CD3 konnten sowohl in Jurkat T-Zellen als auch in aktivierten primären Zellen Cluster detektiert werden, was auf deren Aktivierung hinweist, wohingegen CD3 in naiven Zellen homogen verteilt war.

Im Weiteren wurde *d*STORM im Rahmen von drei klinischen Fragestellungen angewandt, in welche die Rezeptoren CD38, BCMA und CD20 involviert waren, die in Immuntherapien mit monoklonalen Antikörpern oder auch CAR T-Zellen adressiert werden. In den beiden erstgenannten Projekten wurde *d*STORM genutzt, um die Erhöhung der Rezeptoren-Expression nach Zugabe verschiedener Medikamente sowohl in der Zelllinie MM1.S als auch in primären Zellen von Patienten mit multiplen Myelomen zu bestimmen. Durch das CD20-Projekt hingegen wurde die überlegene Sensitivität von *d*STORM gegenüber der Durchflusszytometrie unter Beweis gestellt. Hier konnte verglichen mit der Durchflusszytometrie eine deutlich höhere CD20-positive Fraktion in Patientenzellen detektiert werden, welche nach Behandlung mit CD20 CAR T-Zellen eliminiert wurde.

Hierauf folgte hochauflösende Bildgebung ganzer Zellen sowohl mit LLS-3D *d*STORM als auch 10x ExM, um Interaktionen mit der Glasoberfläche ausschließen zu können. Bei 10x ExM wurde eine Signalamplifikation mittels Biotin und Streptavidin ATTO 643 benötigt, wonach sogar einzelne Antikörper, welche gegen den Heterodimer CD11a gerichtet waren, an einem herkömmlichen konfokalen Mikroskop detektiert werden konnten. Obwohl dies aufgrund der Prozesse von Gelierung, Verdau und Expansion während des ExM-Protokolls vermutlich nicht quantitativ ist, konnten sogar mutmaßliche Dimere des Rezeptors CD2 mit 10x ExM-SIM visualisiert werden, welche ähnlich in *d*STORM Experimenten auftraten.

Im zweiten Teil dieser Arbeit wurde die Expansionsmikroskopie für bakterielle und pilzliche Pathogene eingesetzt. ExM ermöglichte nicht nur eine isotrope vierfache Expansion von *Chlamydia trachomatis*, sondern auch die Unterscheidung der beiden Entwicklungsformen, der Retikulär- und Elementarkörperchen, aufgrund der Größe der einzelnen *Chlamydien*.

Anschließend wurde ein neues α-NH_2-ω-N_3-C_6-Ceramid eingeführt, was eine effiziente Fixierung und zum ersten Mal die Nutzung von Lipiden in 4x und 10x ExM ermöglichte, was wir Sphingolipid ExM nannten. Diese Verbindung wurde genutzt, um die Ceramid-Aufnahme und den -Einbau in die Zellmembran von *Chlamydia trachomatis* und *Simkania negevensis* zu untersuchen. Im Falle von *Chlamydia trachomatis* wurde die hohe Auflösung von 10x ExM mit SIM kombiniert, was die Visualisierung beider bakterieller Membranen in einem Abstand von ~30 nm ermöglichte.

Hiernach wurde ExM bei den drei unterschiedlichen Pilzen *Ustilago maydis, Fusarium oxysporum* und *Aspergillus fumigatus* nach enzymatischen Verdau der pilzlichen Zellwand angewandt. Im Falle von *Ustilago maydis* Sporidien konnte der Verdau sowohl an lebenden Zellen, was in Protoplasten resultierte, als auch an fixierten Zellen verwendet werden, was die Morphologie erhielt. Mittels dieses neuen Protokolls konnten sowohl Immunfärbungen als auch fluoreszierende Proteine der drei genannten Pilze expandiert werden.

Contents

Contents

1 Introduction

1.1 Fluorescence microscopy

After its invention by Antonie van Leeuwenhoek in the late 17th century light microscopy has been one of the most widely applied tools in biology. Standard transmission light microscopy however, has always been suffering from a relatively poor contrast. To address this, techniques like phase contrast microscopy have been introduced, which improved, but never solved this issue. Since the discovery of fluorescence by George Stokes in 1852, its physical explanation by Alexander Jablonski and especially the discovery of the fluorescent protein GFP (Shimomura, Johnson and Saiga 1962), fluorescence has revolutionized research and particularly fluorescence microscopy has become an extensively used tool to study cellular structures and processes. Fluorescence allows a highly selective signal detection with an excellent contrast between signal and background which makes it an ideal tool that is used not only in microscopy, but also in flow cytometry, genetic analysis and molecular diagnostic. The requirement that a molecule can exhibit fluorescence is a delocalized π-electron-system. These molecules, called fluorophores, possess electrons that remain in an unexcited ground state (singlet state S_0) until they are excited by light with the fitting wavelength to reach energetically higher states (singlet state S_1 or S_2). In these states the electrons lose a part of their energy either *via* vibrational relaxation (VR) within this energy state or *via* internal conversion (IC). When falling back to the ground state S_0 the electrons' energy is emitted in the form of light, the fluorescence. Due to the earlier energy loss, the electrons emit less energy than absorbed in the beginning and the emission light is red-shifted. Hereby, this red-shifted Stokes-shift from the excitation to the emission spectrum makes it possible to separate those two light paths by optical filters achieving a high contrast. In few cases, the excited molecules might also transit to the triplet state (T_1) by radiationless intersystem crossing. From this state the electrons can return to the ground state S_0 by emitting phosphorescence, a long lived light emission that is typically even more red-shifted (Fig. 1) (Sauer et al. 2018, Lakowicz 2006).
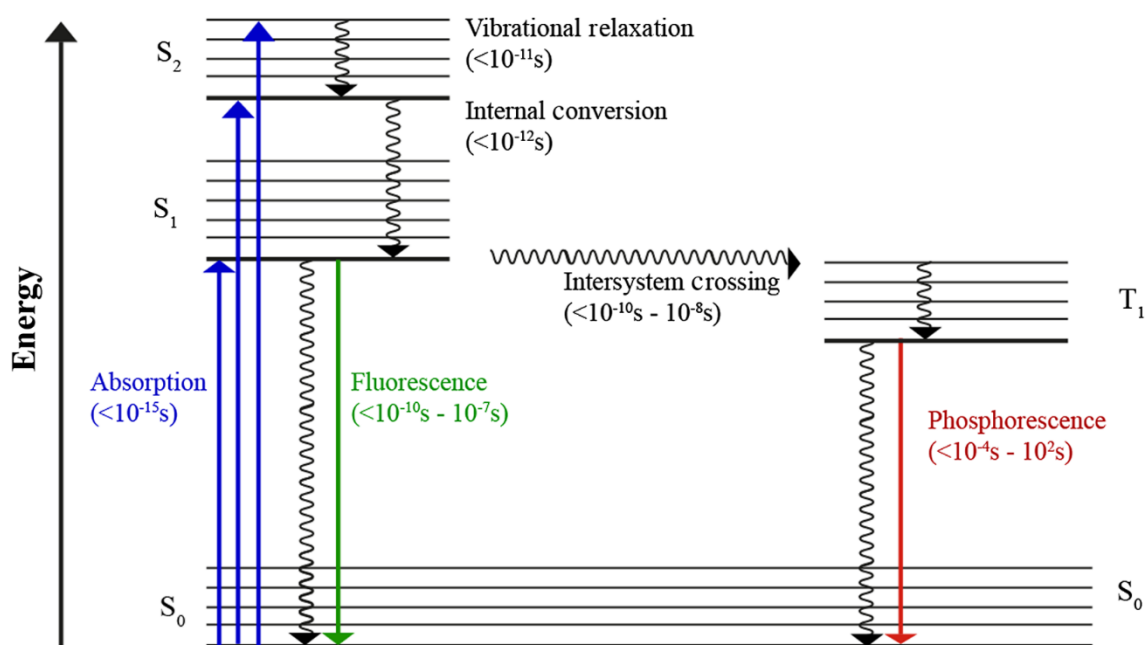
Figure 1 Jablonski diagram of the crossing between the singlet states (S_0-S_2) and the triplet state (T_1). After absorption electrons are excited from the ground state S_0 into the energetic higher S_1- and S_2-states. Here, electrons lose energy *via* relaxation or internal conversion to return to the ground state (S_0) by the emission of fluorescence. Alternatively, electrons enter the triplet state *via* intersystem crossing and return to the ground state by the emission of phosphorescence. With permission from Sauer et al. 2018.

To exploit fluorescence ideally, countless fluorescent proteins, quantum dots and organic dyes have been developed ranging from cyanines to rhodamines and oxazines with spectra all over the visible range (Dempsey et al. 2011, Pinaud et al. 2006). According to the user's needs also specialized proteins and dyes were designed with distinct properties like an improved photostability and brightness (Grimm et al. 2016, Michie et al. 2017) or tuned photophysical behavior (Uno et al. 2014).

These dyes were also labeled to a variety of different molecules among them antibodies, biotins, self-labeling tags (Los et al. 2008, Cole 2013) and oligonucleotides that offer a huge library to stain the molecule of interest.

Due to the wave nature of light, the achievable resolution has been limited by the diffraction of light to ~200 nm, as already published by Ernst Abbe in 1873 (Abbe 1873). Hereby, after imaging two lines through a periodic grid with a microscope, Abbe postulated that a light microscope's resolution or the distance between these two still resolvable lines (d) depends on the numerical aperture (NA) of the used objective and the emission wavelength (λ). He described this relation with the following equation (Abbe 1873, Verdaasdonk et al. 2014):

$$d = \frac{\lambda}{2NA} \qquad (1)$$

This physical limitation makes it impossible to resolve structures below 200 nm. Hence, the so called diffraction limit leaves a huge gap between the imaged structures and the "ground truth". Rayleigh addressed further questions concerning resolution in light microscopy and defined within his Rayleigh criterion the minimum distance between two single light emitting spots to still be resolved. Hereby, he used two airy discs, focused and diffraction limited light sources with concentric rings of decreasing intensities around it, and overlapped them until they could not be distinguished as separate spots anymore. He defined that the maxima of these two diffraction limited spots may not be closer to each other than the radius of the single spots or the maximum of the first spot may only coincide with the minimum of the other (Fig. 2). This minimal resolvable distance between two spots (d) can also be described by the following equation (Rayleigh 1903):

$$d = \frac{1.22 * \lambda}{2NA} \qquad (2)$$
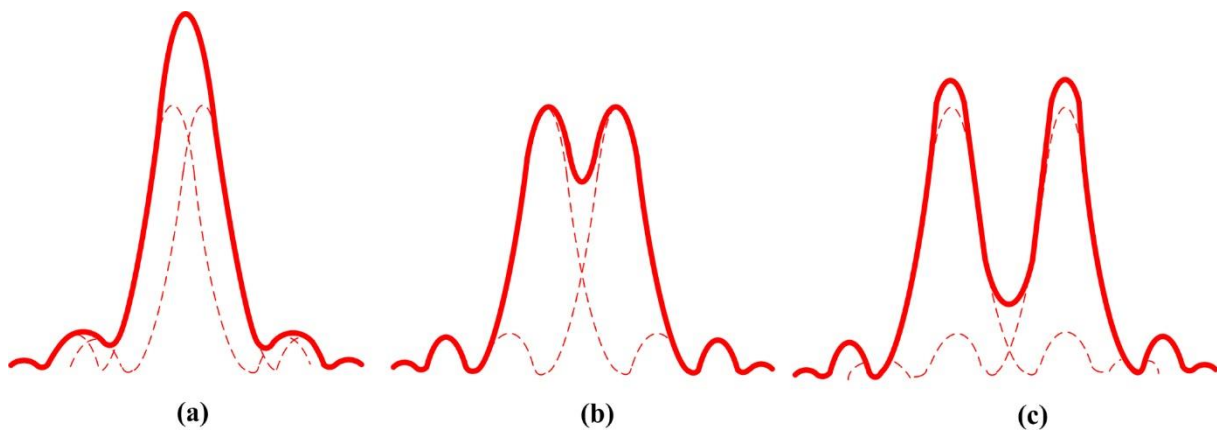
Figure 2 Schematic overview of the Rayleigh criterion. (a) Two overlapping light sources cannot be separated. (b) Two light sources overlap but can still be resolved because the maxima of the two spots are not closer to each other than the radius of each spot. (c) Two light sources overlap only partially and can be resolved. With permission from Li et al. 2012.
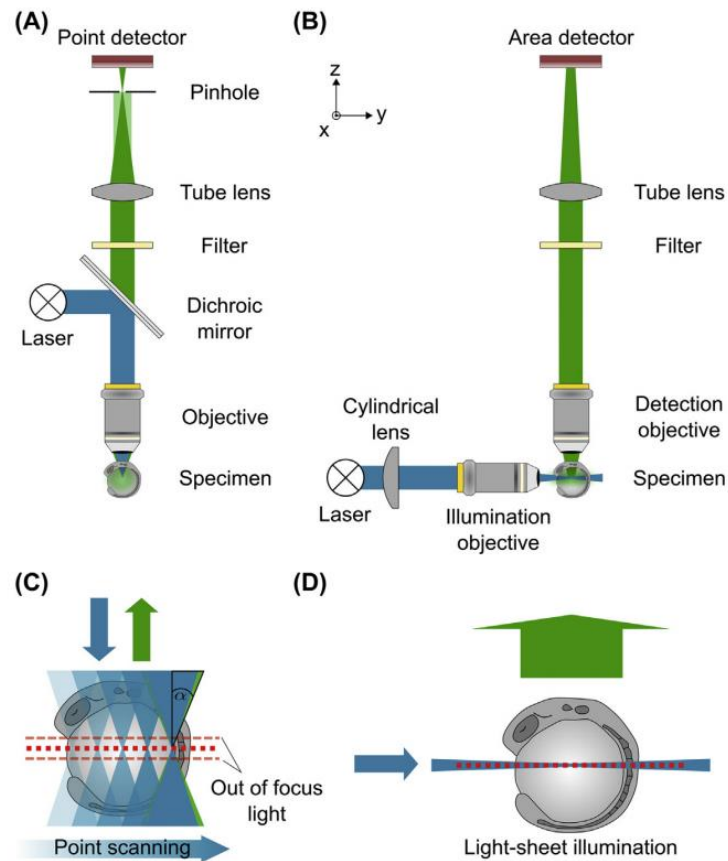
1.2 Confocal scanning and light-sheet microscopy

One of the most widespread fluorescence microscopy methods is the confocal laser scanning microscope (CLSM). Here, the excitation beam is reflected by a dichroic mirror through the objective into the sample from underneath to excite the fluorophores and is focused at the sample. For image acquisition the sample is scanned point by point. The red-shifted fluorescence is then transmitted by the dichroic mirror and focused by a tube lens at the detector. To minimize signals from excited dyes in other planes a pinhole is placed in front of the detector. This simple and robust microscopy method suffers, however, from severe phototoxicity in live-cell experiments and partially strong photodamage when imaging for longer periods of time for e.g. 3D-stacks (Fig. 3).

To address this, light-sheet microscopes (Huisken and Stainier 2009, Stelzer 2015) like the lattice light-sheet (LLS) microscope were developed. Hereby, typically two objectives are positioned orthogonally to each other to use one objective for illumination and the other one for detection. This separation of two light paths in two objectives enables the illumination with a narrow sheet of light from the side contrary to conventional widefield or point scanning approaches which illuminate the whole sample. Because solely the fluorophores in the detection plane are excited by the light-sheet, a pinhole like in CLSM is also unnecessary (Fig. 3). Among the light sheets, the lattice light-sheet stands out due to its superior imaging speed and decreased phototoxicity allowed by an ultrathin light sheet (Chen et al. 2014). The combination with fast sCMOS cameras (100 frames/s) allows the imaging of large 3D-volumes at an impressive speed. With an increasing speed also the collected data amount drastically increases which makes especially the data processing extremely time consuming. To improve the resolution of a LLS, it has already been combined with the super-resolution method point accumulation for imaging of nanoscale topography (PAINT) to image dividing cells and even the periphery of small embryos (Legant et al. 2016).

Figure 3 Differences between point scanning and light-sheet illumination. (A) In confocal systems the laser light is directed focused into the sample *via* a dichroic mirror. The emission is collected with the objective and transmitted through the dichroic mirror. After focusing by the tube lens the light is detected and light from other planes is excluded by a pinhole. (B) In light-sheet microscopy a cylindrical lens generates a light-sheet in the focal plane of the other detection objective. The sample is solely illuminated by the light-sheet resulting in fluorescence exclusively within the focal plane. The collected emission is spectrally filtered and focused on the detector. (C) In confocal scanning microscopes the whole sample is scanned point by point. However, also fluorophores from other planes are excited resulting in out of focus light which is reduced by a pinhole. (D) Light-sheet microscopy by contrast, illuminates solely one plane from the side. Moreover, the whole plane is excited and detected at once enabling high speed imaging. With permission from Kromm 2016.

1.3 Super-resolution microscopy

During the last decades many optical methods have been developed to overcome the diffraction limit and to initiate the age of super-resolution imaging. Either defined illumination patterns are used like in structured illumination microscopy (SIM) (Gustafsson 2000) and stimulated emission depletion (STED) (Hell 2007) or the single emitters are stochastically separated in time like in photoactivated localization microscopy (PALM) (Betzig et al. 2006) and direct stochastic optical reconstruction microscopy (dSTORM) (Heilemann et al. 2008). Hereby, each method has its own limitations and advantages considering acquisition time and final resolution.

In SIM a modified widefield microscope is used to apply a patterned illumination, usually stripes, to excite the dyes. The fluorescence signal is hereby collected in various patterns and orientations. Due to the interaction of the sample's fluorescence emission and the excitation grid, moiré fringes are formed which allow the recording of high frequency information at lower spatial frequencies. The information of various images can then be separated computationally in Fourier space into information of higher and lower frequencies. After moving this separated information into the right position, a super-resolved image with a twofold improved resolution can be generated. While solely doubling the lateral and axial resolution, SIM is fully compatible to live-cell experiments with up to four colors and does not need specialized fluorophores like in other super-resolution methods besides relatively stable dyes (Wegel et al. 2016, Heintzmann and Huser 2017).

STED by contrast is a deterministic technique that applies additionally to a conventional excitation laser also a depletion laser, a "donut" which efficiently depletes fluorescence in the area of the depletion laser. The sample is then scanned like in confocal scanning microscopes point by point, resulting in a maximal achievable resolution between 20 nm and 50 nm (Blom and Brismar 2014).

PALM and dSTORM on the other hand are single molecule localization microscopy (SMLM) methods. In PALM fluorescent photoconvertible proteins like mEos (Zhang et al. 2012) are activated by a short UV-light pulse. This ensures that only few, separated molecules are activated which can be localized and consequently bleached. A new pulse will activate new proteins and this procedure is repeated until all proteins were activated and subsequently localized. Due to the limited brightness and the activation mechanism of fluorescent proteins in many cases the resolution is slightly worse than in dSTORM and the acquisition times are much longer.

Contrary, *d*STORM exploits the stochastic repeated blinking of some organic dyes in the presence of reducing agents like thiols and achieves a lateral resolution of 20 nm (Fig. 4 a). Here, dyes are excited with high laser powers to force many dye molecules to enter the triplet state from which they can be effectively reduced by the widely used β-mercaptoethylamine (MEA) to enter a stable non-fluorescent radical state. Some dyes like ATTO 655 can even be reduced one more time into its leuco form (van de Linde et al. 2011). Oxygen on the other hand is able to interact with dyes in its triplet and radical state to return them into their ground state (Fig. 4 b).
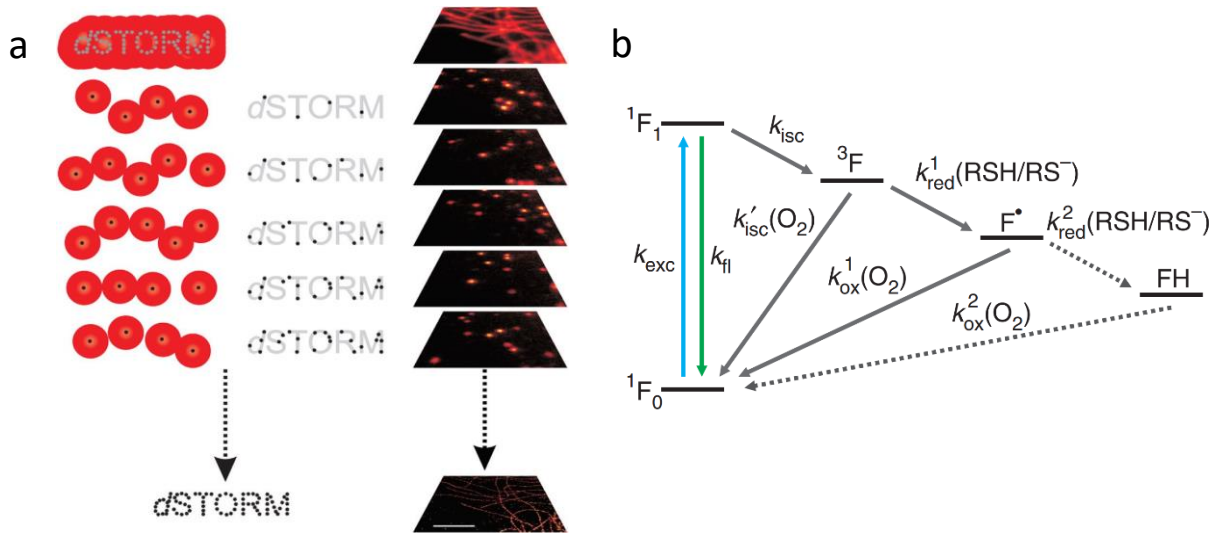
Figure 4 The principle of *d*STORM. (a) Upon labeling with photoswitchable fluorophores the dyes are transferred into a not fluorescent off state. Only few molecules are spontaneously activated and emit fluorescence. Once activated, the molecules are localized and again deactivated. Repetitive localization of single dye molecules allows the reconstruction of a super-resolved image. (b) To enable reversible photoswitching cycling dyes between the ground state F_0 and F_1 enter the triplet state ^3F. Dyes in the triplet state either interact with oxygen to repopulate the ground state or react with thiols to form a stable not emitting radical anion of the fluorophore. This radical anion can be oxidized by molecular oxygen to return to the ground state. Few dyes like ATTO 655 can even be reduced to its leuco form before they return to the ground state. With permission from van de Linde et al. 2011.

Therefore, it is crucial to remove oxygen in the imaging buffer which is often accomplished by an oxygen scavenging glucose oxidase system. However, MEA can also fulfill this role to deplete oxygen (Schafer et al. 2013). According to those reactions, an equilibrium is established between mostly switched off dyes and only few dyes in the on state which results in "blinkling" dyes. The center of all those blinking dyes is then determined using a Gaussian fit with a localization precision of less than 10 nm. The localization precision (I), and with this ultimately the achievable resolution, depends hereby on the number of emitted photons (N) and on the standard deviation of the Gaussian fit (σ), as described with the following equation:

$$I = \frac{\sigma}{\sqrt{N}} \qquad (3)$$

Besides of a maximum photon yield the already described switching rates are of great importance for SMLM experiments as insufficient switching rates will result in overlapping point spread functions (PSF) leading to elongated and asymmetric spots. Such overlapping PSFs cannot be fitted correctly and are either discarded and lost or will provoke wrong PSF fitting and imaging artifacts (Burgert et al. 2015).

Another crucial factor limiting the resolution of SMLM is the labeling density which gets of even greater importance with increasing resolution. This relation was described within the Nyquist-Shannon sampling theorem which defines that the distance between two molecules next to each other must be at least half of the final resolution.

To sum up, the final resolution depends not only on the number of emitted photons and therefore the accuracy of the Gaussian fit, but also on suitable switching rates and label density.

1.4 Multicolor dSTORM

The success of *d*STORM also resulted in the development of various multi-color approaches to visualize more structures at a superior resolution. Hereby, multicolor measurements can be realized by either spectral separation or by using the same dye in sequential approaches. In classical two color experiments well established dye-pairs are Alexa Fluor 647/Cy5 and Alexa Fluor 532 (Andreska et al. 2014, van de Linde et al. 2013) or Alexa Fluor 647/Cy5 and CF 568 (Heller et al. 2019) for not only adherent cells, but also primary neurons (Andreska et al. 2014) or tissue (Heller et al. 2019). Here, chromatic aberrations need to be corrected using fiducial markers to align the cameras. Another, nearly aberration-free approach is spectral-demixing (SD) *d*STORM (Lampe et al. 2012). SD *d*STORM applies dye pairs like Alexa Fluor 647/CF 647 and Alexa Fluor 700 (Lampe et al. 2012), DY678 (Lampe, Tadeus and Schmoranzer 2015) or CF680 (Lehmann et al. 2016) which can be both excited by the same laser. Although their emissions overlap partially, the different emissions can be separated efficiently with a minimal crosstalk of solely 1.6% (Lampe et al. 2012). This is realized by splitting the emissions on two different cameras with a dichroic mirror and thereby separating the emissions in different ratios. Because all fluorophores are always visible on both channels, pseudo-colors can be assigned to the dyes using the different emission ratios of the dyes on the two cameras.

However, when using different dyes there is always the need for a compromise in terms of the switching buffer which may lead to signal loss due to photobleaching and the majority of dyes are not suited for high-quality *d*STORM imaging. Moreover, these approaches are mostly restricted to two colors.

It may also seem reasonable to use the best *d*STORM dye, Alexa Fluor 647, more often under perfect chemical conditions. This can be realized by the removal of the dye after imaging and consequent restaining of another target in order to use the dye sequentially. In one very simple

approach, introduced by Valley et al. (Valley et al. 2015), this was enabled by irreversible photo bleaching in combination with quenching of Alexa Fluor 647 by $NaBH_4$. After imaging of the first structure of interest, the switching buffer was replaced by PBS, the dyes were photobleached with high laser densities at 405 nm (~0.24 kW/cm^2) and 637 nm (~1.7 kW/cm^2) and subsequently quenched by $NaBH_4$. This was followed by the staining and imaging of another structure, again with Alexa Fluor 647. This combination of bleaching and quenching resulted in a negligible cross-talk of only 0.2% when imaging clathrin followed by tubulin (Valley et al. 2015).

Another idea was realized in multiplexed antibody size-limited *d*STORM (madSTORM) (Yi et al. 2016), where bound antibodies were efficiently removed after imaging by the elution in high salt concentrations and Tween-20 in combination with photobleaching. After antibody removal new structures were stained with Alexa Fluor 647 and this could be repeated to stain and image 25 different epitopes. Albeit this protocol provides a huge improvement by removing the antibodies and therefore allows the imaging of "limitless" structures, this antibody elution and restaining procedure requires fixed cells and therefore impedes multi-color live-cell stainings. Additionally, both approaches are very time consuming and may be prone to cross-talk from prior staining due to incomplete bleaching or antibody-removal after several rounds of imaging. Recently, this problem was beautifully addressed within the DNA-exchange *d*STORM protocol (Schueder et al. 2017) using exchangeable DNA-probes. Hereby, DNA-conjugated antibodies are used to stain the structures of interest in a "one-pot" reaction. Hence, this protocol is fully compatible with staining protocols of both, fixed and living cells. The immunostaining is followed by the introduction and hybridization of the first DNA-dye strand in labeling buffer. Subsequently, by repeated washing the labeling buffer as well as unbound DNA are removed and exchanged by a *d*STORM switching buffer. After image acquisition the imaging buffer is replaced by a washing buffer containing 30% formamide which decreases the DNA melting temperature by partial denaturation and removes the bound DNA-dye strand. To enable an efficient DNA removal, the 12 - 13 bp long DNA strands are designed for optimal hybridization in labeling and optimal removal in washing buffer. Finally, the washing buffer is replaced by labeling buffer containing a new DNA-dye, complementary to the new target strand (Fig. 5). Using DNA-origami this method has also been validated in *d*STORM and STED which resulted in 92% correctly assigned spots. This whole procedure can be repeated in principle nearly limitless and is only limited by the number of orthogonal DNA sequences. Moreover, this washing and staining procedure is extremely fast, taking only 20 minutes per round, making this a superior sequential labeling technique (Schueder et al. 2017).
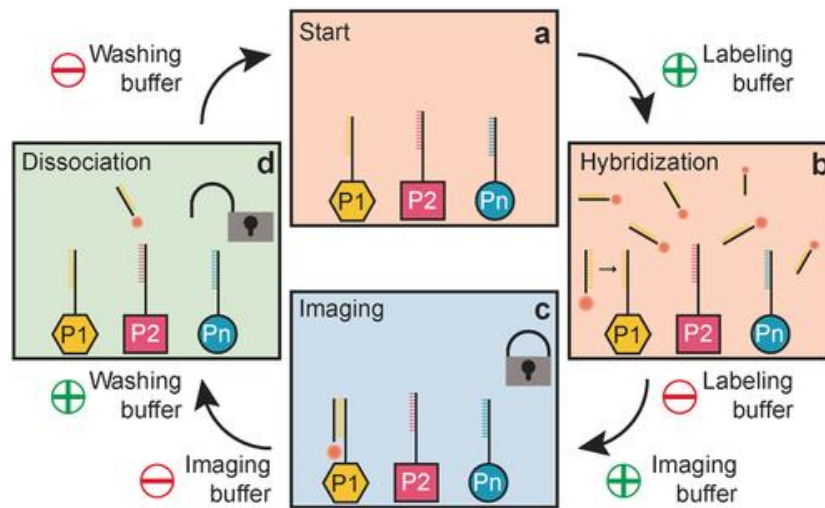
Figure 5 Procedure of the DNA-exchange. (a) Targets are labeled with 12 - 13 bp long oligonucleotide conjugated antibodies. (b) The first dye-conjugated DNA-strand hybridizes in labeling buffer to the complementary strand. (c) The image is acquired in imaging buffer. (d) The introduction of the washing buffer dissociates the dye-conjugated DNA. This process is repeated until all target structures are imaged. With permission from Schueder et al. 2017.

1.5 Quantitative cluster analysis

It could be shown in correlative studies of the nuclear pore complex that *d*STORM can truly provide quantitative data (Löschberger et al. 2014). Due to the nature of *d*STORM with dyes that blink several times, localizations have to be assigned to single antibodies. To provide quantitative molecule numbers, they need to be clustered. However, there is a plethora of different cluster algorithms which also use different clustering approaches. These algorithms can be center-, hierarchical-, grid- or density-based (Scitovski and Sabo 2019).

Center- or partitional-based cluster algorithms group all clusters simultaneously and do not apply a hierarchical structure. The simplest and most used center-based algorithm is the *k*-means algorithm. This algorithm is strongly dependent on the initial cluster centers and unable to find non-convex clusters (Scitovski and Sabo 2019). Hierarchical-based algorithms either start with all points as single clusters and merge these according to their parameters or assign all data points to one cluster and separate this cluster into smaller ones. By contrast, grid-based clustering algorithms divide the data space into cells forming a grid. Then these cells are clustered which represent the data points instead of directly clustering the data points (Aggarwal 2014). On the other hand, density-based algorithms rely on the principle of connecting dense areas which are separated by sparse or empty areas.

The most used algorithm among these is the density-based spatial clustering of applications with noise (DBSCAN) algorithm since it was introduced by Martin Ester et al. in 1996 (Ester et al. 1996). This algorithm connects data points (Fig. 6) and requires two parameters, the radius

within localizations are grouped (ε) and the minimum number of localizations per cluster (min-Points). Within this algorithm, data points are categorized into core points (points with > min-Points), border points (points with < minPoints, but within ε of a core point) and noise (points which are neither a core nor a boarder point) (Schubert et al. 2017).

The right parameter choice is very crucial as a too small ε will yield in most data points assigned to as noise and a too large ε will result in merged clusters because too many data points are assigned to one cluster. On the other side, a too low minPoints value will assign every point to be a cluster, whereas a high minPoints value might discard many clusters. Hence, the parameters need to be determined carefully to avoid wrong and incomplete clustering (Ester et al. 1996, Scitovski and Sabo 2019, Schubert et al. 2017, Duan et al. 2016).

Fortunately, as dye-conjugated antibodies with blinking dyes resemble dense areas or clusters, this algorithm can be implemented to group localizations of a *d*STORM experiment and therefore to count and quantify single molecules. Typical parameters are 20 nm for ε, as this is the resolution achieved within a *d*STORM experiment, and at least three localizations per cluster for minPoints, but these parameters need to be determined experimentally. From now on, these grouped localizations will be referred to as "clusters".
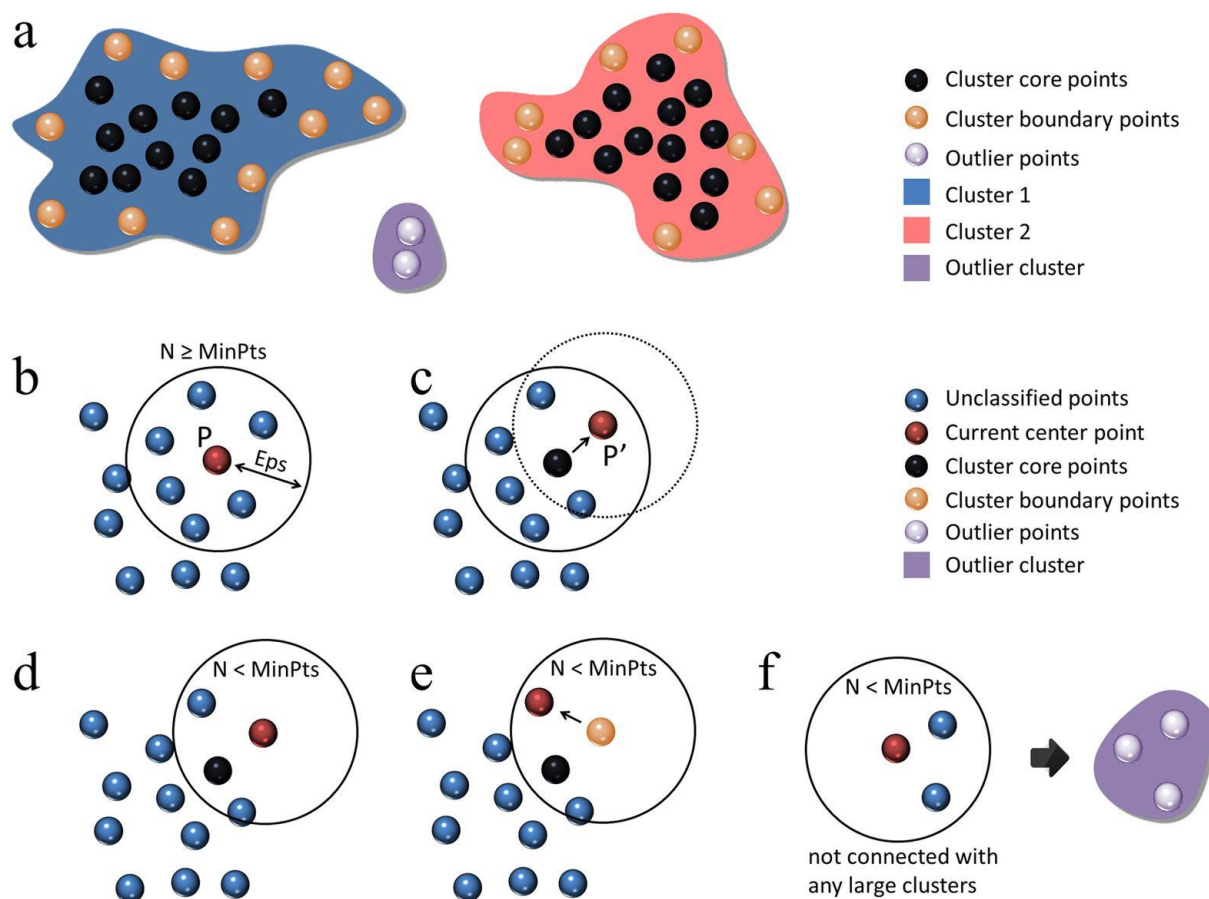
Figure 6 Schematic overview of the DBSCAN algorithm. (a) Clustering result with core points, boundary or core points and outlier points or noise. (b-f) Impact of the parameter choice on the clustering. With permission from Duan et al. 2016.

1.6 Receptors and their importance in immunotherapy

Receptors are a key component for intra- and extracellular communication. They act as antennae to detect the presence of signaling molecules and translate these *via* cellular effector pathways and signal transduction into physiological functions. If perturbations occur here, this may lead to severe signal transduction errors and metabolic defects causing various diseases. The nomenclature of cluster of differentiation (CD) has been introduced to classify the more than 4000 surface molecules on leucocytes, whereas the receptors were categorized by their reactivity with a library of monoclonal antibodies. Nowadays, this nomenclature ranges from CD1 to CD371. Those antibodies are widely used to identify cell types in the clinics and in research for both diagnosis and therapy. Within this thesis relevant receptors ranging from CD2 to CD105 were investigated.

CD2 is an adhesion molecule that can be found on the surface of T-cells and natural killer cells. Due to its early appearance on T-cells, CD2 is considered as T-cell marker, although not present on all T-cells (Schubert et al. 2006, Bausch-Fluck et al. 2015). Furthermore, CD2 occurs to ~85% as monomer (Murray et al. 1995) and can trigger T-cell activation. A constitutive T-cell specific marker however, is the T-cell co-receptor CD3. The protein complex CD3 is crucial for T-cell activation as it associates with the T-cell receptor (TCR) (Smith-Garvin, Koretzky and Jordan 2009) and should be homogeneously distributed on not activated CD4$^+$ and CD8$^+$ T-cells according to new studies. CD3-clustering is a heavily debated topic, although it is known to form nanoclusters after activation (Rossboth et al. 2018). CD4 and CD8 on the other hand are co-receptors that are of great importance for the development and determination of the exact T-cell subtype (Fournier et al. 2010). The dimeric T-cell marker CD5 in contrast inhibits TCR-signaling and is thought to be associated with CD3ζ within the CD3-TCR-complex (Bamberger et al. 2011, Perez-Villar et al. 1999). CD7 is a co-receptor probably involved in T-cell interaction which is expressed in most, but not all T-cells (Aandahl et al. 2003). The integrin CD11a on the other hand appears heterodimeric and has been shown to interact with CD45 by its cytoplasmic tail (Geng et al. 2005). CD11a is also associated with the regulation of CD8$^+$ T-cell differentiation and with memory development after infection (Bose et al. 2013). The homodimeric co-receptor CD28 is constitutively expressed on T-cells and is crucial not only for activation, but also for survival and productive T-cell responses. It also interacts with its coligand B7 to transduce signals necessary for an immediate T-cell response (Li and Sayegh 2007). The receptor-like transmembrane protein tyrosine phosphatase (RPTP) CD45 is a highly abundant protein in the plasma membrane of all nucleated hematopoietic cells. Studies could show that CD45 is of great importance for signal transduction and the regulation of peripheral T-cell

activation (Majeti et al. 2000, Zamoyska 2007). CD69 is a dimeric membrane protein expressed on T-cells at an early activation stage. Upon expression, CD69 triggers T-cell activation and proliferation as costimulus (Risso et al. 1991).

The receptors CD20 (B-cell marker) and CD105 (endoglin) by contrast are mostly absent or present on only a small subset of T-cells (Schuh et al. 2016, Stashenko et al. 1980, Nassiri et al. 2011, Schmidt-Weber et al. 2005).

The concept of immunotherapy harnesses the immune system's activity to eradicate cancer cells by targeting specific, ideally solely on cancer cells expressed markers. Receptors are an attractive target for those therapies due to the fact that many cancer cells often have tumor associated surface molecules in their plasma membrane that can be targeted by antibodies or antibody-derived reagents. Unfortunately, most cancer cell markers are also found on healthy cells making the target choice difficult (Wei et al. 2019).

The first clinically used monoclonal antibody was the anti-CD20 antibody rituximab against B-cell malignancies, lymphoma and leukemia. CD20 is strongly expressed on those tumor cells, but unfortunately CD20 is also widely expressed on naive B-cells and affects therefore also healthy B-cells. Rituximab may mediate cell killing *via* various pathways: Upon binding, apoptosis may be triggered by not yet completely understood caspase dependent and independent mechanisms. Alternatively rituximab binding may also trigger a complement cascade, the complement-dependent cytotoxicity (CDC) or recruit natural killer cells leading to an antibody-dependent cell mediated cytotoxicity (ADCC) which kills the target cell by the release of perforin and granzyme B. Lastly, macrophages might recognize bound rituximab to phagocytose the target cell *via* antibody-dependent phagocytosis (ADP, Fig. 7) (Pierpont et al. 2018).

Another highly relevant monoclonal antibody used in the cancer therapy is the anti-CD38 antibody daratumumab. This transmembrane glycoprotein CD38 is an attractive target as it is expressed on the surface of haematopoietic cells and importantly overexpressed in multiple myeloma cells (Lin et al. 2004). Daratumumab has been approved as monotherapy and combination therapy for patients with relapsed and refractory multiple myeloma (Blair 2017). Especially the combination therapy with bortezomib and dexamethasone or lenalidomide and dexamethasone is very promising with complete response rates of up to 43% (Palumbo et al. 2016, Dimopoulos et al. 2016). It could also be observed that a high CD38-expression correlates with a high efficacy and that patients with a high CD38-expression had a higher response chance. Although very potent, it was also noticed that during daratumumab treatment CD38-expression is often decreased during disease progression favoring immune escape (Nijhof et al. 2016).

Hence, it is not surprising that many efforts were made in this field to find molecules to selectively increase the CD38-expression specifically in multiple myeloma cells. One of those molecules was panobinostat, a non-selective histone deacetylase (HDAC) inhibitor that induced a

CD38 increase and could therefore increase ADCC after daratumumab treatment (Garcia-Guerrero et al. 2017). However, panobinostat showed also severe toxicities increasing the need for alternatives with better tolerability. A possible alternative could be ricolinostat, a specific inhibitor of histone deacetylase 6, currently in phase 1/2 trial (Vogl et al. 2017) which was investigated in this work.
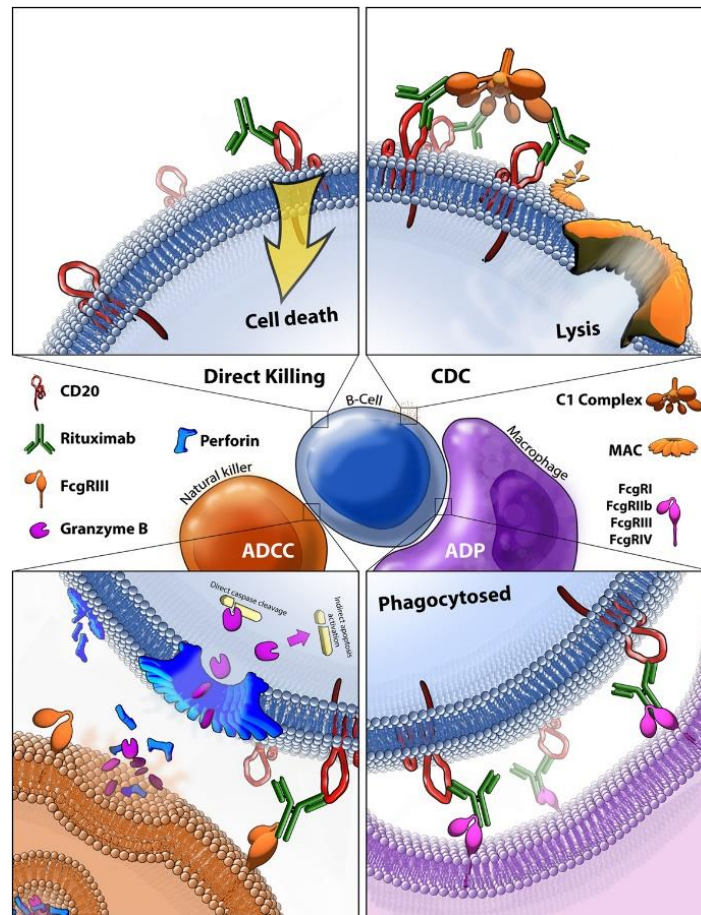
Figure 7 Schematic overview of the killing mediated by rituximab of CD20-positive cells. (Top left) Rituximab binding directly triggers apoptosis *via* caspase independent and caspase dependent pathways. (Top right) Binding of rituximab recruits the C_1-complex initiating the complement cascade which triggers cell death *via* complement-dependent cytotoxicity (CDC). (Lower left) Rituximab recruits natural killer cells which results in antibody-dependent cell-mediated cytotoxicity. After perforin release granzyme B enters the target cell and triggers apoptosis by mostly cleaving caspases. (Lower right) Antibody-dependent phagocytosis (ADP) is triggered by macrophages recognizing CD20 bound rituximab. With permission from Pierpont, Limper and Richards 2018.

Another extremely elegant way to stimulate the own immune system to fight cancer are chimeric antigen receptor (CAR) T-cells. Hereby, in a first step patient cells are collected by leukapheresis which is followed by monocyte elutriation and T-cell selection. Hereafter, the T-cells are activated by anti-CD3 and anti-CD28 antibodies and transduced with the CAR-construct. Finally, the transduced CAR T-cells are expanded ex vivo and harvested to be infused back into the patient. CAR T-cells will then bind to their target molecule and consequently lyse the target cells without the need for antigen presentation *via* MHC-complexes.

By now there are countless different CAR-designs. However, the base structure remained barely unchanged. The CAR consists out of a single-chain variable fragment (scFv) with an antibody-like variable heavy (V_h) and a variable light (V_L) chain that is fused by a peptide linker. The scFv is connected to an intracellular signaling domain that was consequently improved since the original CAR-development. In the 1st generation of CARs the intracellular signaling domain consisted solely out of CD3ζ (Fig. 8). This resulted often in an only short immune response with insufficient IL-2 secretion due to the absence of co-stimulatory signals (Imai et al. 2004, Maher et al. 2002). Therefore co-stimulatory domains like 4-1BB (Imai et al. 2004), CD27, CD28 (Maher et al. 2002) and CD134 (Fesnak, June and Levine 2016) were fused to CD3ζ which resulted in an enhanced persistence of CAR T-cells (Fesnak et al. 2016).
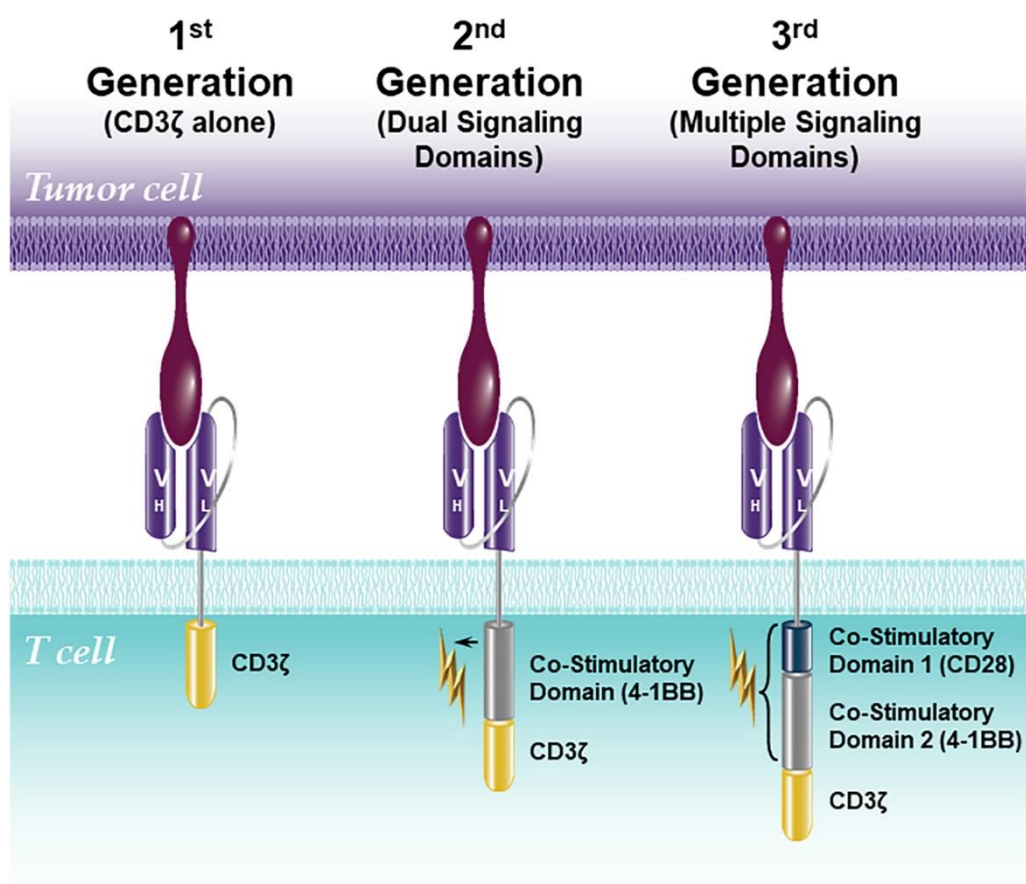
Figure 8 Schematic overview of the chimeric antigen receptor structure. CARs consist of a single-chain variable fragment (scFv) with a variable light (V_L) and heavy chain (V_H) connected by a linker. In first generation CARs the scFv was solely linked to CD3ζ, while second generation CARs carry one and third generation CARs multiple co-stimulatory domains like CD28 and 4-1BB. With permission from Feins et al. 2019.

The first classical target for CAR T-cells was CD19 for the treatment of advanced B-cell malignancies. Those therapies have been validated in the clinics for years and underline the curative potential of CARs (Turtle et al. 2016). However, to be a universal approach in the fight against cancer, new targets need to be found and validated, ideally also for solid tumors.

In the search for novel targets several antigens stand out, among them the B-cell maturation antigen (BCMA) and the signaling lymphocytic activation molecule family member 7 (SLAMF7) for the treatment of multiple myeloma and the FMS-like tyrosine kinase 3 (FLT3) for the treatment of acute myeloid leukemia (Prommersberger et al. 2018). BCMA is a member of the tumor necrosis family receptor (TNFR) that is expressed on multiple myeloma cells and on some hematopoietic cells. As BCMA is not expressed on healthy solid tissue, this makes BCMA an attractive target for BCMA targeting immunotherapies (Seckinger et al. 2017, Hipp et al. 2017). CAR T-cells targeting BCMA are currently in the phase I clinical trial for the treatment of multiple myeloma and could induce complete responses in a myeloma subset (Ali et al. 2016). Unfortunately, BCMA loss or downregulations have also been reported leading to severe relapses which is decreasing the hopes in BCMA as suitable target. Therefore, similar to CD38, the idea occurred to increase the expression of BCMA and the number of BCMA expressing cells by the addition of a multiple myeloma cell specific drug. One possible molecule could be all-trans retinoic acid (ATRA) which has been shown to induce epigenetic changes in multiple myeloma cells (Balmer and Blomhoff 2002). This effect could already be harvested in combination with daratumumab in myeloma and possibly more antigens could be affected by ATRA (Nijhof et al. 2016).

Despite being very successful in the treatment of especially B-cell malignancies, also severe side effects occurred in CAR-treatments. The most frequent toxicities are the cytokine release syndrome (CRS) and the CAR T-cell-related encephalopathy syndrome (CRES). In CRS the CAR T-cells get activated, expand and lyse the cells expressing the target receptor. Hereby, high amounts of interferon-γ and tumor-necrosis factor α (TNF-α) are released which activate monocytes and macrophages with enhanced tumoricidal capacity (Mosser and Edwards 2008). These activated macrophages secrete high levels of inflammatory cytokines (IL-1, IL-6 and IL-10) and inducible nitric oxide synthase (iNOS) resulting in symptoms like fever, muscle pain, low blood pressure and confusion (Yanez, Sanchez-Escamilla and Perales 2019).

An interesting case appeared in 2015, where a refractory multiple myeloma patient was treated with anti-CD19 CARs. This resulted in a complete response although 99.95% of the patient's neoplastic plasma cells were negative for CD19 (Garfall et al. 2015). This of course raised questions about the sensitivity of the conventional antigen measurements in the clinics with the widely used flow cytometry.

1.7 Expansion microscopy

Super-resolution imaging has become a very powerful tool in the last decade and has shed light on the spatial protein organization of many biological samples (Sauer and Heilemann 2017, Schermelleh et al. 2019). However, multi-color experiments remain challenging and 3D-experiments are often limited axially. Furthermore, these methods require intensive experience and specialized equipment within the laboratories.

Recently, expansion microscopy (ExM) (Chen, Tillberg and Boyden 2015) was introduced by Boyden and coworkers. In ExM the proteins are linked into a dense network of a swellable acrylamide gel and the sample is expanded isotropically approximately fourfold after homogenization by an unspecific proteinase to bypass the resolution limit. This expansion, which was published in 2015, allowed a fourfold improvement in both the lateral and axial dimension enabling a lateral resolution of ~60-70 nm on conventional microscopes. The first approaches could be separated in two main protocols (Fig. 9). In the first, the sample was fixed, stained and labeled with an amine or acrydite containing label (Chen et al. 2015), linked with AcX (Tillberg et al. 2016), MA-NHS (Chozinski et al. 2016), glutaraldehyde (Chozinski et al. 2016) or Label-X (Chen et al. 2016), gelated, digested with proteinase K and expanded in ddH$_2$O (Fig. 9). These approaches suffer from a relatively big linkage error and fading dyes during the gelation step. To avoid those disadvantages the magnified analysis of the proteome (MAP) (Ku et al. 2016) was developed. Here, the sample is incubated in a mixture of formaldehyde and acrylamide to penetrate the whole sample with acrylamide and to avoid intra- and inter-protein crosslinking during the gelation. Following gelation, the sample is boiled at 95°C and denaturated in SDS to linearize all proteins present in the gel until the sample is expanded in ddH$_2$O and finally stained. This protocol allows therefore a post-staining which minimizes linkage errors, avoids fading dyes by the radical reaction during gelation and even new epitopes may get accessible due to the denaturation step. Unfortunately, not all antibodies will recognize denatured epitopes (Gambarotto et al. 2019).

At an impressive speed other, new protocols were developed to further improve this attractive method which makes super-resolution available to everyone even without sophisticated set-ups. These protocols enable the expansion of RNAs (Chen et al. 2016), higher expansion factor of tenfold (Truckenbrodt et al. 2019) and even twentyfold (Chang et al. 2017) by iterative ExM in both cells and tissue. Even the combination with super-resolution microscopy was already reported (Gao et al. 2018, Xu et al. 2019). Although very easy to implement, care must be taken when new structures are expanded, as the protocol might need to be adjusted like in the case of the multiprotein complex of centrioles to enable a truly isotropic expansion

(Gambarotto et al. 2019). Using these structures it could be shown that, although well established by now, ExM can bear also the risk of artifacts.
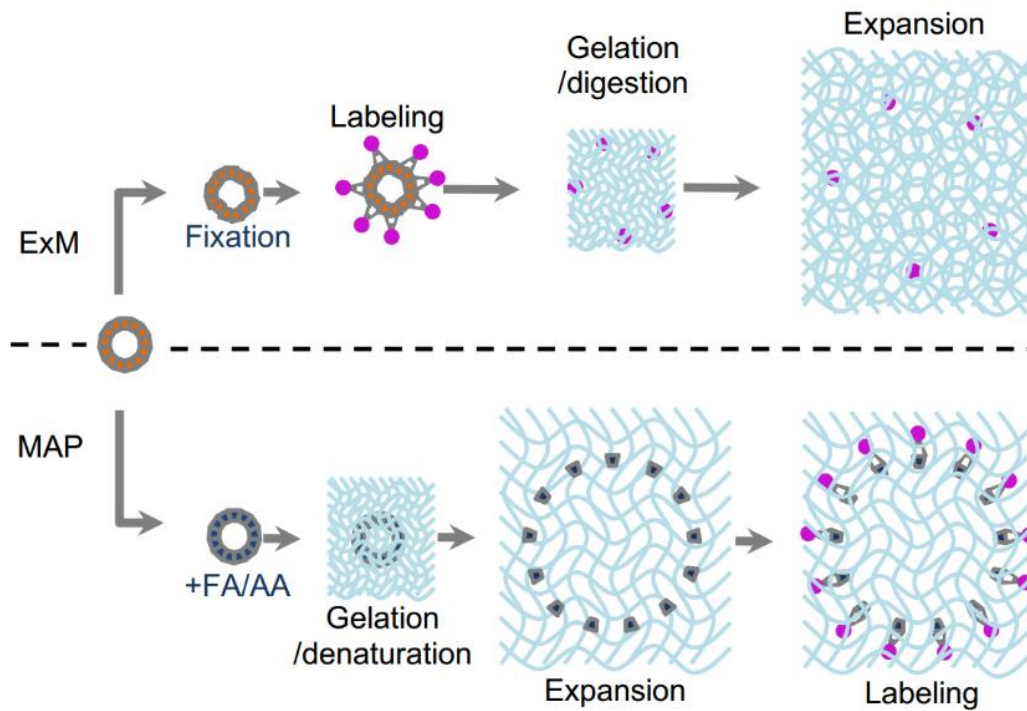
Figure 9 Schematic overview about the ExM- and MAP protocol. In ExM the sample is fixed, labeled and after gelation and digestion, expanded. Contrary, in MAP the sample is first incubated in formaldehyde and acrylamide followed by gelation and protein denaturation. Subsequently, the sample is expanded and immunostained. With permission from Gambarotto et al. 2019.

1.8 Intracellular pathogens

1.8.1 *Chlamydiales*

The order of *Chlamydiales* consists out of eight families, among them the *Chlamydiaceae* and *Simkaniaceae*. All are gram-negative obligate intracellular bacteria, share an up to 80% similarity in their 16S and 23S rRNA and pass a developmental cycle within the host cell (Everett, Bush and Andersen 1999).

The bacterium *Chlamydia trachomatis* as member of the *Chlamydiaceae* family is of major clinical relevance because this bacterium is human specific. *C. trachomatis* causes blinding eye diseases (trachoma) or sexually transmitted diseases eventually leading to infertility with annually more than 100 million infections (Belland, Ojcius and Byrne 2004). In a typical *C. trachomatis* life cycle (Fig. 10) *Chlamydia* infect the host as small elementary bodies (EB) by binding to the host cell and by interactions with membrane proteins. Internalization is then induced by changes within the actin cytoskeleton, assisted by GTPases of the RHO family and other factors (Bastidas et al. 2013). Effector proteins are injected into the host cell *via* a needle like structure, the chlamydial type 3 secretion system (T3SS) (Moore and Ouellette 2014). Upon internalization the *Chlamydia* remain within this membrane bound vesicle, the so called inclusion. This inclusion is completely independent from any endocytic or lysosomal pathway creating an exclusive niche for the *Chlamydia* to replicate and develop (Hackstadt et al. 1996). However, the inclusion needs to be stabilized structurally which is enabled by a scaffold consisting out of F-actin, intermediate filaments and tubulin (Al-Zeer et al. 2014). Besides the cytoskeleton also the cellular organelles like mitochondria and the smooth endoplasmatic reticulum (ER) are rearranged (Agaisse and Derré 2015, Derré 2015). Both interactions are not fully understood, although it seems reasonable that the *Chlamydia* might rearrange those organelles to gain nutrition in the form of lipids and metabolites and to inhibit apoptosis. This inhibition of apoptosis and importantly also the lysosomal degradation of the inclusion is mediated by interfering with the host ubiquitin system using the chlamydial deubiquitinase 1 (Cdu1). This protein localizes at the inclusion membrane (Fischer et al. 2017) while its expression starts at ~16 hours post infection (hpi) and increases further during the infection (Belland et al. 2003). It is known that Cdu1 deubiquitinates and therefore stabilizes anti-apoptotic proteins like Mcl-1 (Fischer et al. 2017) avoiding premature cell death. Moreover, Cdu1 has been shown to be involved in the stabilization of IκBa, the inhibition of NFκB-induced inflammatory responses (Le Negrate et al. 2008) and the fragmentation of the host cell's Golgi-apparatus (Pruneda et al. 2018).
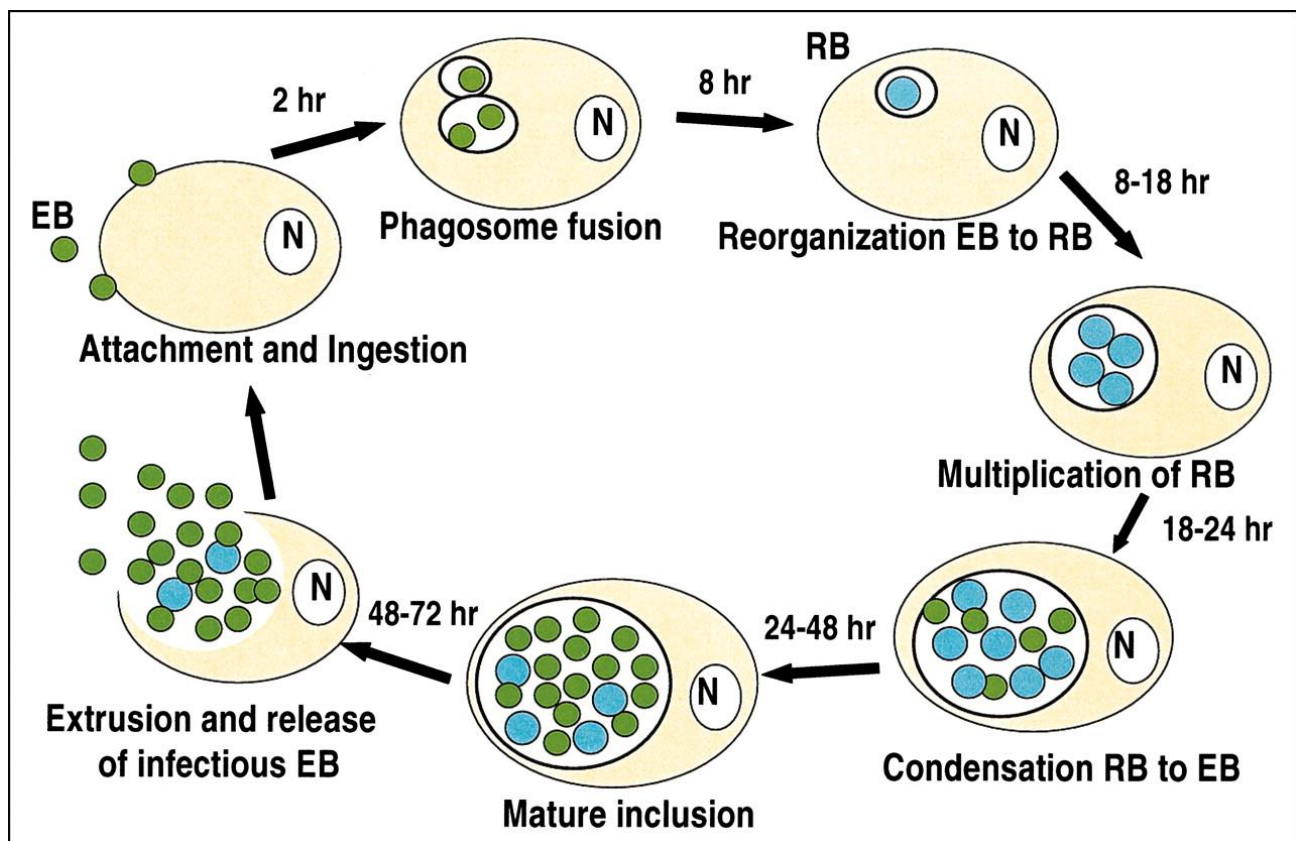
Figure 10 Developmental cycle of *Chlamydia* within epithelial cells. To infect cells, EBs first attach to the surface of the host cell and are then taken up. About 8 hours later EBs begin to differentiate into its replicative form. *Chlamydia* begin to replicate within the inclusion until they redifferentiate into EBs after ~24h. The inclusion matures up to 48 h which is followed by the extrusion and release of EBs to infect new cells. With permission from Hammerschlag 2004.

After 6 – 9 hpi the EBs begin to transcribe early transition genes necessary for the conversion to its metabolically active form, the reticulate body (RB). During this transition, mediated by histone 1 homologues HC1 and HC2, chromatin gets decondensed to activate transcription and the RBs begin to expand (Grieshaber et al. 2006).

After extensive RB multiplication the transition back to EBs is again mediated by HC1 and HC2 which switch off the transcription of RB related genes again after ~24 hpi. This process may be triggered by RBs "falling off" the inner membrane of the inclusion membrane (Wilson et al. 2006), and can strongly be inhibited by antibiotics, stress induced by the environment or missing nutrition. Among those important nutrients are sphingolipids, especially ceramides. It is assumed that ceramides serve as precursor for sphingomyelin directly at the inclusion membrane or as chlamydial signaling molecule (Derre, Swiss and Agaisse 2011). To gain ceramides, *Chlamydia* hijack the lipid transfer protein CERT which regulates in uninfected cells the non-vesicular transport to the Golgi-apparatus from the ER. This hijacking process is hypothesized to be mediated by the inclusion protein D (IncD) that colocalizes at the inclusion membrane with CERT. The lipid transfer is then fulfilled by association with the ER-resident vesicle-associated membrane protein-associated protein B (VAPB) after close interaction with

the ER tubules (Agaisse and Derre 2014, Derre et al. 2011). The importance of ceramides for the chlamydial development could be demonstrated by the inhibition of CERT with the CERT specific inhibitor HPA-12 which strongly delayed or even impeded the growth of *C. trachomatis* (Koch-Edelmann et al. 2017, Elwell et al. 2011).

However, if not inhibited, after 48 hpi the inclusion of *C. trachomatis* matures and the *Chlamydia* begin to be released from the host cell. This release is well characterized and follows one of the following two methods. In the first possibility of release *Chlamydia* lyse the host cell and escape from the bursting cell (Hybiske and Stephens 2007). The lysing of the host cell is mediated by many proteins with the *Chlamydia* protease activity factor (CPAF) as one of the most prominent ones. CPAF degrades several host proteins before the inclusion membrane gets permeabilized. After permeabilization of not only the inclusion membrane, but also the nuclear membrane and several organelles, the *Chlamydia* are released (Snavely et al. 2014). On the other hand, *Chlamydia* may also escape from the host cell without killing it in a much slower process. Hereby, the cytoskeleton is modified and primarily the interactions between actin and myosin cause a depolymerization of microtubules. This is followed by a cytokinesis like process, where a contractile ring is formed and the *Chlamydia* are released from the cell (Hybiske and Stephens 2007).

The closely related pathogen *Simkania negevensis* by contrast belongs to the family of the *Simkaniaceae* and is prevalent especially among adults with pneumonia and children with bronchiolitis (Lieberman et al. 2002). This gram-negative bacterium shares many similarities with *Chlamydia* like the two distinct developmental forms EBs and RBs but for example builds up a different inclusion, the *Simkania*-containing vacuole (SCV). Interestingly, *Simkania* growth is significantly slower compared to *Chlamydia* and this pathogen can remain within its host cell for up to 10 days without lysing the cell (Kahane et al. 2001). In electron microscopy (EM) studies it could be shown that the SCV consists out of many, both EB and RB containing vacuoles with mitochondria arranged around them (Kahane et al. 2001, Friedman, Dvoskin and Kahane 2003, Mehlitz et al. 2014). Furthermore, a close association between the ER membrane and the SCV could also be demonstrated using *d*STORM (Mehlitz et al. 2014).

1.8.2 Fungi and their cell wall composition

Although very small, Fungi are highly important and relevant pathogens. Fungi are essential not only for human nutrition and health, but are also keyplayers in biodegradation and on the other hand dangerous pathogens for plants, animals and humans (Lange 2014, Meyer et al. 2016). An important characteristic of fungi is their cell wall consisting out of chitin, β-1,3-glucan, α-1,3-glucan and various mannans and mannoproteins (Osherov and Yarden 2010). Hereby, the dynamic cell wall composition is crucial for not only viability, morphogenesis and pathogenesis, but also for the ecology of the fungus. Interestingly, the cell wall composition is highly regulated and can be adapted when exposed to new environmental conditions or various forms of stress. Due to this importance of the cell wall for fungi it is not surprising that, although the cell wall composition strongly varies among different species (Fig. 11), ~20% of the whole yeast genome is associated with the synthesis of the fungal cell wall (Lesage and Bussey 2006, Gow, Latge and Munro 2017). These extremely robust cell walls withstand the turgor pressure mostly between 0.2 and 10 MPa (few even 20 MPa), making the fungal cell wall one of the most robust walls in nature (Gow et al. 2017, Erwig and Gow 2016).
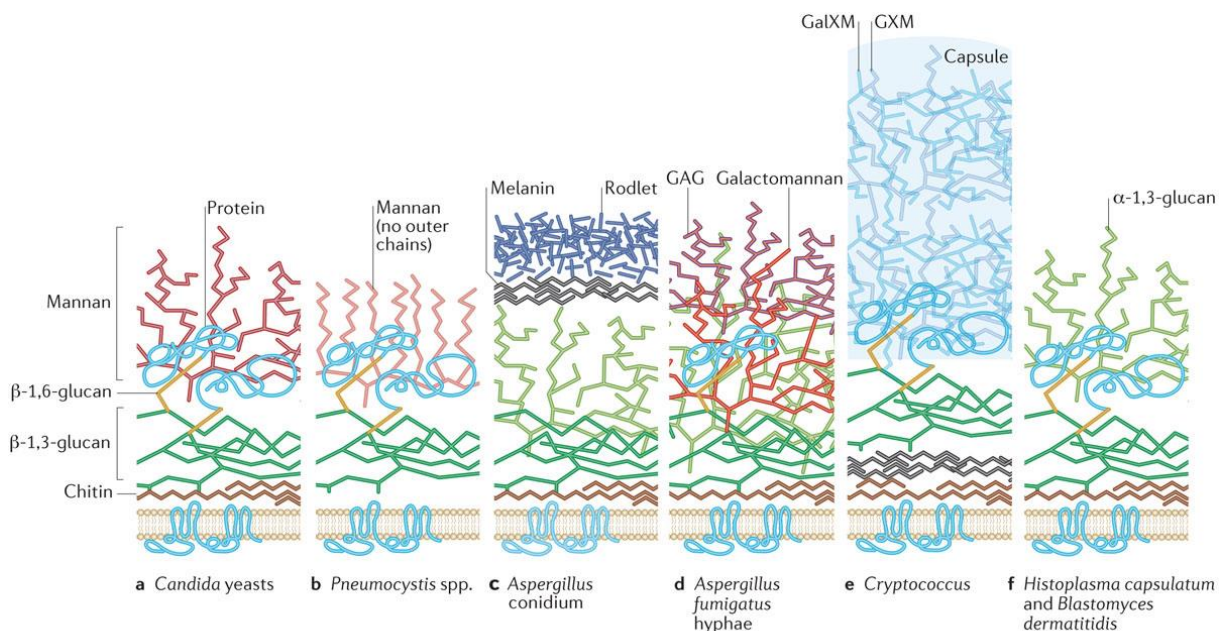
Figure 11 Cell wall organization of fungal pathogens. The cell wall composition of various fungi differs strongly and is composed out of different proteins, glycans and mannans. With permission from Erwig and Gow 2016.

There have also been efforts to efficiently remove this cell wall to form fungal protoplasts. Hereby, a mixture of various lytic enzymes including β-glucanases, chitinases, cellulases and proteases was applied to fungi to successfully produce protoplasts from *Aspergillus spp.* and *Fusarium spp.* (Ramamoorthy et al. 2015, de Bekker et al. 2009). Within this thesis the fungi *Ustilago maydis*, *Fusarium oxysporum* and *Aspergillus fumigatus* were investigated and served as model for the establishment of ExM on fungi.

Ustilago maydis is a basidiomycete causing corn smut and has a biotrophic parasitic life style (Kahmann and Kämper 2004, Vollmeister et al. 2012). Like other biotrophic pathogens *U. maydis* does not kill its host, but has a very close relationship to its host to reprogram the host's metabolism during infection. In a typical life cycle the diploid spores germinate and form after meiosis a promycelium. After septation four compartments containing one haploid nucleus are formed and after mitosis the haploid cells bud off to turn into sporidia and enter a vegetative life cycle. When on a leaf, two compatible haploid cells fuse to turn into its infectious and fila-mentous form and penetrate the epidermis of the leaf *via* appressoria. Now, the hyphae begin to branch and to form clamp-like structures to properly distribute the nuclei during septum for-mation. As the infection proceeds, plant "tumors" are formed, the hyphae begin to strongly proliferate and to form huge aggregates. Following this, the hyphal morphology changes into a mucuous matrix and new dark colored spores are formed (Lanver et al. 2017).

By contrast, *Fusarium oxysporum* is an ascomycete inhabiting the soil causing the wilt disease in various crop species which can even be an opportunistic human pathogen (Ortoneda et al. 2004). Its spores rest in the soil for long periods of time and germinate after stimulation by roots. This results in hyphal branching and the formation of a mycelial network to penetrate the host root through narrow openings probably supported by degrative enzymes (Michielse and Rep 2009). The further growth is entirely intracellular to draw nutrients directly from the apo-plast without damaging adjacent cells and the fungus can even invade the vascular system. Meanwhile conidia and chlamydospores are constantly produced during the infection and re-turn to the soil, as soon as the host plant dies due to high vascular tissue damage to complete the life cycle (Gordon 2017, Warman and Aitken 2018, Dita et al. 2018).

Aspergillus fumigatus on the other hand is a saprotrophic ascomycete, with a worldwide distri-bution that can cause life threatening aspergillosis in immunocompromised patients and is therefore the most important aerial fungal pathogen (Latge and Chamilos 2019). *A. fumigatus* has a mostly vegetative life cycle (Fig. 12) and spreads, once hyphae have grown into a mature mycelium, by asexual sporulation using conidia on specialized hyphal structures (conidio-phores). This dispersal of *A. fumigatus* conidia is highly efficient making it the primary fungal component in the air (Abdel Hameed, Yasser and Khoder 2004). It is estimated that each person inhales 100 - 1000 conidia each day which are removed by alveolar macrophages. If this fails, the conidia germinate within 4 - 6 h into short hyphae known as germ tubes as the

human body temperature is ideal for *A. fumigatus* (van de Veerdonk et al. 2017). Mostly immunocompromised patients are exposed to a high risk of aspergillosis and once infected, aspergillosis has an extremely high mortality rate (30–95%) (Brown et al. 2012). Other diseases caused by *A. fumigatus* include severe asthma with fungal sensitization or severe allergic bronchopulmonary aspergillosis (van de Veerdonk et al. 2017).
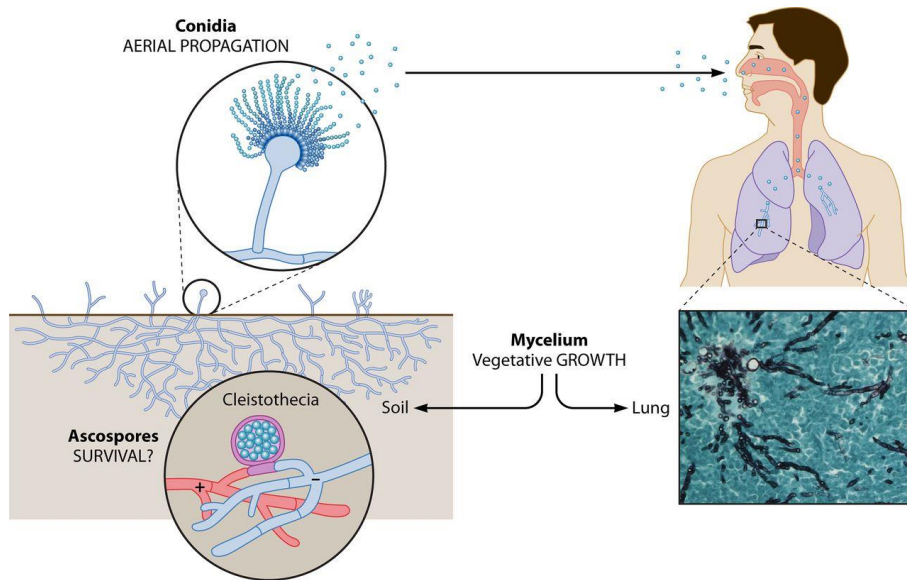
Figure 12 The trimorphic fungus *A. fumigatus* forms a vegetative mycelium in nature and patients. Asexual conidia are formed after starvation and resting ascospores are produced from heterothallic strains. With permission from Latge and Chamilos 2019.

1.9 Ceramides and click chemistry

A main component of the plasma membrane are sphingolipids, glycerophospholipids and cholesterol. Ceramides, sphingolipids with solely an H-atom as residue, regulate many cellular processes including proliferation, apoptosis, cell-differentiation and -migration, and have also been implicated in severe diseases like cancer and neurodegeneration (Zeidan and Hannun 2007). The synthesis of sphingolipids, with ceramides as starting molecules, can be *de novo*, through the recovery of sphingosine from other sphingolipids, through the salvage pathway or by the breakdown of complex sphingolipids like sphingomyelin (Fig. 13).

The *de novo* synthesis is divided into three parts. First, a serine palmitoyltransferase catalyzes the condensation of fatty acid-CoA and serine to 3-ketosphinganine. This 3-ketosphinganine is reduced and then processed to a dihydroceramide. To finally receive a ceramide a double bound is introduced by a dihydroceramide desaturase. In the salvage pathway however, long chain sphingoide bases are reorganized into sphingosine which are acetylated to create ceramides. This main pathway for sphingolipid biosynthesis produces 50-90% of all new sphingolipids (Tettamanti et al. 2003, Kunz and Kozjak-Pavlovic 2019).

Once ceramides are synthesized in the ER, they are transported either *via* vesicular transport or *via* CERT to the Golgi-apparatus, as described in the earlier chapter, and from here into the plasma membrane (Hannun and Obeid 2018). Although under debate, sphingolipids could be shown to form ceramide-rich platforms (CRP), which reorganize the plasma membrane, induce receptor clustering and can facilitate vesicle formation and fusion. These formations could even be increased by the addition of a sphingomyelinase and quantified by *d*STORM (Burgert et al. 2017).

Unfortunately, several obstacles have impeded research in this field. First of all, classical spectroscopic approaches of fluorescent membrane analogs have been impeded by alterations caused by the fluorescent molecules themselves (Kuerschner et al. 2005, Mukherjee et al. 2004). Fluorescence imaging on the other hand always struggled with the limited spatial resolution and could not resolve putative lipid nanodomains or even clusters (Simons and Gerl 2010). Hereby, also the labeling caused problems: Often antibodies did not label the target lipids sufficiently and possibly even induced artifacts. These artifacts may even occur after aldehyde fixation by residual lipid diffusion or by antibody crosslinking (Kraft 2016, Tanaka et al. 2010). As genetic tools to introduce fluorescent proteins are not suitable for non-proteinaceous molecules like glycans and lipids, alternatives were indispensable.
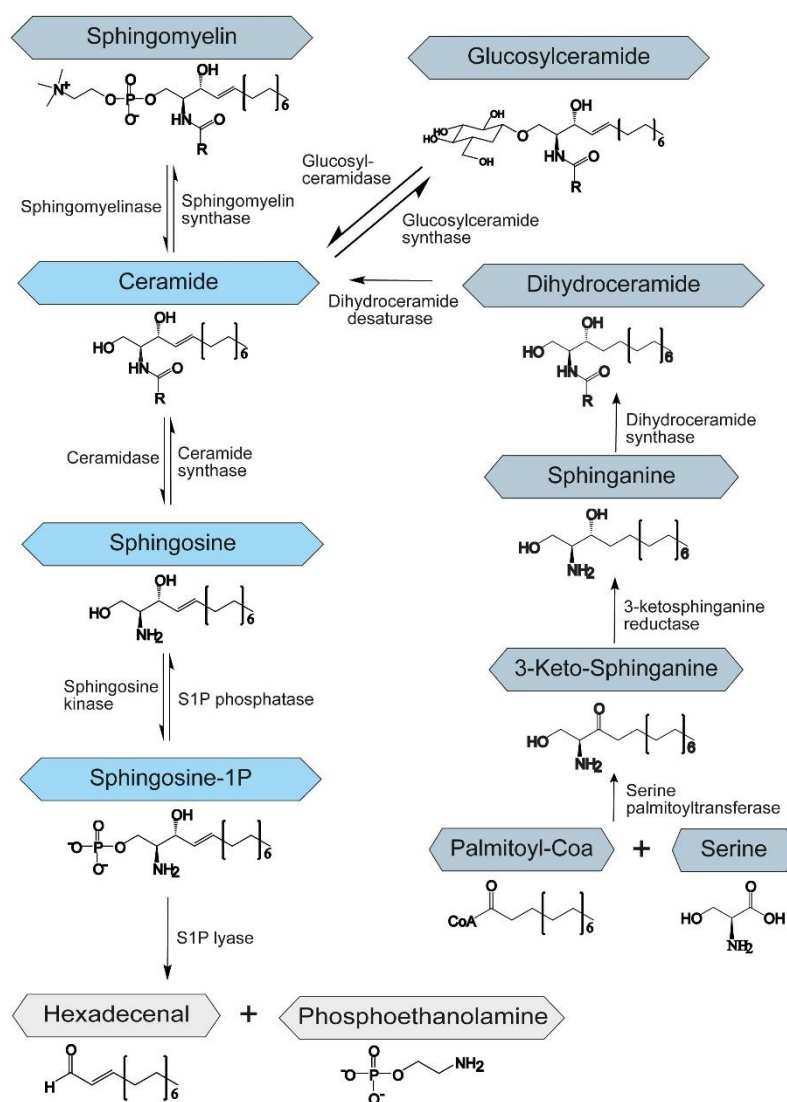
Figure 13 Schematic illustration of the sphingolipid metabolism. Ceramides are keyplayer within the sphingolipid metabolism. They can either be synthesized *de novo* from palmitoyl-CoA, by sphingomyelin hydrolysis or the salvage pathway involving the sphingosine recovery from complex sphingolipids. With permission from Kunz and Kozjak-Pavlovic 2019.

Therefore, a new approach has been introduced to efficiently visualize ceramides using bioorthogonal click chemistry. Bioorthogonal describes that the functional groups must be inert, specifically reactive at biological conditions and in case of *in vivo* experiments nontoxic (Hang et al. 2003). Click chemistry on the other hand describes a pair of functional groups like azides and dibenzocyclooctyne (DBCO)-moieties that react fast and selectively with each other under mild and aqueous conditions (Kolb, Finn and Sharpless 2001).

This chemistry offers an elegant way to stain ceramides by the introduction of small modifications like an azido-modification into ceramides which differ only slightly from the natural compounds. Those azide-modified ceramides were shown to be biocompatible after incorporation

into the plasma membrane and could be efficiently labeled by introducing the already mentioned clicked chemistry with DBCO-dyes (Walter et al. 2017). When using bioorthogonal azide reactions these can either react *via* the Staudinger ligation, *via* copper-catalyzed or *via* copper-free strain-promoted cycloaddition. The Staudinger reaction exploits the selective reactivity of azides and phosphines which form an amide bond. The Staudinger reaction however, suffers from slow reactions kinetics which demand high triarylphosphine concentrations (Sletten and Bertozzi 2009). The other two reactions utilize the reaction of alkynes with azides to form triazoles. The first among these reactions, the Cu(I)-catalyzed azide-alkyne cycloaddition (Cu-AAC) is accelerated by the copper catalyst Cu(I), whereas the strain-promoted cycloaddition (SPAAC) applies cyclooctynes that are activated by a ring strain (Fig. 14).
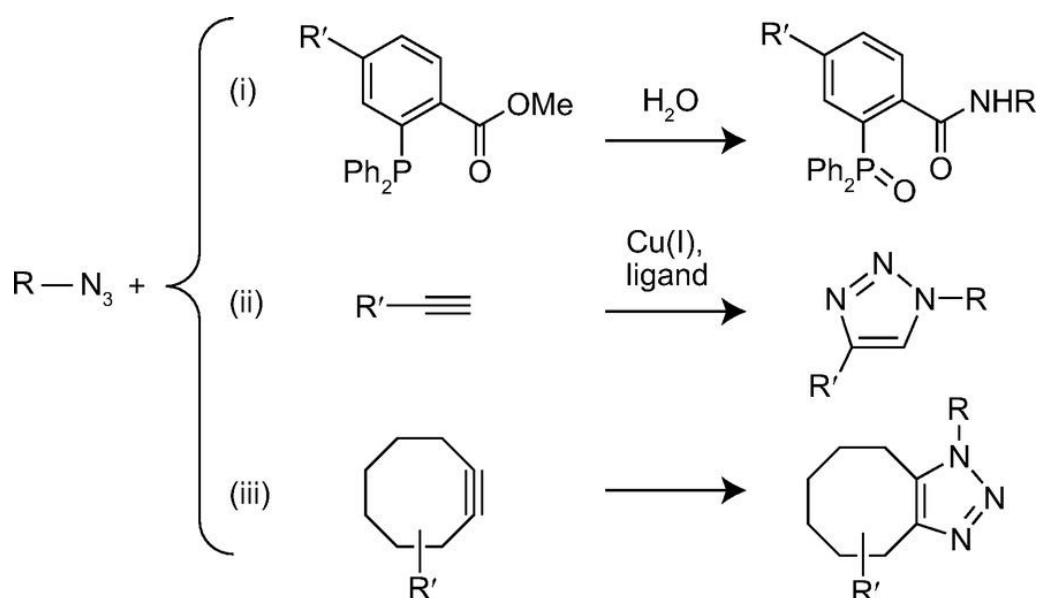
Figure 14 Bioorthogonal click-reactions involving azides. Azide reaction *via* (i) Staudinger ligation, (ii) copper catalysis and (iii) strain-promoted cycloaddition form ligated products. With permission from Agard et al. 2006. Copyright (2006) American Chemical Society.

Although highly efficient and fast, CuAAC always was strongly limited by the cytotoxicity of copper(I) which impeded its use in living cells: Therefore it was a huge improvement that SPAAC reactions overcame the cytotoxicity of the CuAAC reaction. The first SPAAC reactions were still considerably slower than CuAAC, but with discovery of difluorinated cyclooctyne (DIFO) (Baskin et al. 2007) and dibenzocyclooctyne (DBCO) (Debets et al. 2010) similar kinetics were enabled.

This principle of click chemistry was quickly adapted by chemists and biologists for the modification of ceramides with azides and used to visualize not only the ceramide integration into plasma membranes (Walter et al. 2016, Walter et al. 2017), but also ceramide distributions during bacterial infections (Elwell et al. 2011, Koch-Edelmann et al. 2017).

Albeit this dramatically promoted fluorescence imaging of sphingolipids, some limitations still remained. Lipids like sphingolipids are not fixable because most lipids do not bear a primary amine making it hard to apply additional immunofluorescences, especially when the cell membrane needs to be permeabilized. This also restricted the application of super-resolution imaging methods like *d*STORM which rely on the reconstruction of thousands of images over time and therefore dependent on completely fixed samples.

1.10 Objectives of this work

Within this work, super-resolution microscopy was used to visualize membrane receptors and intracellular pathogens. First, in order to visualize and quantify membrane receptors, we needed to establish a reliable staining protocol which allowed *d*STORM imaging of the basal membrane. Here, Jurkat T-cells were used as model cell line to study various receptors in one color. The next aim was to visualize two receptors with two different dyes, followed by receptor imaging using the same dye sequentially to allow quantitative multi-color imaging. To assess the applicability to primary T-cells, this protocol needed then to be tested with primary naïve and activated T-cells. Next, we aimed to quantify the clinically relevant receptors CD38 and BCMA after the treatment with various drugs to assure that changes within the receptor expression can be detected. Furthermore, the sensitivity of our approach needed to be addressed in comparison to flow cytometry using the receptor CD20 which is a target in immunotherapy. To evaluate an equal staining of the cell or artifacts in general whole cell imaging was also indispensable. Hence, LLS-3D *d*STORM and 10x ExM were applied to asses this and to visualize receptor distributions on the whole T-cell.

The improved resolution can also be used to visualize bacterial and fungal pathogens in ExM. First, ExM needed to be established to expand bacteria as modifications of the standard protocol might be required. Next, we wanted to extend the possible molecules that can be used in ExM which could be enabled by the introduction of only one primary amine. As model served ceramides during the infection by *Chlamydia*. Finally, we even planned to extend the applicability of ExM to fungi with the severe obstacle of the fungal cell wall. Here, the cell wall first had be digested to enable an isotropic expansion.

2 Materials and Methods

2.1 Cell culture

In this work the cell lines U2OS, Jurkat T-cells, HeLa 229 (ATCC CCL-2.1tm) and human epithelial conjunctival cells (Chang) were used. The U2OS cells were cultured in DMEM Ham's F12 supplied with 10% FCS, 100 U/ml penicillin and 0.1 mg/ml streptomycin at 37°C and 5% CO_2, while Jurkat T-cells were cultured in RPMI 1640 with the same additives. Cell culture of the U2OS cells and Jurkat T-cells was mainly performed by Lisa Behringer-Pließ und Petra Geßner, while the HeLa 229 and Chang cells were completely cultivated and seeded by Tobias C. Kunz from the Department of Microbiology. Primary cells were isolated and stimulated at the Medical Clinic and Policlinic II of the University Hospital of Würzburg by Dr. Thomas Nerreter.

2.2 Preparation of pathogens and fungi

HeLa 229 cells were infected with *Chlamydia trachomatis, Simkania negevensis* and *Neisseria gonorrhoeae* by Tobias C. Kunz. Infection with *C. trachomatis* was performed for 24 h, with *S. negevensis* for 72 h and with *N. gonorrhoeae* for 4 h.

Fungi were cultured by Sabine Panzer (*F. oxysporum* and *U. maydis*) and Nora Trinks (*A. fumigatus*). The *U. maydis* strains FB1 ΔUmOps1 pcrg-UmOps1::eGFP K1 and FB1 pcrg-UmOps1::eGFP KA (Panzer et al. 2019) were grown in potato dextrose broth pH 5.6 (PDB; Sigma P6685) for 15-24 h at 28°C and 100 rpm and seeded after harvesting and washing. If necessary, UmOps1::eGFP was induced by adding arabinose to the medium.

F. oxysporum f. sp. lycopersici race 2 strain 4287 microconidia (FGSC 9935) expressing H1-mCherry (Ruiz-Roldan et al. 2010) together with Lifeact-GFP (Riedl et al. 2008) were cultivated in PDB pH 9.0 for 4-7 days in 28°C at 120 rpm. Microconidia were harvested by filtration and washed with ddH_2O prior to seeding.

The transformed *Aspergillus fumigatus* strain AfS35 expressed mitochondria targeted mRFP together with sGFP and was cultivated in *Aspergillus* minimal medium. Harvesting of the spores was performed by subsequent submerging in PBS and resuspension using glass beads.

2.3 Immunofluorescence

2.3.1 Live cell staining

To perform a live cell immunostaining of plasma membrane receptors, 150 000 Jurkat T-cells per well were seeded on poly-D-lysine (PDL) precoated chambers (Lab-Tek II, Nunc, Thermo Fisher Scientific) or on PDL-coated coverslips and the cells were allowed to adhere for 1 h at 37°C and 5% CO_2. For coating, the chambers were incubated 1 h in 0.1 mg/ml PDL, subsequently washed three times with sterile PBS and air dried. If necessary, the chambers were precleaned prior to the PDL-coating with 1 M KOH for 10 min and after washing incubated for 15 min in EtOH. Directly prior to the staining, the cells were cooled 5 min on ice and then incubated for 45 min in the antibody (mostly 5 µg/ml, table 1) dissolved in PBS on ice. This was followed by three washing steps and a fixation of 15 min in 4% formaldehyde and 0.25% glutaraldehyde. In case of a biotinylated antibody the washing was followed by an incubation of 30 min in 0.1 mg/ml streptavidin-ATTO 643 (ATTO-TEC, AD 643-61), washing and the already described fixation. Hereafter, the cells were washed again and stored in PBS at 4°C until use. In case of a staining with DNA-conjugated antibodies the samples were blocked additionally in 5% BSA and 1 mg/ml single stranded salmon DNA (Sigma D9156-1ml) overnight at 4°C.

2.3.2 Immunofluorescence of fixed cells

For expansion experiments, 50 000 U2OS cells per well were seeded on a 12 mm or 15 mm coverslip, otherwise 20 000 cells per well were seeded on LabTek-chambers (Lab-Tek II, Nunc, Thermo Fisher Scientific) and allowed to grow overnight at 37°C at 5 % CO_2. In case of a tubulin-staining the seeded cells were fixed according to the cytoskeleton protocol using a cytoskeleton buffer (CB, 10 mM MES, 150 mM NaCl, 5 mM EGTA, 5 mM Glucose, 5 mM $MgCl_2$, pH 6,1) (Michie et al. 2017). In a first step, the cells were prefixed and permeabilized by an incubation for 1 min in prewarmed CB1 (CB supplied with 0.3% glutaraldehyde and 0.25% Triton X-100) followed by a second fixation in CB2 (CB supplied with 2% glutaraldehyde) for 10 min and three washing steps. Moreover, autofluorescence caused by glutaraldehyde was quenched by incubation of 7 min in 0.1% $NaBH_4$. After subsequent washing, unspecific binding was blocked by 5% BSA for 30 min and the antibody-staining was proceeded.

If no cytoskeleton staining was desired, the sample was fixed for 15 min in 4% formaldehyde and 0.25% glutaraldehyde or, if infected with bacteria, for 30 min in 4% PFA. After washing, the cells were permeabilized in 0.2% Triton X-100 for 15 min and washed again. Following this, the sample was blocked for 30 min in 5% BSA and the first antibody was applied for 1 h dissolved in 5% BSA. The cells were washed again and incubated for another hour in the

corresponding secondary antibody and washed. To preserve the staining, the cells were post-fixed for 10 min in 4% formaldehyde, washed and stored at 4°C until use.

The used antibodies are depicted in table 1.

Table 1 Used antibodies with the corresponding specifity, conjugate, applied concentration and manufacturer.

Type	Specifity	Conjugate	Concentration	Company
Primary antibodies	Anti-BCMA	Alexa Fluor 647	5 µg/ml	Biolegend, 357518
	Anti-CD105		5 µg/ml	Biolegend, 323202
	Anti-CD11a		5 µg/ml	Biolegend, 301218
	Anti-CD2		5 µg/ml	Biolegend, 309202
	Anti-CD20		5 µg/ml	Biolegend, 302302
	Anti-CD20	Alexa Fluor 647	5 µg/ml	Biolegend, 302318
	Anti-CD28		5 µg/ml	Biolegend, 302902
	Anti-CD3		5 µg/ml	Biolegend, 300402
	Anti-CD38	Alexa Fluor 647	5 µg/ml	Biolegend, 303514
	Anti-CD4		5 µg/ml	Biolegend, 357402
	Anti-CD45		5 µg/ml	Biolegend, 368502
	Anti-CD5		5 µg/ml	Biolegend, 300602
	Anti-CD69		5 µg/ml	Biolegend, 310902
	Anti-CD7		5 µg/ml	Biolegend, 343102
	Anti-Cdu1		10 µg/ml	
	Anti-CERT		10 µg/ml	Abcam, ab72536
	Anti-CPAF		10 µg/ml	Provided by G. Zhong, University of Texas
	Anti-GFP mouse		10 µg/ml	Abcam, ab1218
	Anti-HSP60		10 µg/ml	Santa Cruz sc-57840
	anti-*Neisseria gonorrhoeae*		25 µg/ml	US biological, N0600-02
	Anti-Prx3		6 µg/ml	Origene, TA322470
	Anti-mCherry		2 µg/ml	Abcam, ab167453
	Anti-α-tubulin		5 µg/ml	Abcam, ab18251

	Anti-β-tubulin		10 µg/ml	Sigma-Aldrich, T8328
	CD5-L17F12		5 µg/ml	Biolegend, 364002
	CD5-polyclonal		5 µg/ml	R&D Systems, AF1636-SP
	Isotype-mouse IgG1		5 µg/ml	Biolegend, 400102
	Isotype-mouse IgG2a		5 µg/ml	Biolegend, 401502
	Isotype-mouse IgG2b		5 µg/ml	Biolegend, 400302
	Isotype-rat IgG2b		5 µg/ml	Biolegend, 400602
	Anti-CD2	Biotin	5 µg/ml	Biolegend, 300204
	Anti-CD3	Biotin	5 µg/ml	Biolegend, 300404
	Anti-CD11a	Biotin	5 µg/ml	Biolegend, 301204
Secondary antibodies	ATTO 647N anti-mouse	ATTO 647N	10 µg/ml	Rockland, 610-156-121S
	ATTO 647N anti-rabbit	ATTO 647N	10 µg/ml	Sigma, 40839
	Alexa Fluor 488 Anti-mouse	Alexa Fluor 488	10 µg/ml	Thermo Fisher, A-11017
	Alexa Fluor 488 Anti-rabbit	Alexa Fluor 488	10 µg/ml	Thermo Fisher, A-11008
	Anti-mouse		10 µg/ml	Sigma, SAB3701063
	Anti-rabbit		10 µg/ml	Thermo Fisher, 31212

2.4 *d*STORM imaging

*d*STORM was carried out on a homebuilt widefield setup with an inverted microscope (Olympus IX-71) using an oil immersion objective (Olympus APON 60xO TIRF, NA 1.49). The setup is equipped with excitation lasers of the wavelengths 639 nm (Genesis MX639-1000, Coherent) and 514 nm (Genesis MX514-500, Coherent). To separate the excitation beam from the fluorescence, a dichroic beam splitter was used (ZT405/514/635rpc, Chroma) and the emission was additionally filtered by emission filters (Brightline HC 679/41 (Semrock) and Bright-Line HC 582/75 (Semrock)) in front of the EMCCD-cameras (iXon Ultra 897, Andor). *d*STORM imaging was performed in a switching buffer containing 100 mM ß-mercaptoethylamin pH 7.4 with integration times of 20 ms for 15 000 frames at laser densities of ~7 kW/cm². For two color measurements the pH of the switching buffer was adjusted to 7.7. The recorded images were reconstructed with rapidSTORM 3.3 (Wolter et al. 2012) and two color images were aligned with the Fiji plugin bUnwarpJ by an elastic transformation matrix using tetraspecks as landmarks.

2.5 DNA-exchange *d*STORM

This protocol follows Schueder et al. (Schueder et al. 2017) with various modifications for receptor imaging. The salmon DNA-preblocked samples were incubated in ~0.01 nM complementary dye conjugated DNA (IBA) dissolved in hybridization buffer for 10 min. After five washing steps gold beads (650 nm, Nanopartz) were introduced into the sample by the incubation for 10 min in a 1:50 dilution. After three more washing steps, *d*STORM imaging buffer was added, followed by *d*STORM imaging. Next, the dye-conjugated DNA was denatured and removed by the incubation for two times in 30% formamide for 5 min. After three more washing steps the next DNA-dye strand was introduced in hybridization buffer supplied with 1 mg/ml salmon DNA. This procedure of staining with complementary DNA and consequent removing was repeated until all targets were imaged. The whole procedure was performed with the sample on stage using solely a 1 ml pipette. Reconstructed images were aligned using the Fiji plugin bUnwarpJ with the gold beads as fiducials.

The used DNA-sequences are summarized in Table 2 with "A"-strands in 3'-5' and "B"-strands in 5'-3' direction.

Table 2 Sequences of the oligonucleotides used in DNA-exchange *d*STORM.

Oligonucleotide	Sequence
1A	TTC CTC TAC CAC-DBCO
1B	Alexa647-AAG GAG ATG GTG
2A	TAA CAT TCC TAA C-DBCO
2B	Alexa647- ATT GTA AGG ATT G
3A	AAT CCC TCA CCA-DBCO
3B	Alexa647-TTA GGG AGT GGT

2.6 Dye conjugation to antibodies

After buffer exchange to 100 mM NaHCO$_3$ using 0.5 ml 7 kDa Spin Desalting Columns (Thermo Fisher, 89882), 50 µg of the purified antibody were incubated at RT in 5 molar excess of the desired NHS-dye. Used NHS-dyes were Alexa Fluor 647-NHS (Thermo Fisher, A20106), Cy5-NHS (Sigma Aldrich, PA15131), ATTO 643-NHS (ATTO-TEC, AD643-31) and Alexa 532 (Thermo Fisher, A20101MP).

After 3 hours, unreacted dye was removed using 0.5 ml 7 kDa Spin Desalting Columns and the buffer was exchanged to PBS supplemented with 0.02 % NaN$_3$. To determine the degree of labeling (DOL), the absorption of the antibody and the dye was measured with a UV-vis spectrophotometer (Jasco V-650). The conjugated antibodies were stored at 4°C.

2.7 DNA conjugation to monoclonal antibodies

To conjugate oligonucleotides specifically to the Fc-fragment of antibodies, the Siteclick Antibody Azido modification Kit (Thermo Fisher Scientific, S20026) was used according to the manual. In short, after antibody concentrating and buffer exchange with 100 kDa Amicon columns (Merck, UFC510024), 200 µg of the desired antibody were incubated at 37°C for 6 h with ß-galactosidase. To add an azido group to the antibody, it was incubated at 30°C overnight in a mixture of UDP-GalNAz and GalT enzyme. Following purification the azido-modified antibodies were incubated in 5 molar excess of DBCO-DNA overnight at 25 °C. Unreacted DNA was removed using again 100 kDa Amicon columns.

2.8 Quantification of localization data

Localization data acquired in *d*STORM measurements was analyzed by a custom-made code by PD. Dr. Sören Doose written in Mathematica 11.1 (Wolfram Research Inc.). For the analysis of each *d*STORM image an appropriate region of interest within a cell was chosen to be clustered. For clustering, a DBSCAN clustering algorithm (Schubert et al. 2015) was applied to group detected localization. The parameters were chosen by scanning different parameters for the weakest dependency on the clustering set. However, in most cases suitable parameters were ε = 20 and minPoints = 3. To estimate the total number of molecules on a cell, the cells' surface was calculated estimating T-cells as a sphere. Using this surface and the cluster density acquired from the DBSCAN algorithm, the total cluster number was calculated. In total 10-60 cells were analyzed for each condition.

To determine a non-specific and a specific subpopulation of CD20 antibodies in the CD20-project, the density distributions were fitted with a one- or two component log normal distribution. This enabled the estimation of relative contributions of specifically and non-specifically bound antibodies (Nerreter et al. 2019).

2.9 Expansion microscopy

Stained samples were first modified to be incorporated into the hydrogel. To do so, the samples were either incubated in 0.25% glutaraldehyde for 10 min or overnight in 0.1 mg AcX dissolved in 100 mM $NaHCO_3$ at RT in a humidified chamber. This was followed by three washing steps and subsequently by the gelation of the sample. In case of a fourfold expansion a monomer solution containing 8.625% sodium acrylate (Sigma, 408220) 2.5% acrylamide (Sigma, A9926), 0.15% N,N′-methylenbisacrylamide, 2 M NaCl (Sigma, S5886) and 1x PBS with freshly added 0.2% ammonium persulfate (APS, Sigma, A3678) and tetramethylethylenediamine (TEMED, Sigma, T7024) was used. Hereby, a 75 µl droplet of the monomer solution was pipetted on Parafilm within a polymerization chamber and the on coverslips grown cells were placed on this droplet upside-down using tweezers. The gels were then allowed to polymerize for 1 h at RT.

If a tenfold expansion was desired, 1 ml of the monomer solution contained 0.267 g DMAA (Sigma, 274135) and 0.064 g sodium acrylate (Sigma, 408220) dissolved in 0.57 g ddH_2O. Prior to use, this solution was degassed for 45 min on ice and after the addition of 100 µl 0.036 g/l KPS (Sigma, 379824) the solution was degassed for another 15 min. Finally, for each mil-

liliter of monomer solution 4 µl TEMED were added and the gelation was carried out as described above with the difference that the gelation was first performed for 30 min at RT followed by 1.5 h at 37°C in a degassed and humidified chamber.

After gelation completion, the gels were cut in smaller pieces, transferred into digestion chambers and incubated in digestions buffer (50 mMmTris pH 8.0, 1 mM EDTA (Sigma, ED2P), 0.5 % Triton X-100 (Thermo Fisher, 28314) and 0.8 M guanidine HCl (Sigma, 50933)), containing 8 U/ml proteinase K (Thermo Fisher, AM2548) for 30 min to overnight. Digested samples were expanded in ddH$_2$O and the ddH$_2$O was changed hourly until the expansion saturated. After the expansion was completed, the gel size was measured using calipers and the expansion factor was determined by the gel size prior and after expansion. The expanded gels were stored at 4°C until use and chopped again prior to use. Imaging was performed in PDL-coated glass chambers (Merck, 734-2055).

2.10 Preparation of fungi

Fungal spores or sporidia were seeded on coverslips coated with PDL in 4-well culture plates. Sporidia were further processed after 30 min of sedimentation in distilled water while conidia were incubated for 18 h (*A. fumigatus*) or for 14-19 h (*F. oxysporum*) in media to allow germination. If indicated, the cell wall of living *U. maydis* sporidia was removed using an enzymatic mix (0.1 g lysing enzyme of *T. harzanium* (Sigma-Aldrich, L1412), 0.25 g driselase, (Sigma-Aldrich, D8037-1G) and 0.5 mg chitinase (Sigma-Aldrich, C6137-25UN) dissolved in 10 ml 0.7 M NaCl) from known protocols to generate protoplasts of *Fusarium fujikuroi* (Garcia-Martinez et al. 2015). Otherwise, the cell wall was removed after fixation, albeit prior to the antibody staining to enable sufficient antibody penetration. Membrane stainings and immunofluorescences were performed as described above.

2.11 Ceramide labeling

Seeded, adhered and, if indicated, infected cells were fed with 10 µM of either α-Amino-ω-Azido-C_6-ceramide, ω-Azido-C_6-ceramide or ω-Azido-sphingosine for 1 h at 37°C. In case of a chlamydial infection the ceramide-analogues were fed 23 hpi, in case of an infection by *Simkania* 71 hpi and in case of a neisserial infection the sphingosine-analogues were added directly before infection. Feeding was followed by a fixation in 4% PFA and 0.1% glutaraldehyde for 15 min and washing with PBS. Permeabilization was performed for another 15 min in 0.2% Triton X-100 and after subsequent washing the lipids were clicked by the incubation of 5 µm DBCO Alexa Fluor 488 (Jena Bioscience, CLK-1278-1) or 5 µM DIBO Alexa Fluor 488 (ThermoScientific, C20020) for 30 min at 37°C dissolved in HBSS. For antibody-staining the samples were washed and proceeded as described in an earlier chapter.

2.12 mCling labeling and staining

mCling was purchased at Biosyntan and labeled using a cysteine-maleimide reaction as previously published (Revelo et al. 2014). Hereby, 150 nmol mCling were incubated in 100 mM TCEP and 3 molar excess of ATTO 643-maleimide (ATTO-TEC, AD 643-45) under continuous shaking overnight at RT. The label product was separated from unreacted dye using HPLC (JASCO) and the concentration of the final label product was determined by a UV-vis spectrophotometer (JASCO, V-650). Adherent cells or fungi were stained by a live-cell incubation in 0.5 µM mCling ATTO 643 dissolved in media for 10 min at 37°C. Afterwards the cells were fixed and, if desired, further stained.

2.13 CLSM and SIM imaging

Confocal imaging was performed on an inverted microscope (Zeiss LSM700) equipped with 5 mW red laser (637 nm), a 5 mW green laser (555 nm) and a 10 mW blue laser (488 nm) or on a SP5 (TCS SP5, Leica). For SIM imaging a commercial Zeiss ELYRA S.1 SR-SIM was used and SIM images were reconstructed by the ZEN image-processing platform with a SIM module. In both cases a water-immersion objective (C-Apochromat, 63x 1.2 NA, Zeiss, 441777-9970) was used. The recorded images and z-stacks were processed with FIJI 1.51n (Schindelin et al. 2012) and IMARIS 8.4.1. Moreover, the molecules in expanded samples were counted using the IMARIS spot counting.

3 Results

This thesis is composed of two main parts based on super-resolved fluorescence imaging. First, we used *d*STORM for quantitative receptor imaging of Jurkat T-cells and primary T-cells. This was followed by the application of this method to three clinically relevant receptors, CD38, BCMA and CD20, to validate the sensitivity of *d*STORM and whole cell imaging with 3D-LLS dSTORM and 10x ExM.

Next, we expanded the applicability of ExM not only to bacterial and fungal pathogens. We also modified a C_6-ceramide which enabled its use in fourfold and tenfold ExM.

3.1 Receptor imaging and quantification

Within the first part of this thesis we quantitatively analyzed the basal membrane of Jurkat T-cells and primary T-cells using *d*STORM. Afterwards, this method was applied to three clinical examples to demonstrate not only the applicability, but also superior sensitivity of *d*STORM. This is followed by whole cell receptor imaging using 3D-LLS *d*STORM and 10x ExM.

### 3.1.1 Visualization and quantification of the "Receptome" on Jurkat T-cells

In this first project, we sought to approach the quantitative "Receptome", the entirety of all receptors on the plasma membrane, of Jurkat T-cells and primary T-cells with single molecule sensitivity. To start, the first important step was the selection of suitable plasma membrane antigens. However, as conventional methods including immunolabeling and flow cytometry are not sufficient due to their limited sensitivity (Zola 2004, Truneh and Machy 1987), we completed our antibody selection using data from mass spectrometry (Bausch-Fluck et al. 2015).

Next, we established a reliable protocol for super-resolution imaging of membrane antigens. A crucial step was the PDL-coating to allow suspension cells to adhere and to form an imageable basal membrane on the glass surface. Hereafter, Alexa Fluor 647 or Alexa Fluor 532 conjugated primary antibodies were used to stain the surface of living Jurkat T-cells in order to avoid artificial, by secondary antibodies induced receptor clustering (Stanly et al. 2016). Importantly, labeling was performed at 4°C to avoid antibody internalization and after washing, glutaraldehyde was used for fixation additionally to formaldehyde to minimize the residual mobility of the stained antigens (Tanaka et al. 2010). If the Jurkat T-cells were fixed prior to staining with aldehydes or methanol, this resulted either in a dramatically decreased fluorescence signal compared to the live-cell staining or in too high residual antigen mobility due to incomplete fixation. We assume that high aldehyde concentrations might heavily crosslink membrane pro-

teins resulting in also crosslinked epitopes which impedes antibody binding. To enable an exquisite signal-to-noise ratio and to selectively illuminate the basal plasma membrane of the T-cells, *d*STORM imaging was performed by total internal reflection fluorescence (TIRF) microscopy. The super-resolved *d*STORM images clearly uncovered a non-random receptor distribution of CD3, CD5 and CD7 in clusters with diameters ranging from 30 nm to even 300 nm (Garcia-Parajo et al. 2014, Lillemeier et al. 2010). All other investigated receptors (CD2, CD4, CD11a, CD28, CD45 and CD69) seemed to show a homogeneous distribution (Fig. 15 a-k). As negative controls we used the B-cell marker CD20 and CD105. Interestingly, we could detect a low antigen number of CD105-molecules in many Jurkat T-cells, whereas all T-cells were negative for CD20.

Besides constructing super-resolved images, rapidSTORM also generates a list of all fitted localizations which can be further analyzed. Repeated localizations (≥ 3) were grouped within a distance of 20 nm and assigned to single, antigen-bound antibodies using a density-based spatial clustering of applications with noise (DBSCAN) and a customized localization analysis written by Sören Doose. Application of this algorithm to selected unfolded basal membrane regions allowed us to reliably determine antigen densities with single molecule sensitivity of up to 100 cluster/µm² according to simulations. When using Alexa Fluor 647, this cluster analysis of 20-30 cells per antigen revealed strongly varying mean receptor densities with a standard error (SE) from 1.2 ± 0.6 receptors/µm² for CD4 to 31.5 ± 1.9 receptors/µm² for the highly abundant antigen CD45. The control experiments 0.3 ± 0.01 receptors/µm² for CD20 and 2.0 ± 0.2 receptors/µm² for CD105 could be detected (Fig. 15 l). This is in conformity with reports that CD105 is partially expressed on activated T-cells (Schmidt-Weber et al. 2005). When considering the mean diameter of ~10 µm of a Jurkat T-cell, this corresponds to ~99 CD20-molecules in our negative control. The isotype controls to determine unspecific antibody binding also resulted in 0.1 – 0.3 clusters per cell corresponding to 30 – 120 clusters per cell.
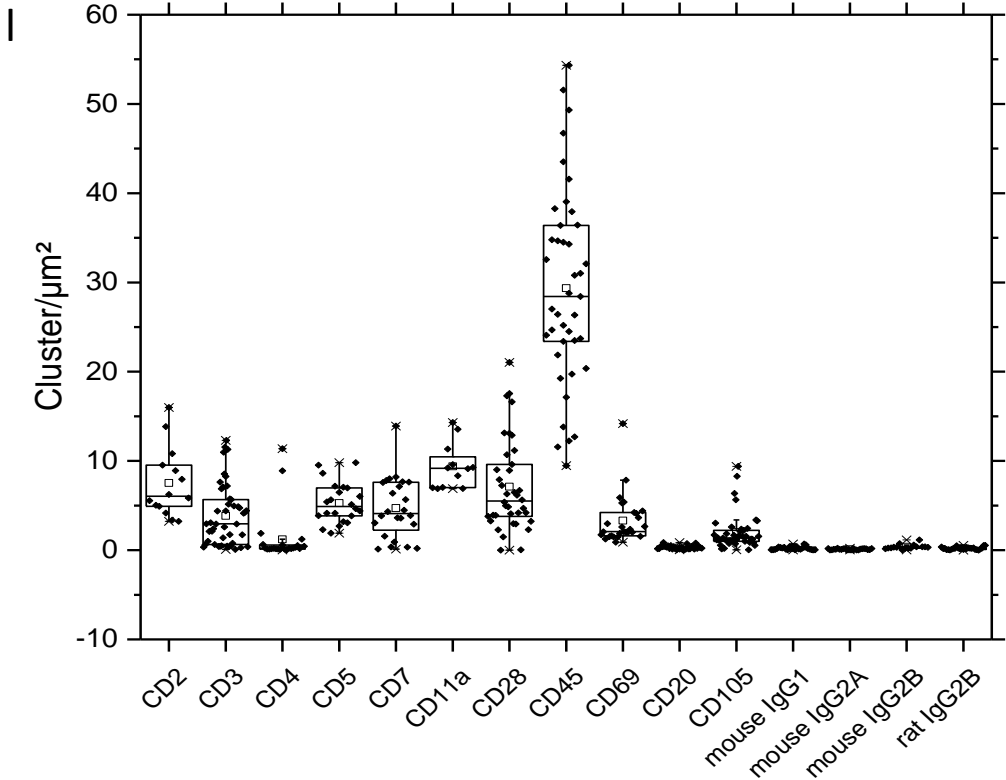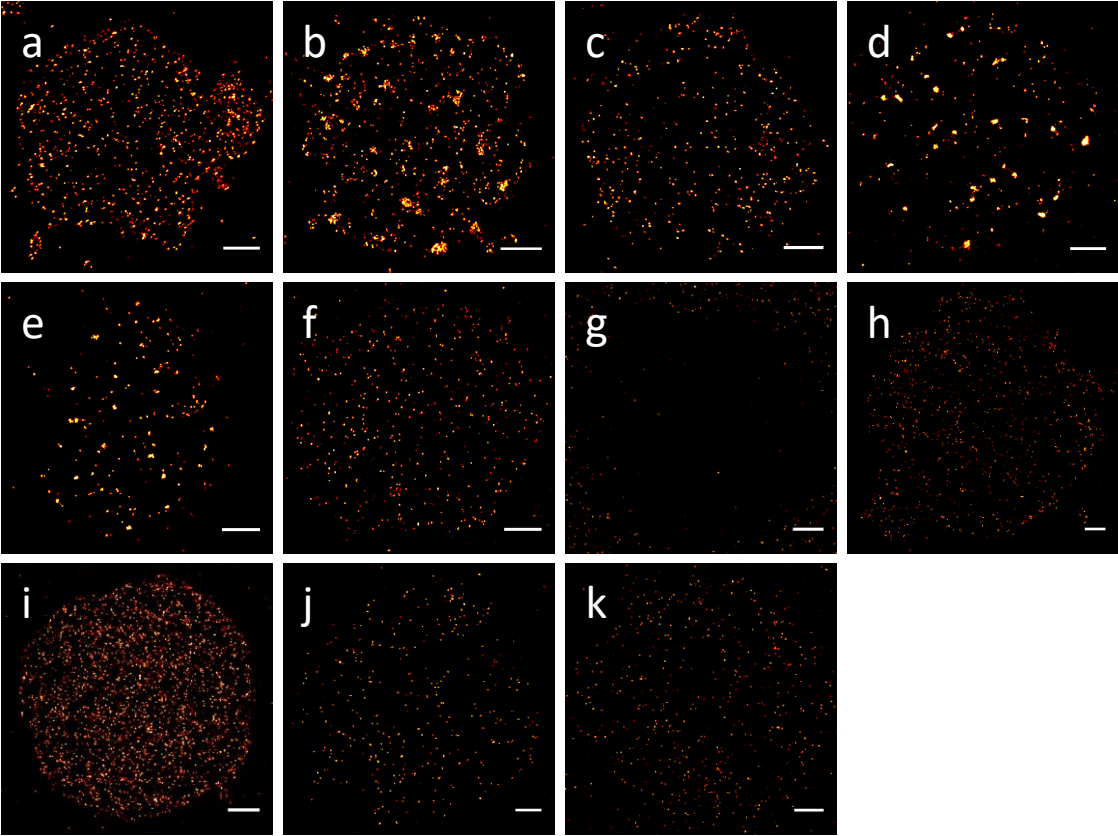
Figure 15 *d*STORM images of the basal membrane from Jurkat T-cells labeled with various antibodies conjugated with Alexa Fluor 647. Live-cell staining was performed on ice to avoid internalization followed by fixation. The *d*STORM images depict the receptors (a) CD2, (b) CD3, (c) CD4, (d) CD5, (e) CD7, (f) CD11a, (g) CD20, (h) CD28, (i) CD45, (j) CD69 and (k) CD105. (l) Boxplots represent receptor densities of up to ~55 receptors/µm². Scale bar, 1 µm.

We additionally analyzed the achieved localization precision in these experiments that ranged from 5.6 nm to 7.6 nm with a mean localization precision and a standard deviation (SD) in x-direction of 6.5 nm ± 0.7 and in y-direction of 6.6 nm ± 0.6 nm, summarized in table 3.

Table 3 Mean localization precision of Alexa Fluor 647 during *d*STORM experiments of the plasma membrane receptors CD2, CD3, CD4, CD5, CD7, CD11a, CD20, CD28, CD45 and CD69. The localization precision ranges between 5.6 nm and 7.6 nm

| Receptor	X-direction [nm]	Y-direction [nm]
CD2	7.3	7.6
CD3	6.1	6.5
CD4	5.8	6.5
CD5	7.0	7.2
CD7	7.0	6.3
CD11a	5.6	5.7
CD20	7.3	7.3
CD28	6.7	7.1
CD45	5.7	6.4
CD69	6.2	5.9

To exclude labeling and imaging artifacts, we performed *d*STORM experiments of the homogeneously distributed CD45 and the clustered CD5 at various antibody concentrations (Baumgart et al. 2016). Here, the cluster diameter determined by the convex hull was nearly independent of the antibody concentration (0.1 to 10 µg/ml) for both antigens (Fig. 16). Additionally, we titrated all antibodies in separate experiments to assure the saturation of all by the antibodies accessible antigen epitopes. Hereby, we could show epitope saturation for all antibodies at 5 µg/ml (Fig. 17).
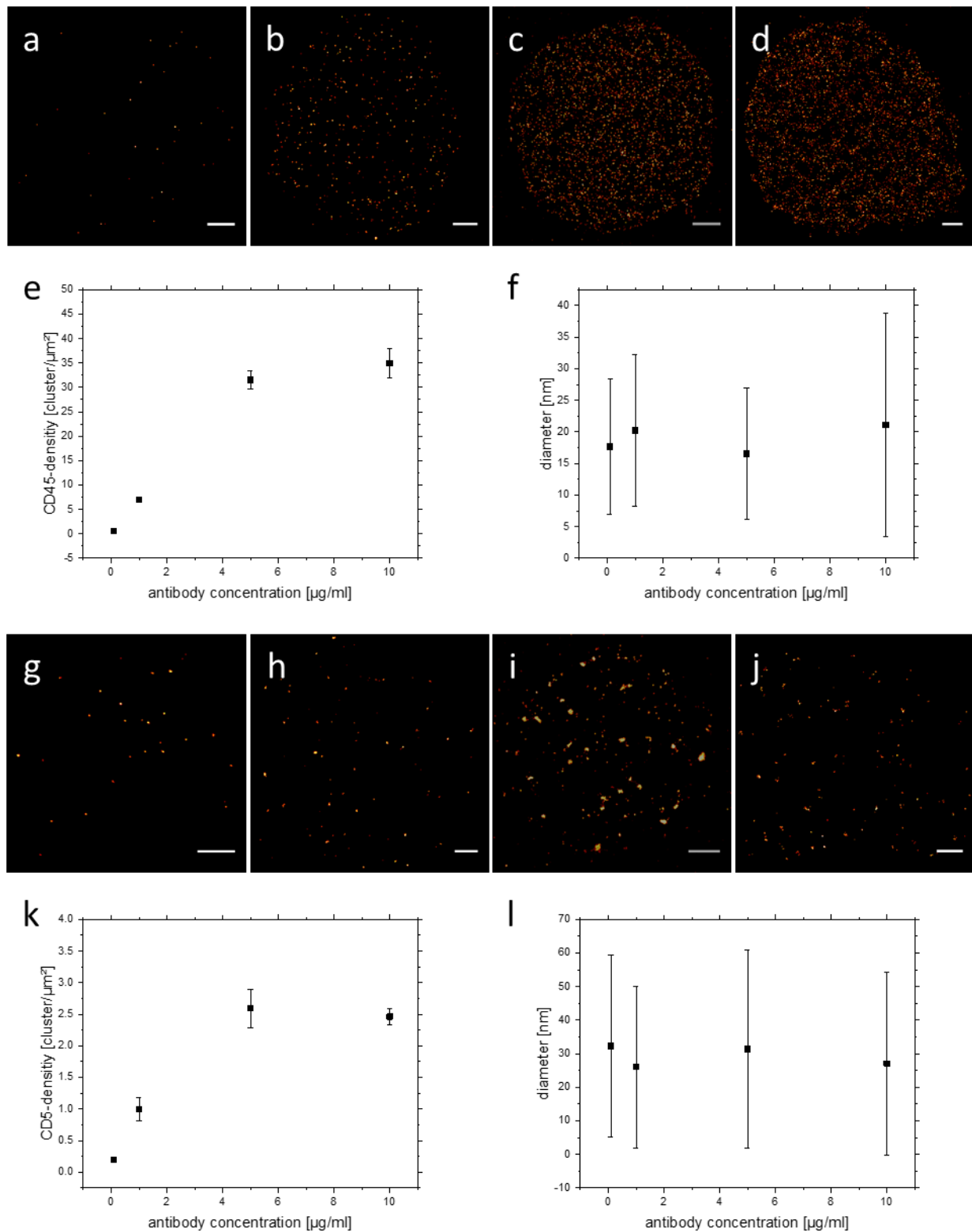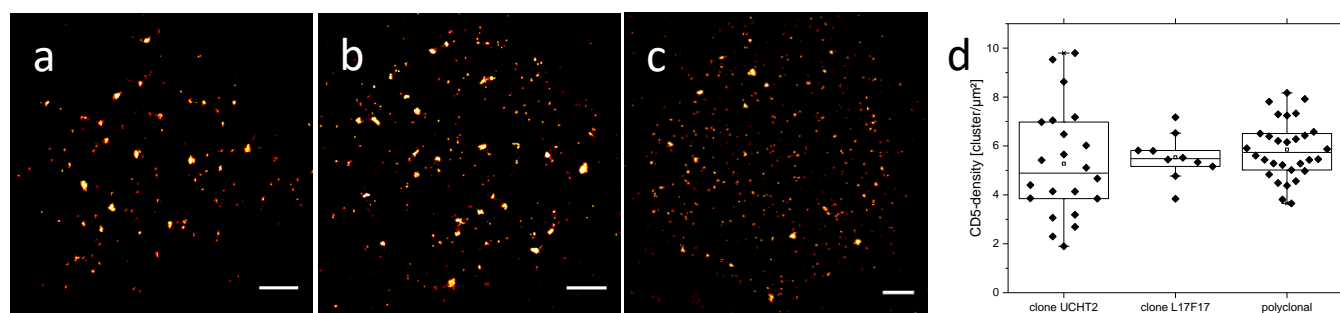
Figure 16 *d*STORM images of the antibody titration (anti-CD5 and anti-CD45) to visualize and quantify the effect of the antibody concentration on the receptor density and cluster size. (a-e) CD45 shows an increasing signal with increasing antibody concentration which saturates at ~ 5µg/ml. (f) Analysis of the CD45-clusters diameter demonstrates a constant cluster size with varying antibody concentration. (g-k) Similarly CD5-cluster-densities increase with increasing antibody concentration until they saturate at ~5 µg/ml. (l) The CD5-cluster diameter remains nearly independent of the antibody concentration. In (e and k) the corresponding standard error and in (f and l) the standard deviation is shown. Scale bar, 1 µm.
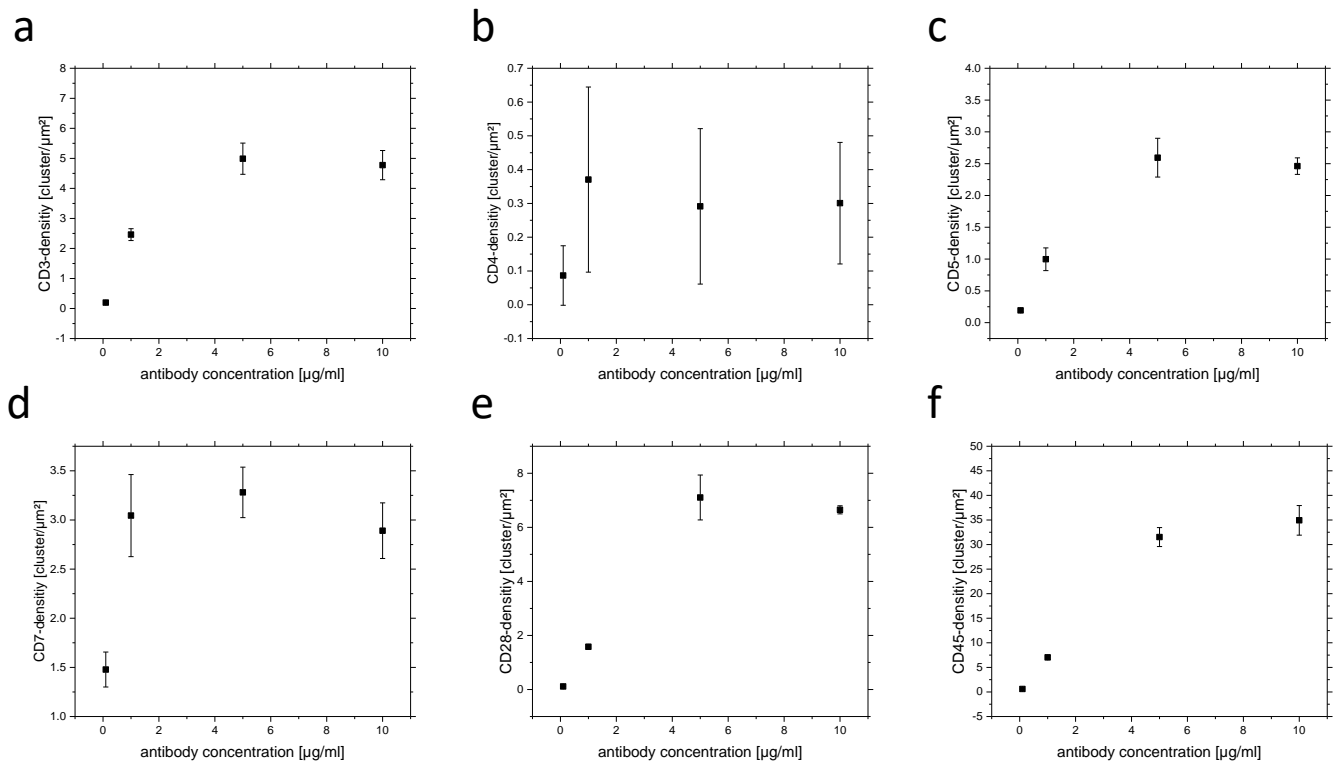
Figure 17 Antibody titration confirms the saturation of all accessible antigens on the basal plasma membrane of Jurkat T-cells. Quantification of the membrane receptor densities acquired from dSTORM experiments with various antibody concentrations of antibodies directed against (a) CD3, (b) CD4, (c) CD5, (d) CD7, (e) CD28 and (f) CD45. The error bars resemble the corresponding standard error.

Additionally, we evaluated the influence of the accessibility of different epitopes on the plasma membrane. Therefore, we selected two different monoclonal antibodies (clones L17F12 and UCHT2) binding to independent epitopes and a polyclonal antibody directed against CD5. Both, the super-resolved dSTORM images and the cluster analysis, showed very similar results and we calculated a receptor density of ~5.5 CD5-cluster/µm² for all three antibodies. This revealed an equal accessibility of CD5 molecules for these antibodies and demonstrates that at least in this case epitope accessibility does not impede antigen quantification (Fig. 18). Moreover, we performed various two-color dSTORM experiments. Two-color experiments, however, are always a compromise in terms of the ideal switching buffer for the used dyes. The two-color images showed similar receptor distributions compared to the single color experiments (Fig. 19).

Figure 19 *d*STORM images of the basal membrane from Jurkat T-cells live-cell stained with different monoclonal and polyclonal antibodies directed against CD5. Reconstructed dSTORM images of the monoclonal antibody (a) clone L17F12, (b) clone (UCHT12) and the (c) polyclonal antibody result all in comparable images of CD5. (d) Quantification demonstrates only minor differences within the CD5 densities using antibodies binding to independent epitopes. Scale bar, 1 μm.
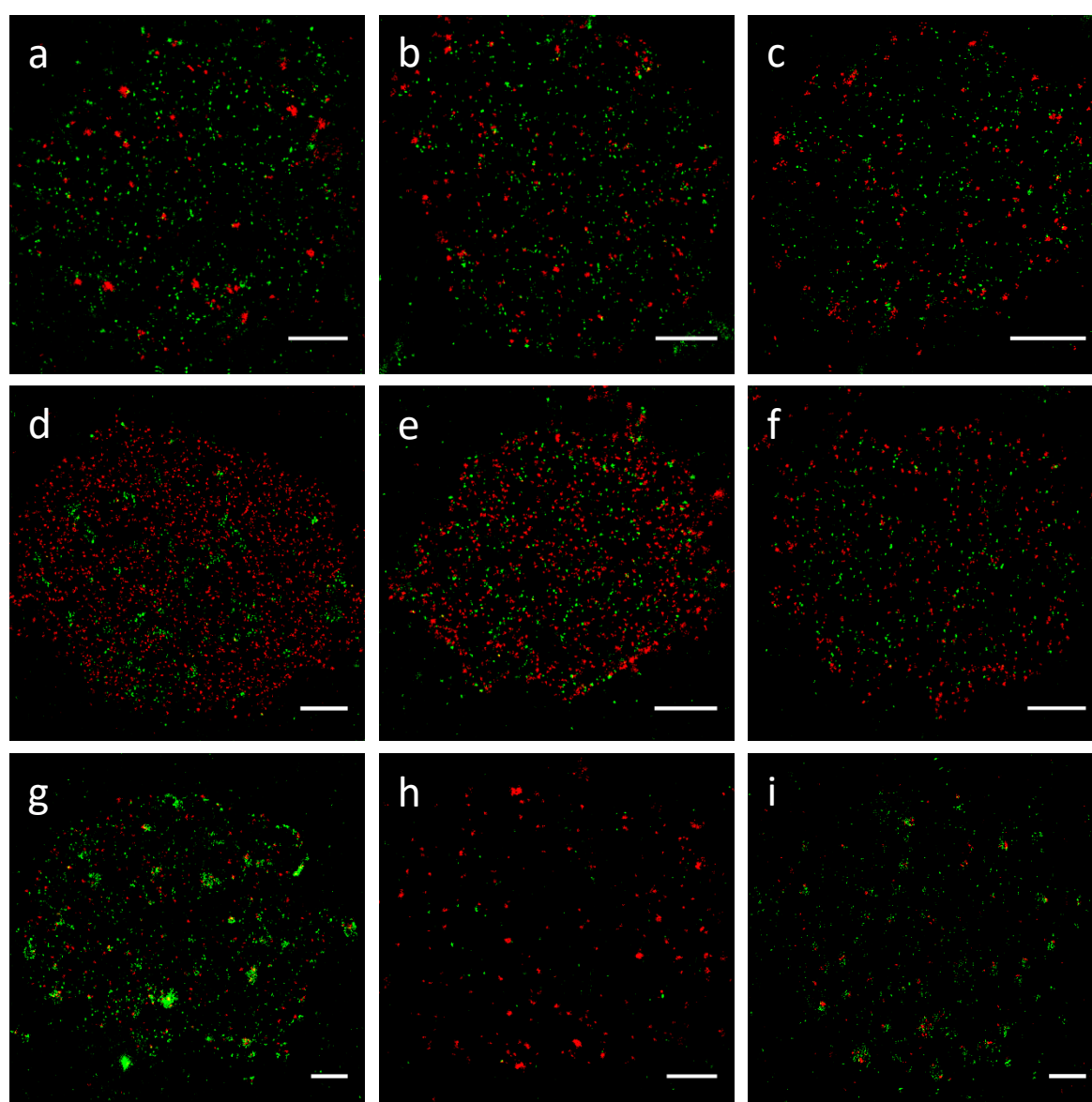

Figure 18 Two-color *d*STORM images of the basal membrane of live-cell stained Jurkat T-cells using Alexa Fluor 647 (red) and Alexa Fluor 532 (green). The *d*STORM images depict CD2 and CD5 (green and red; a), CD2 and CD7 (green and red; b), CD2 and CD28 (green and red; c), CD3 and CD45 (green and red; d), CD2 and CD45 (green and red; e), CD2 and CD45 (red and green; f), CD3 and CD7 (green and red; g), CD5 and CD7 (red and green; h) and CD3 and CD5 (green and red; i). Scale bar, 1 μm.

Analyzing the blinking rates, we could detect differences between the two dyes as each antibody labeled with Alexa Fluor 647 or Alexa Fluor 532 was localized on average 9.3 ± 2.1 (SD) and 7.6 ± 1.2 times. Moreover, Alexa Fluor 532 emits less photons with a worse signal-to-noise ratio resulting in a worse localization precision with mean 8.4 nm ± 0.3 in the x-direction and 9.5 nm ± 0.3 in the y-direction (table 4) compared to Alexa Fluor 647.

Table 4 Mean localization precision of Alexa Fluor 532 during *d*STORM experiments of the plasma membrane receptors CD2, CD3, CD7 and CD45. The localization precision ranges between 8.1 nm and 9.8 nm.

| Receptor	X-direction [nm]	Y-direction [nm]
CD2	8,8	9,2
CD45	8,1	9,4
CD7	8,2	9,7
CD3	8,3	9,8

As a next step, we evaluated the quantifiability of Alexa Fluor 532. Unfortunately, only Alexa Fluor 647, the most reliable *d*STORM-dye, was shown to provide truly quantifiable results (Löschberger et al. 2014). To address this, we compared the quantification results of Alexa Fluor 647 and Alexa Fluor 532 coupled anti-CD45 antibodies under identical imaging conditions. Here, Alexa Fluor 532 showed only approximately 55% CD45-Cluster/µm² compared to Alexa Fluor 647 (~16 to ~29 CD45-Cluster/µm^2; *p*-value = 2.8*10^{-6}, Fig. 20).
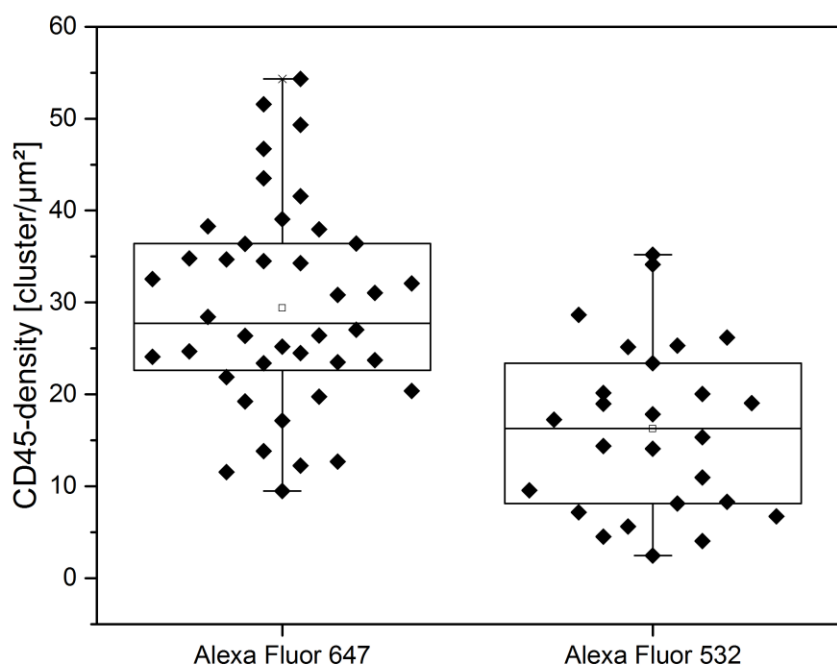
Figure 20 Quantification of CD45 on Jurkat T-cells acquired from *d*STORM experiments with Alexa Flour 647 or Alexa Flour 532. Comparison of the calculated CD45-densities reveals a decreased density of 55% of Alexa Fluor 532 compared to Alexa Fluor 647.

As these results clearly demonstrate that Alexa Fluor 647 outperforms the second best *d*STORM-dye Alexa Fluor 532 in quantification experiments, we decided to use Alexa Fluor 647 sequentially. A suitable method for this is DNA-exchange *d*STORM (Schueder et al. 2017) because this method fulfills several requirements for quantification experiments: First, the method has to be compatible with live-cell staining as staining after fixation will result in severe signal loss. Additionally, the method should enable sequential imaging with Alexa Fluor 647 of a "limitless" number of targets. Ideally, each round of imaging should also be as fast as possible to gain robust quantification statistics. All these requirements are combined by DNA-exchange *d*STORM (Schueder et al. 2017), so we decided to conjugate 12 - 13 bp long oligonucleotides to primary antibodies. However, labeling *via* biotin-streptavidin, unspecific amine-NHS-reactions and thiol-maleimide-reactions resulted in either unspecific or insufficient signals.

Hence, we chose a specific enzymatic antibody conjugation procedure. Hereby, the carbohydrates present on all IgG antibodies' Fc-fragments are modified *via* a ß-galactosidase while a modified galactose-transferase enables a side-specific azido-modification. Afterwards, DBCO-oligonucleotides can efficiently be "clicked" to those azides in a SPAAC-reaction resulting in antibodies conjugated with ~2 oligonucleotides. Another critical step to enable a specific staining was the blocking of unspecific binding to the glass surface of the DNA-dye with salmon-DNA. After solving these issues, pseudo 3-color exchange *d*STORM images of CD2, CD3 and CD28 on the basal plasma membrane of Jurkat T-cells could be acquired (Fig. 21 a). Importantly, using this protocol both receptor distributions and densities of CD2, CD3 and CD28 did not differ significantly using DNA-exchange *d*STORM compared to single-color measurements (Fig. 21 b). This demonstrates that DNA-exchange *d*STORM can successfully be applied for quantitative multi-color receptor imaging.
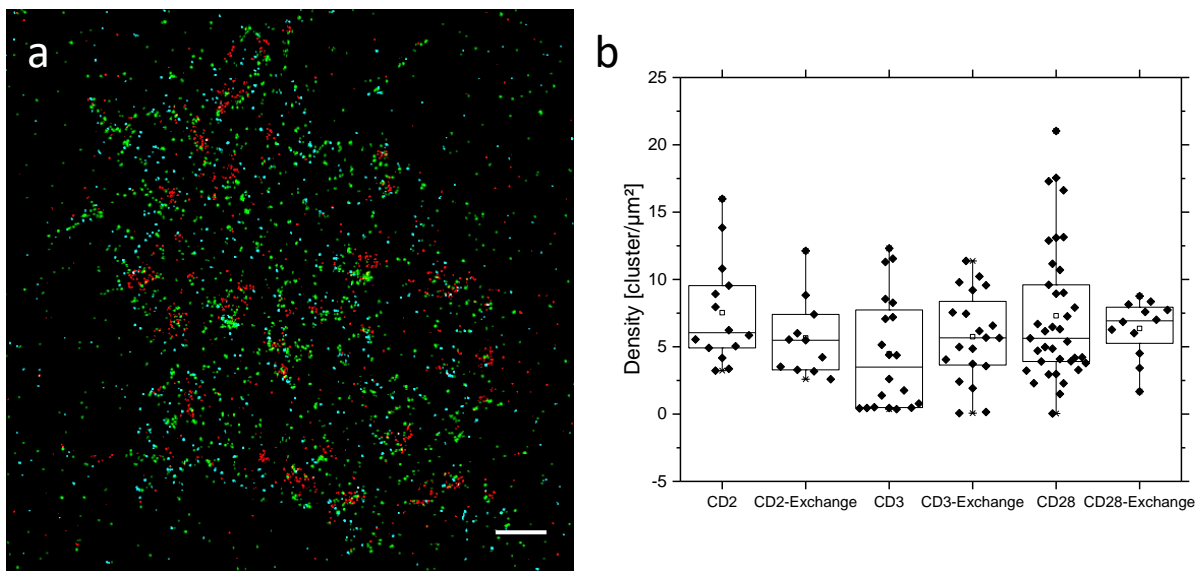

Figure 21 DNA-exchange *d*STORM of sequentially imaged CD2 (cyan), CD3 (red) and CD28 (green) on the plasma membrane of Jurkat T-cells. (a) Three-color exchange *d*STORM image. Scale bar, 1 µm. (b) Receptor quantification and comparison to single color and DNA-exchange *d*STORM experiments results in similar receptor densities.

3.1.2 Visualization and quantification of membrane receptors in primary T-cells

Additionally to Jurkat T-cells we were also interested in the receptor distribution and densities of primary T-cells, as only these can shed light on the receptor densities in healthy humans. Hence, we imaged the plasma membrane of both, CD4$^+$ and CD8$^+$, naïve and activated primary T-cells of healthy donors with our established antibody library. In naïve T-cells we could detect a heterogeneously clustered receptor distribution solely in case of CD7, while all other receptors appeared homogeneously distributed (Fig. 22). Within the negative controls CD20 and CD105, no specific staining could be detected besides of CD20 in activated CD8$^+$ T-cells. Moreover, the receptor densities ranged between mean 0.8 cluster/µm² for CD20 and 81.4 cluster/µm² in case of the highly abundant CD45. Overall, the receptor densities were similar when comparing CD4$^+$ and CD8$^+$ T-cells, with the difference that CD3 seemed to be stronger expressed in CD4$^+$ sorted T-cells with mean 37.4 ± 2.6 cluster/µm² (SE) compared to CD8$^+$ primary T-cells with 15.5 ± 3.6 cluster/µm². When comparing the receptor densities from primary naïve T-cells, it was obvious that most receptors were drastically higher expressed in primary T-cells than in Jurkat T-cells.

Upon activation *via* CD3 and CD28 the receptor densities in both, CD4$^+$ and CD8$^+$ sorted T-cells, changed (Fig. 23). Mostly the receptor densities of the T-cell activation marker CD2 and CD69 increased, with an increase of 45% from mean 37.4 cluster/µm² to 54.3 cluster/µm² in case of CD2 and a dramatic increase of ~500% in the expression level of CD69 from 2.6 cluster/µm² to 13.3 cluster/µm². After activation the receptor distribution ranged from 6.9 cluster/µm² for CD28 to 62.1 cluster/µm² for CD45. It should also be noted that the CD3 density of activated CD4$^+$ T-cells was decreased, presumably due to CD3-clustering, while only few other differences occurred between CD8$^+$ naïve and activated cells. When considering the literature, we could confirm that CD20 was only partially expressed, while no CD105-positive cells were detected (Schuh et al. 2016, Schmidt-Weber et al. 2005). Hereby, only 33% of activated CD8$^+$ T-cells expressed CD20 with on average 0.8 ± 0.09 molecules/µm² (SE) corresponding to mean 430 ± 514 molecules on the whole cell. In all other T-cell populations neither CD20 nor CD105 could be detected. To compare the total number of antigens within the plasma membrane between Jurkat T-cells and primary T-cells, it was necessary to extrapolate the calculated receptor densities. For this, T-cells were assumed to be a sphere which allowed the calculation of the total membrane surface by the mean diameter of the cells. For Jurkat T-cells the mean diameter was 10.0 ± 1.5 µm (SD) while the naïve primary T-cells had a mean diameter of solely 5.3 ± 0.6 µm and the activated primary T-cells a mean diameter of 8.9 ± 1.1 µm. This resulted in mean T-cell surfaces of 322 ± 92.3 µm², 90 ± 22.5 µm² and 251 ± 59.5 µm² and together with the receptor densities, the total molecules per cell could be calculated. The summary of these estimations is depicted in table 5.
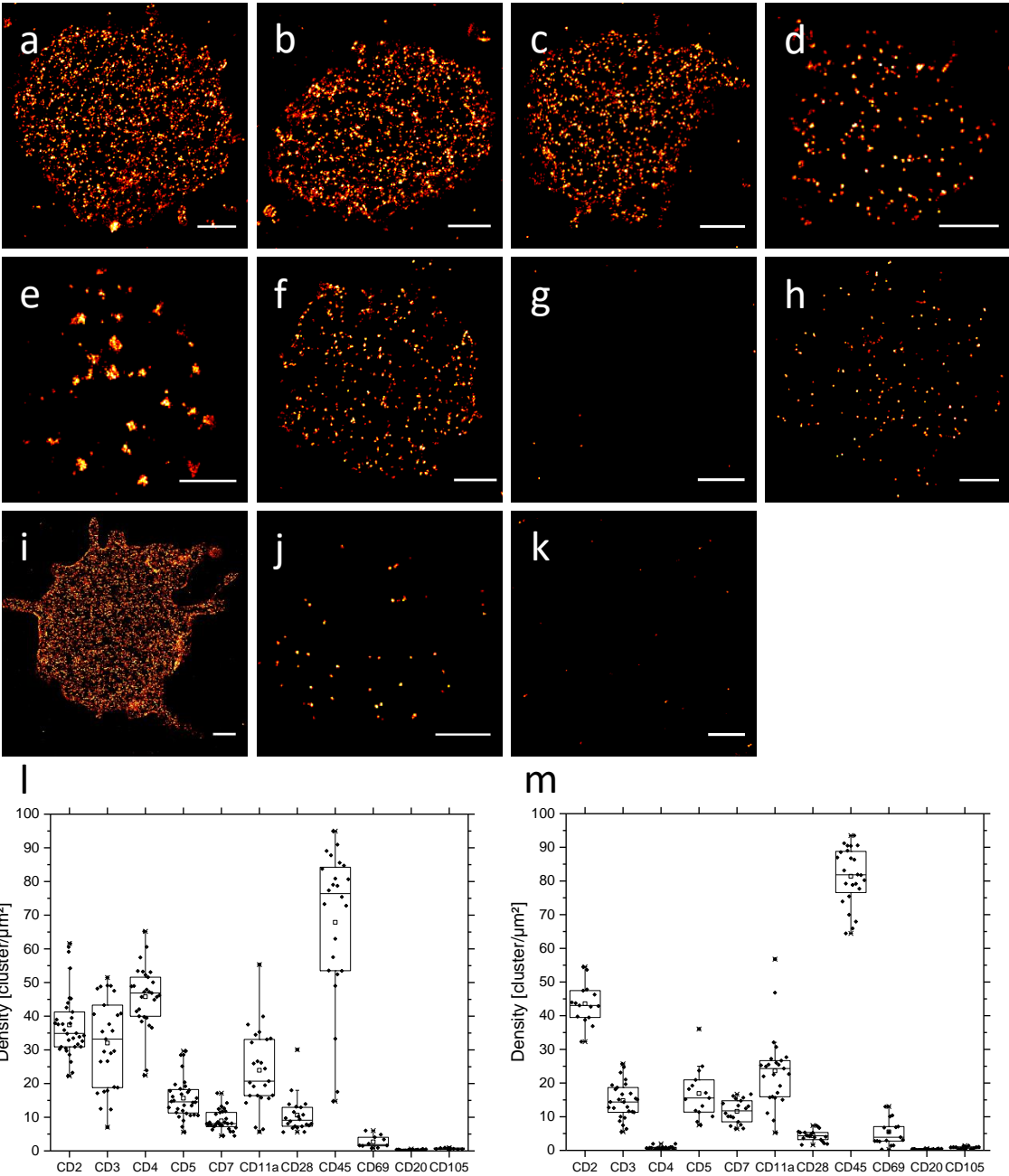
Figure 22 *d*STORM images of (a-k) primary naïve CD4⁺ and CD8⁺T-cells and quantification of the receptor densities of (l) CD4⁺ and (m) CD8⁺ T-cells. T-cells were stained for (a) CD2, (b) CD3, (c) CD4, (d) CD5, (e) CD7, (f) CD11a, (g) CD20, (h) CD28, (i) CD45, (j) CD69 and (k) CD105. Mostly CD7 seems to form clusters while the other receptors were homogeneously distributed. Quantification of the receptor densities demonstrate only minor differences between naïve (l) CD4⁺ and (m) CD8⁺ T-cells. Scale bar, 1 µm.
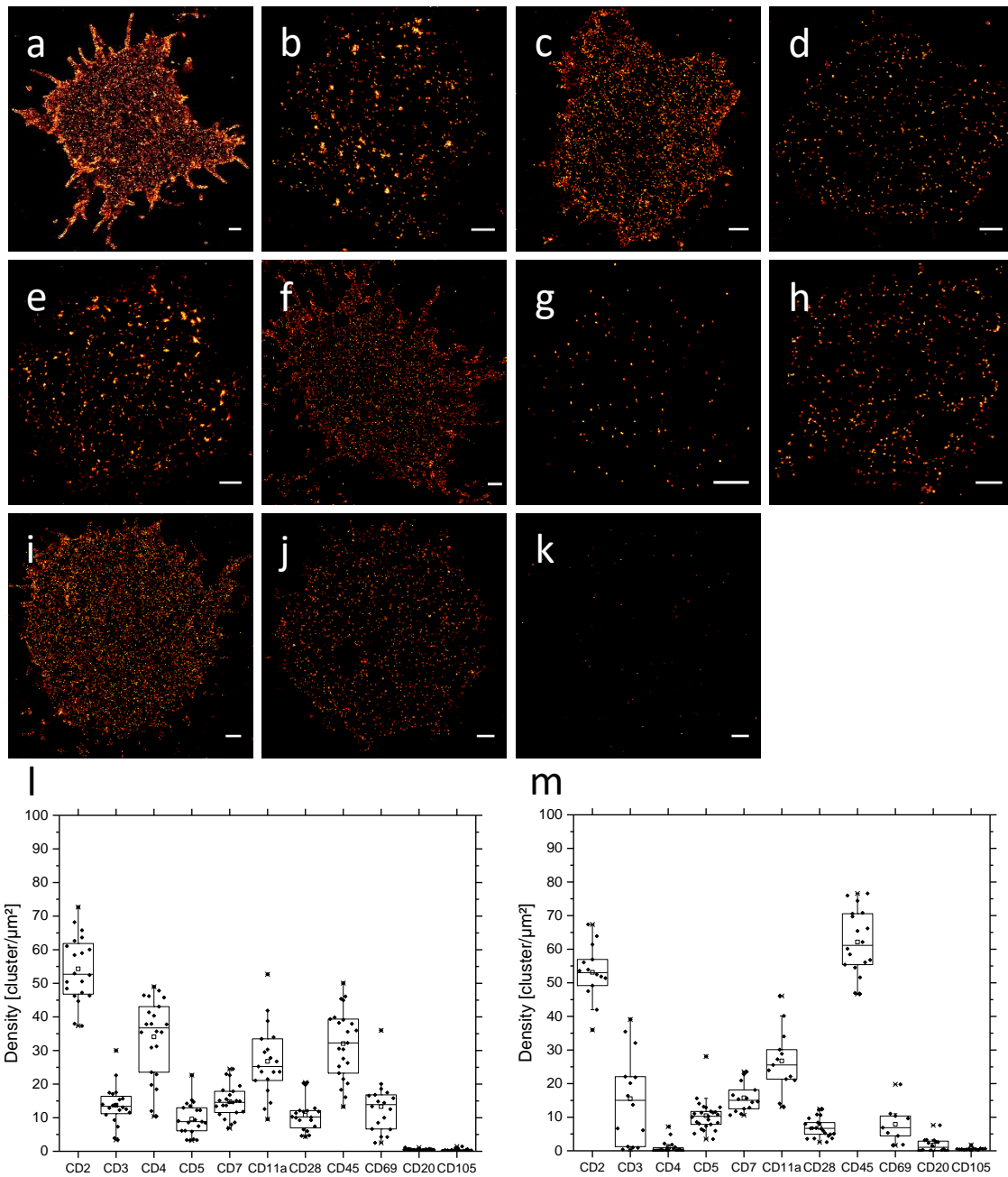
Figure 23 *d*STORM images of (a-k) primary activated CD4+ and CD8+ T-cells and quantification of the receptor densities of (l) CD4+ and (m) CD8+ T-cells. T-cells were stained for (a) CD2, (b) CD3, (c) CD4, (d) CD5, (e) CD7, (f) CD11a, (g) CD20, (h) CD28, (i) CD45, (j) CD69 and (k) CD105. CD3, CD7 and slightly CD28 appear in clusters while the other receptors seem unclustered. Quantification of the receptor densities demonstrates few differences between activated (l) CD4+ and (m) CD8+ T-cells. Scale bar, 1 µm.

Table 5 Extrapolated total mean antigen numbers with the corresponding standard deviation from *d*STORM experiments of whole Jurkat T-cells and primary T-cells.

|	Jurkat T-cells	Naïve CD4^{+}	Naïve CD8^{+}	Activated CD4^{+}	Activated CD8^{+}
CD2	2426 ± 1254	3365 ± 877	3918 ± 532	13630 ± 2464	13332 ± 2066
CD3	1440 ± 1353	2881 ± 1196	1329 ± 482	3443 ± 1491	3891 ± 3383
CD4	393 ± 924	4120 ± 833	64 ± 47	8548 ± 2907	257 ± 465
CD5	1700 ± 722	1407 ± 535	1520 ± 672	2404 ± 1241	2623 ± 1189
CD7	1520 ± 1096	802 ± 264	1043 ± 312	3712 ± 1178	3956 ± 1053
CD11a	3025 ± 814	2153 ± 1057	2125 ± 981	6718 ± 2631	6709 ± 2362
CD20	99 ± 70	21 ± 13	69 ± 29	108 ± 51	430 ± 514
CD28	2290 ± 1648	954 ± 482	396 ± 150	2700 ± 1220	1746 ± 729
CD45	9464 ± 3554	6110 ± 2061	7325 ± 762	8048 ± 2599	15595 ± 2395
CD69	1064 ± 887	241 ± 161	497 ± 364	3335 ± 1965	1978 ± 1419
CD105	650 ± 649	60 ± 19	76 ± 31	78 ± 90	145 ± 93
Mouse IgG1	69 ± 58				
Mouse IgG2A	35 ± 19				
Mouse IgG2B	119 ± 86				
Rat IgG2A	68 ± 45				

3.1.3 Clinical application
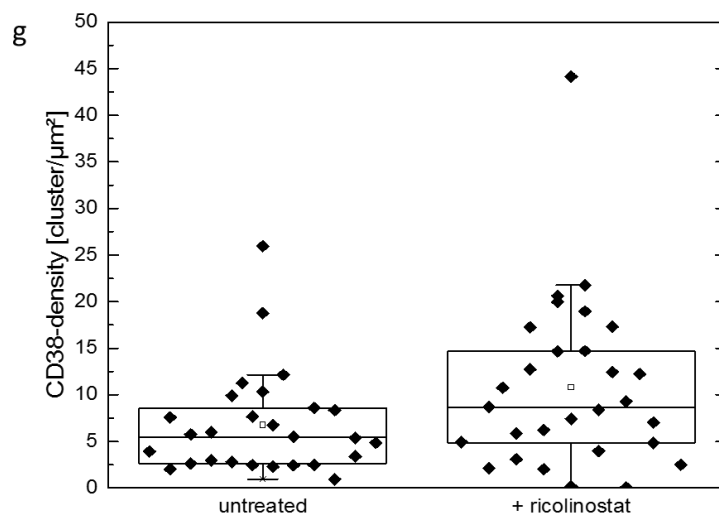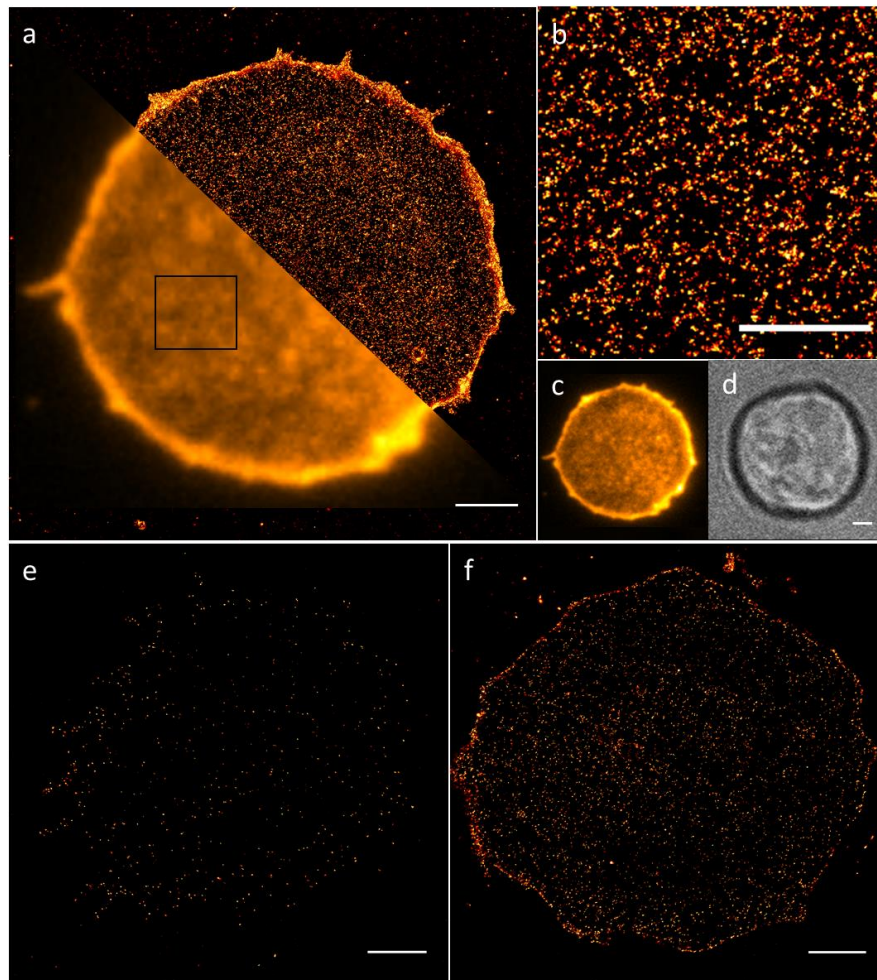
3.1.3.1 Quantification of CD38 in multiple myeloma cells

After establishing our protocol to quantify plasma membrane receptors, we applied this method in clinical relevant questions. The CD38- and the following BCMA-project were performed in collaboration with Dr. Sophia Danhof and Dr. Michael Hudecek. Our first target was the receptor CD38 which is highly expressed in multiple myeloma. CD38 serves as target for the monoclonal antibody daratumumab which induces good responses in patients, especially in combination with other drugs (Lonial et al. 2016, Palumbo et al. 2016, Dimopoulos et al. 2016). However, during treatment with daratumumab, CD38 is often downregulated in multiple myeloma cells (Nijhof et al. 2016). Hence, various drugs are in development to increase CD38-expression specifically in multiple myeloma cells, among them ricolinostat (rico) (Vogl et al. 2017), a specific inhibitor of histone deacetylase 6. For comparison, we treated MM1.S cells not only with ricolinostat, but also with the already established and approved drugs ATRA (Nijhof et al. 2015) and panobinostat (pano) (Garcia-Guerrero et al. 2017). To clearly identify myeloma cells, the sample was additionally stained with anti-CD138 FITC. Interestingly, in MM1.S cells we could detect the highest increase of the homogeneously distributed CD38 (Fig. 24) after exposure to 5 µM ricolinostat (55.5 ± 2.6 cluster/µm²; SE, p-value = $1.5*10^{-7}$) compared to 10 nM ATRA (46.1 ± 2.0 cluster/µm², p-value = 0.002), 25 nM panobinostat (49.1 ± 2.2 cluster/µm², p-value = $1.2*10^{-4}$) and the untreated control (37.0 ± 2.0 cluster/µm²) using dSTORM and our quantification software (Fig. 24 e). Extrapolating these cluster-densities using again the cells diameter resulted in mean 4397 ± 1699 molecules per cell (SD) in untreated cells, 5190 ± 1601 molecules per cell after MM1.S cells were treated with ATRA, 5115 ± 1628 molecules per cell following treatment with panobinostat and 5871.5 ± 1907.9 molecules per cell after ricolinostat treatment. The efficacy of ricolinostat could also be shown in primary multiple myeloma patient cells. First, we investigated the compatibility of primary multiple myeloma cells with dSTORM by applying our established protocol. Indeed, using this protocol we could successfully visualize the basal membrane stained with an anti-CD38 antibody (Fig. 25). Quantification of CD38-molecules on these primary cells yielded in a CD38-cluster-density of 75.3 ± 3.0 cluster/µm² (SE).Consequently, we investigated primary myeloma cells from a patient who had undergone daratumumab treatment. Compared to previously untreated multiple myeloma patient cells, we could detect a severely decreased CD38-density on daratumumab treated myeloma cells (6.8 ± 1.1 cluster/µm²). This is in agreement with reports that during daratumumab treatment CD38 is often downregulated (Nijhof et al. 2016). Upon treatment with ricolinostat the CD38-expression of previously daratumumab treated patients could be stimulated by 59% to 10.8 ± 1.7 CD38 cluster/µm² (p-value = 0.05, Fig. 25 g).
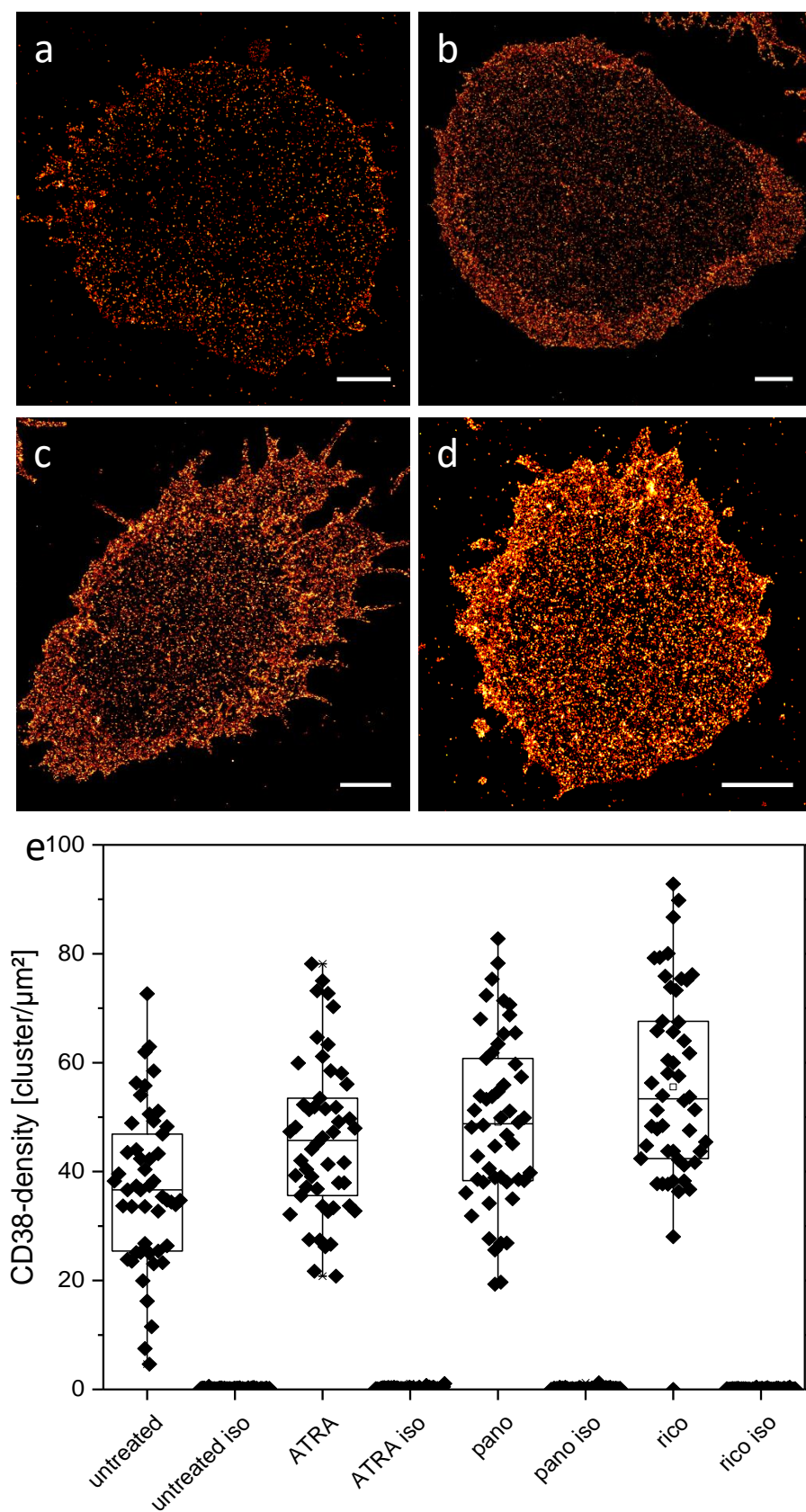
Figure 24 *d*STORM images of MM1.S cells live-cell stained for CD38 after drug treatment show a homogenous CD38-distribution. *d*STORM images of CD38 demonstrate an increase in CD38-expression after treatment with (b) ATRA, (c) panobinostat and (d) ricolinostat compared to (a) untreated cells. (e) Quantification reveals an increase in CD38-expression after treatment with ATRA, panobinostat and ricolinostat. Scale bar, 2 μm. With permission from García-Guerrero et al. 2020.

Figure 25 *d*STORM image of primary multiple myeloma patient cell live-cell stained for CD38 (a, b) without (e) or (f) with ricolinostat-treatment and the corresponding quantification. (a) Widefield- and *d*STORM image of a primary multiple myeloma cell stained for CD38 show an even CD38-distribution on the basal plasma membrane. These cells were earlier not treated with daratumumab. (b) Magnification of (a). The corresponding (c) widefield fluorescence- and (d) brightfield images. (e) *d*STORM image of a primary myeloma cell from a patient priorly treated with daratumumab shows a drastically decreased CD38-expression. (f) Upon treatment with ricolinostat, the *d*STORM image demonstrates a CD38-increase. (g) Quantification of ricolinostat treated and untreated primary multiple myeloma cells show a CD38-increase of 59% after ricolinostat treatment. Scale bar, 2 µm. With permission from García-Guerrero et al. 2020.

3.1.3.2 Quantification of CD38 in multiple myeloma cells

Similarly to the previous CD38-project, we investigated the potential of ATRA to upregulate the receptor BCMA. BCMA is expressed on B-lineage cells, importantly also on multiple myeloma cells, but not on healthy solid tissue. This makes BCMA a suitable target for CAR T-cell therapy which has already shown durable and complete remissions in hematologic malignancies like diffuse large B-cell lymphoma and acute lymphocytic leukemia (Kochenderfer et al. 2015, Pehlivan, Duncan and Lee 2018). Significant efforts are made to design CAR T-cells directed against various multiple myeloma associated antigens, among them CD19 and BCMA CAR T-cells from the Hudecek group (Nerreter et al. 2019, Prommersberger et al. 2018). Although BCMA CAR T-cells showed promising results in a phase I clinical trial with mainly partial and complete responses, still therapy limiting factors remain. Naturally, multiple myeloma cells expressing low BCMA-numbers might be missed by a BCMA-CAR T-cell therapy resulting in relapses after finishing the treatment. Thus, in this study we sought to increase the BCMA-density in the plasma membrane using again ATRA. It is hypothesized that the epigenetic changes induced by ATRA might not only effect, as previously published, the CD38-expression, but possibly also BCMA-levels (Balmer and Blomhoff 2002).

Therefore, we treated MM1.S cells with 50 µM and 100 µM ATRA and analyzed the BCMA surface densities using *d*STORM. In all cases BCMA was homogeneously distributed on the plasma membrane, albeit ATRA indeed induced changes in the BCMA-density (Fig. 26). Untreated MM1.S cells exhibited a mean BCMA-density of 6.1 ± 0.4 cluster/µm² (SE), while MM1.S cells treated with 50 µM ATRA had a BCMA-density of 7.0 ± 0.7 cluster/µm² (*p*-value = 0.29) and cells treated with 100 µM ATRA had a BCMA-density of 8.2 ± 0.6 cluster/µm² (*p*-value = 0.004, Fig. 26). Considering a mean cell surface of 652 µm² for untreated cells, 864 µm² for cells treated with 50 µM ATRA and 798 µm² for 100 µM ATRA treated cells the total antigen number per cell was calculated. This yielded in untreated MM1.S cells in mean 3983 ±1553 BCMA-molecules per cell (SD), in cells treated with 50 µM ATRA in 6018 ± 3028 BCMA-molecules per cell and in MM1.S treated with 100 µM ATRA in 6650 ± 2305 BCMA-molecules per cell. Moreover, no BCMA-negative cell could be detected during these experiments. This study demonstrates the potential of ATRA to enhance the BCMA-expression on the surface of multiple myeloma cells making treatments directed against BCMA more effective. To sum up, ATRA can induce a significantly enhanced expression of BCMA which was assessed by *d*STORM.
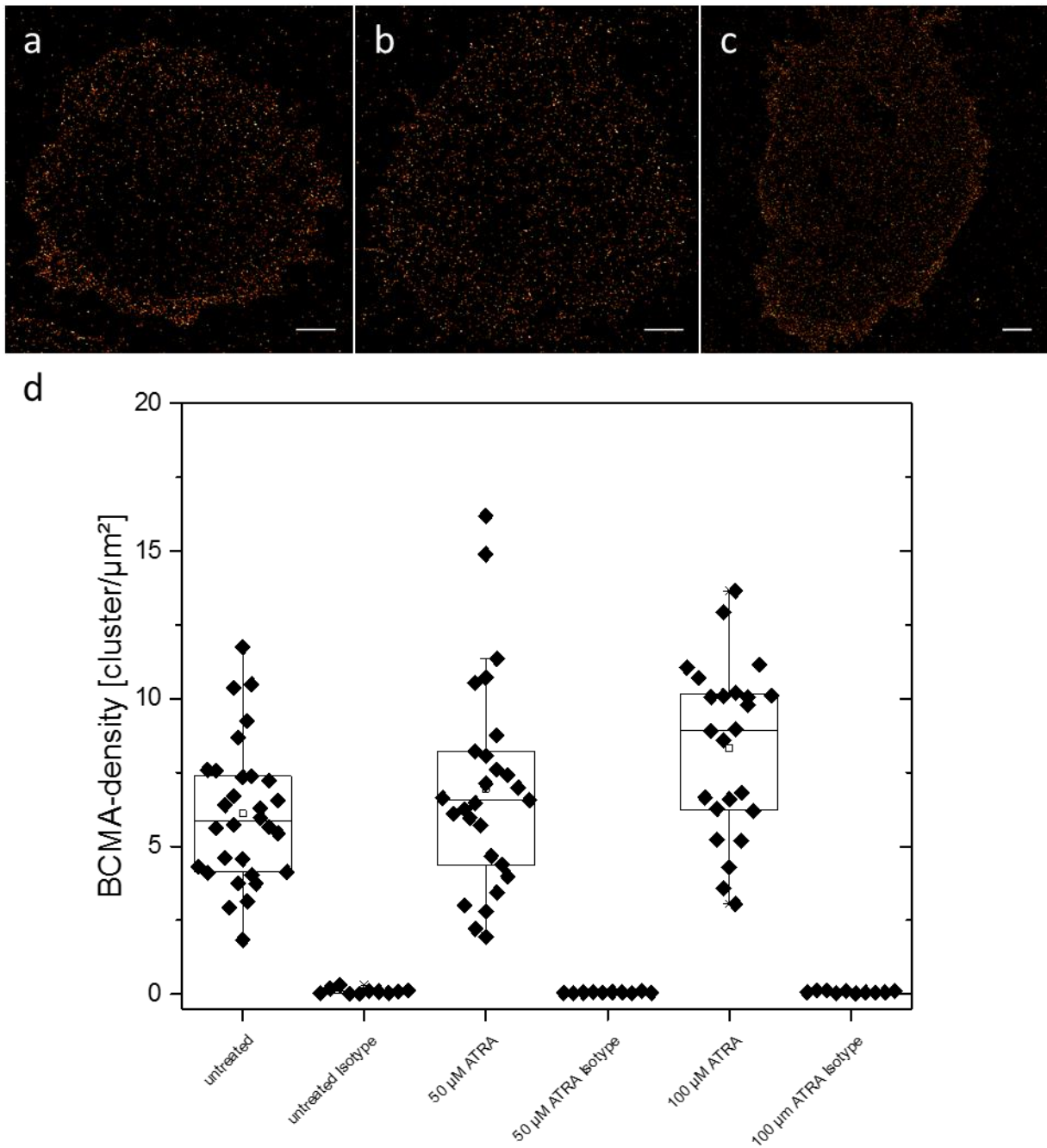
Figure 26 dSTORM images of MM1.S cells live-cell stained for BCMA (a) without or (b, c) with ATRA-treatment and (d) the corresponding quantification. (a-c) dSTORM images depict slight differences within BCMA-densities between the untreated control cells and the ATRA treated cells. (d) Quantification demonstrates a 15% increase after treatment (b) with 50 µM ATRA and a 34% increase in BCMA-surface levels after treatment (c) with 100 µM ATRA. Scale bars, 2 µm.

3.1.3.3 Quantification of CD20 in myeloma cells and the sensitivity of *d*STORM

In earlier experiments by Dr. Sebastian Letschert, Dr. Thomas Nerreter and Dr. Michael Hudecek it could be shown that in many cases there is an ultra-low expression of CD19 in multiple myeloma patients. These few CD19 molecules (<100 CD19 molecules) could only be detected by the single molecule sensitive method *d*STORM and not by flow cytometry with an estimated sensitivity of ~1350 CD19-molecules (Nerreter et al. 2019). They could also demonstrate that already few, only by *d*STORM detectable CD19-molecules, were sufficient to trigger an immune response by anti-CD19 CAR T-cells. This raised the question if also other antigens might be expressed on cancer cells that cannot be detected with conventional methods used in the clinics.

We reasoned that the B-cell marker CD20 might also be expressed in low amounts on the surface of myeloma cells, as the expression of CD20 in multiple myeloma is still insufficiently investigated (Yavasoglu et al. 2015, Huang et al. 2016).

In flow cytometry analyzes of three multiple myeloma patient samples one was classified negative (M029), whereas within the other two patients 33% (M025) and 16.8% (M027) of the myeloma cells' population were positive for CD20 (Fig. 27 a). When using *d*STORM however, a considerably higher percentage of CD20-positive myeloma cells was measured compared to flow cytometry (76.7% in M025 and 64.7% in M027). To achieve these results from the measured CD20-densities, a probability density function (PDF) was generated and receptor densities were fitted using either a one or two component log normal fit to separate the CD20-density distributions into CD20-positive and CD20-negative subpopulation. Hence, these fits also enabled the estimation of the CD20-positive cell population, although both fractions overlapped. To identify multiple myeloma cells the primary cells were additionally stained for CD38 (Alexa Fluor 488) and CD138 (Alexa Flour 555) (Fig. 27 b). Figure 27 d depicts selected *d*STORM images of primary multiple myeloma cells.
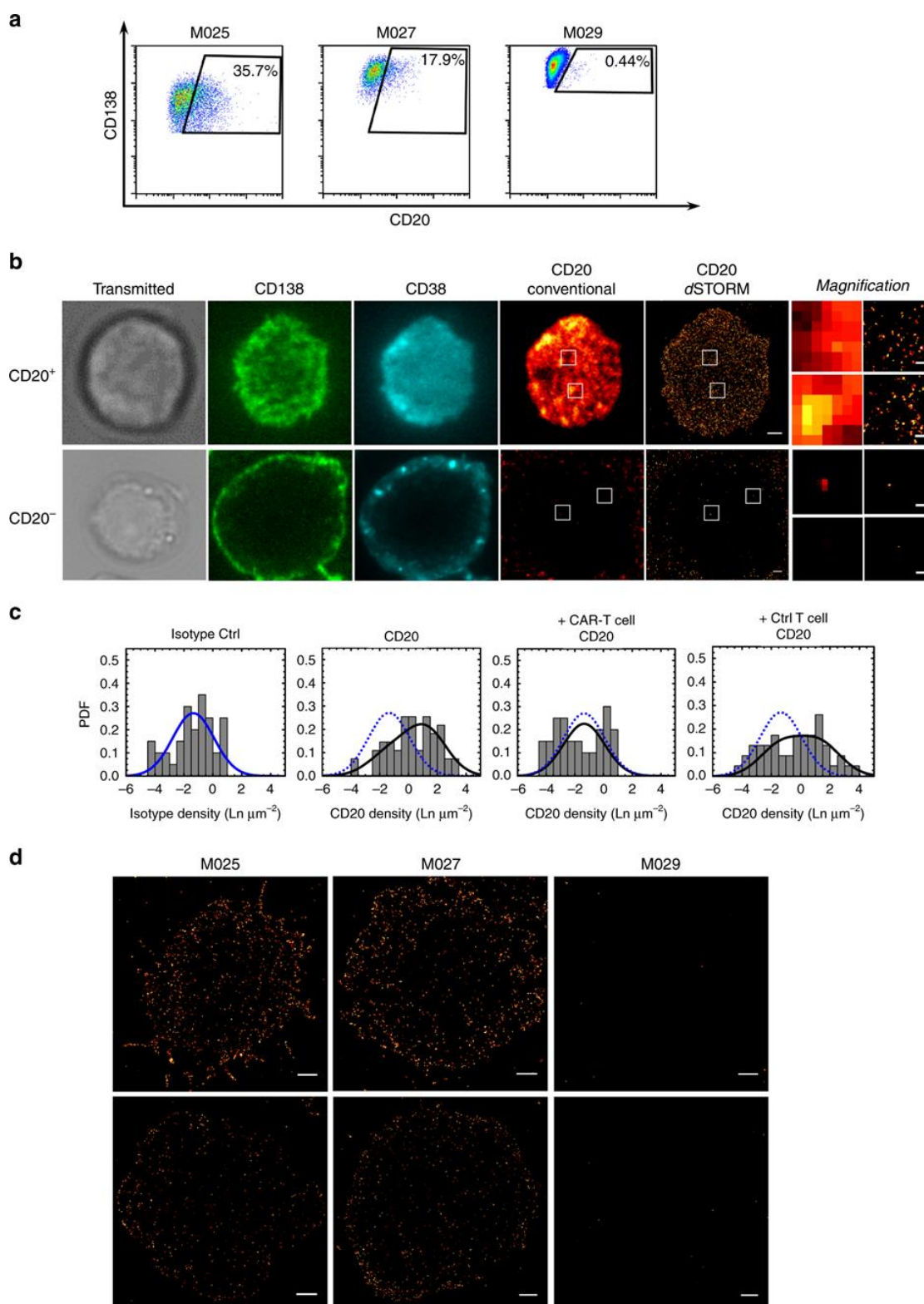
Figure 27 Detection of CD20-positive multiple myeloma cells and eradication by CD20 CAR T-cells. (a) Flow cytometry analysis of CD20-positive cells demonstrates CD20-positive fractions in patient M025 and M027 while patient M029 was negative for CD20. (b) Widefield and *d*STORM images of a CD20-positive and -negative myeloma cell. (c) Merged CD20-densities of the patients M025, M027 and M029 and the corresponding fits. The PDFs were fitted using a one or two component log-normal function to separate the measured densities into CD20-positive and CD20-negative subpopulations. Upon treatment with CD20 CAR T-cells all CD20-positive cells were eradicated. (d) Example *d*STORM images of the basal membrane from the patients M025, M027 and M029 stained for CD20. Scale bars, 1 µm and 0.2 µm (magnifications) (**b**), 3 µm (**d**). With permission from Nerreter et al. 2019.

The quantification of CD20 antigens resulted in mean 650 (55 – 7,724) CD20-molecules per cell in patient M025 and 1770 (149 – 21,045) CD20-molecules in patient M027 within 95% of all data. Figure 28 shows the corresponding fits of the measured cells. Incubation with CD20 CAR T-cells resulted in a complete eradication of all, by dSTORM judged, CD20-positive myeloma cells. This demonstrates that the single molecule sensitivity of dSTORM combined with the exquisite antigen sensitivity of CAR T-cells might be very beneficial in future diagnostics and treatments which might be applied to a variety of antigens.
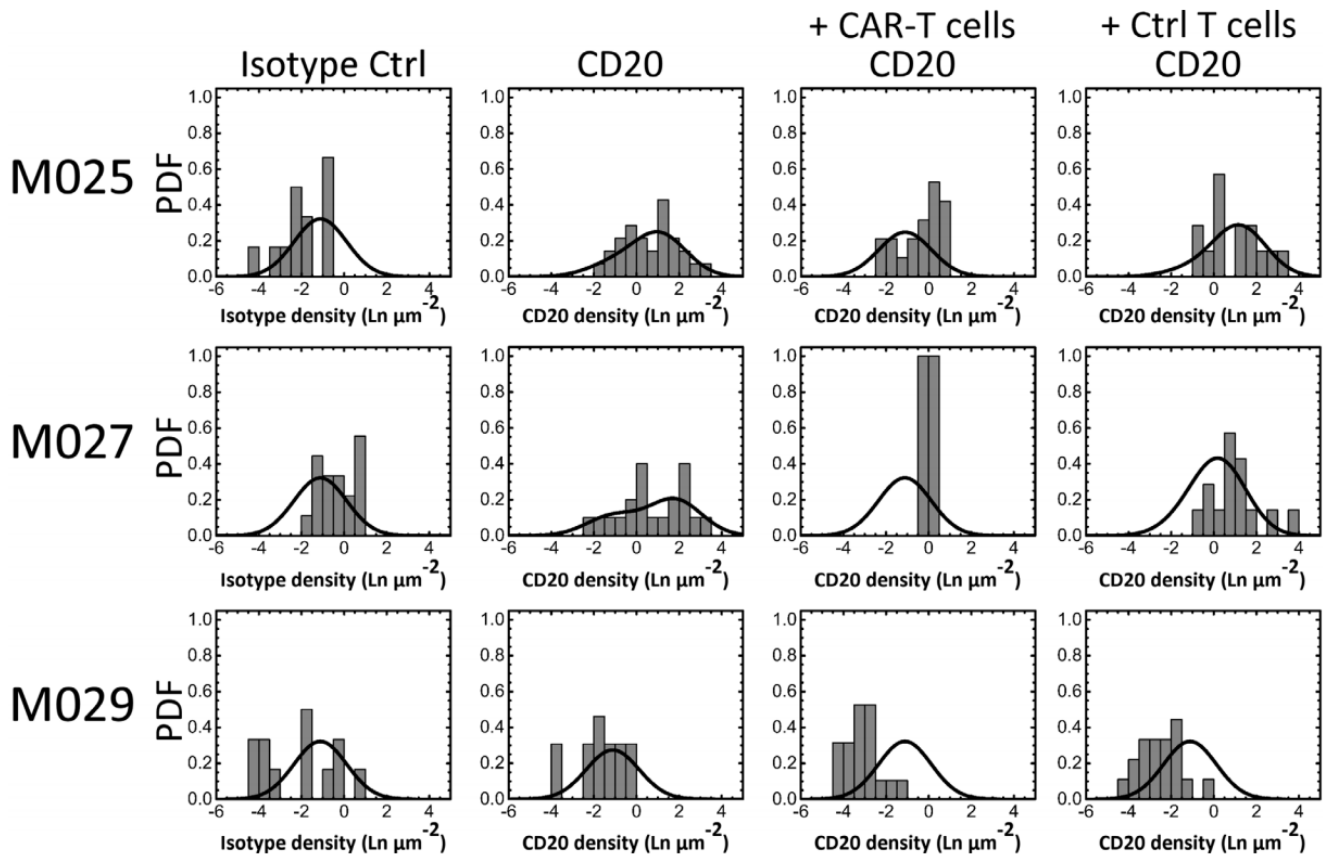
Figure 28 dSTORM quantification of CD20 on multiple myeloma cells and the eradication by CD20 CAR T-cells. Cells from myeloma patients were live-cell stained with an anti-CD20 antibody or the isotype (left panel). The quantification results were fitted using a one or two component log normal function and illustrated as probability density function. According to the fits, the CD20-distributions were divided into a CD20-positive and CD20-negative subpopulation. After treatment with CD20 CAR T-cells all CD20-positive cells were eradicated. With permission from Nerreter et al. 2019.

## 3.1.4 Three-dimensional receptor imaging by LLS and 10x ExM

Until now we solely imaged the basal membrane of T-cells with TIRF-microscopy. Therefore, issues concerning the molecular organization and interaction of T-cells and with the PDL-coated glass surface cannot be excluded. To address this, we performed LLS 3D-astigmatic *d*STORM experiments imaging the whole Jurkat T-cell stained for the clustered CD3 and the homogeneously distributed CD45. Felix Wäldchen built this LLS-setup which is suited for LLS 3D-astigmatic *d*STORM and all measurements were carried out collaboratively. The acquired images of both, CD3 and CD45 (Wäldchen et al. 2020), show that the receptor distribution is not altered due to interactions with the coverslip (Fig. 29). The LLS 3D-*d*STORM experiments demonstrate also that CD3 cluster formation is not induced by the contact to other cells or with the PDL-coated glass surface. The appearance of CD3 clusters can be explained by reports that cultured Jurkat T-cells can produce IL-2 which has a cell activating effect (Pawelec et al. 1982). Consequently, it is very unlikely that the naïve receptor distribution of the previously imaged receptors is altered at the basal plasma membrane.

As LLS 3D-astigmatic *d*STORM experiments are extremely time consuming due to long acquisition times and intensive data processing to render a final image, we decided to turn to tenfold expansion microscopy (Truckenbrodt et al. 2018, Truckenbrodt et al. 2019) for super-resolution imaging of whole T-cells. ExM is also time consuming in sample preparation, but image acquisition and processing can be performed much faster. However, beforehand we established the 10x ExM protocol in adherent U2OS cells. Upon fixation according to the cytoskeleton protocol (Michie et al. 2017), the sample was stained with antibodies directed against β-tubulin and Prx3 (Fig. 30 a) or α-tubulin and clathrin (Fig. 30 b). After gelation, digestion and expansion an isotropic and artifact-free approximately tenfold expansion could be demonstrated after imaging the expanded gels on a CLSM for tubulin, mitochondria and clathrin.
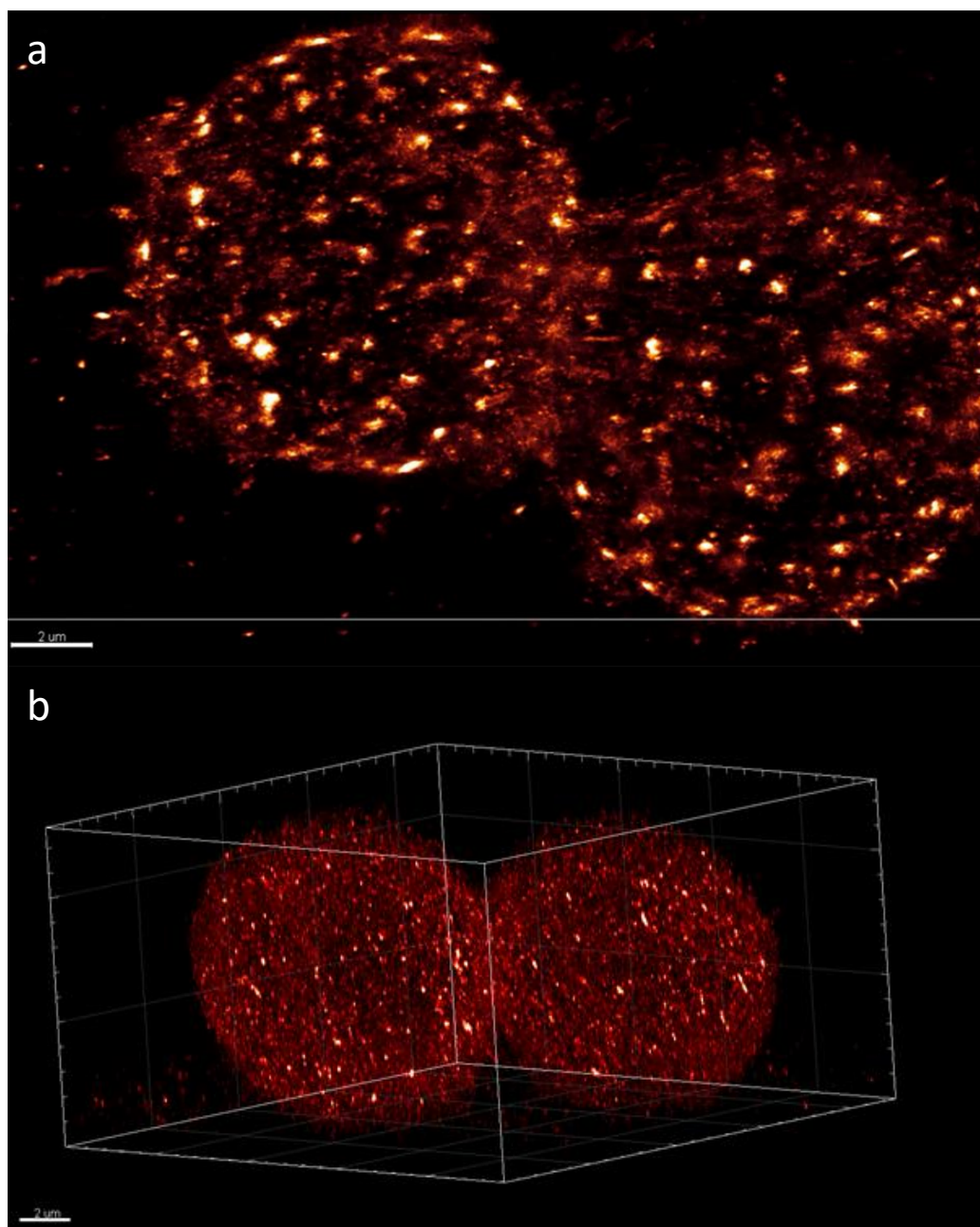
Figure 29 LLS 3D-astigmatic *d*STORM images of whole Jurkat T-cells stained for (a) CD3 and (b) CD45 demonstrate a homogeneous receptor distribution over the whole membrane. With permission from Wäldchen et al. 2020.
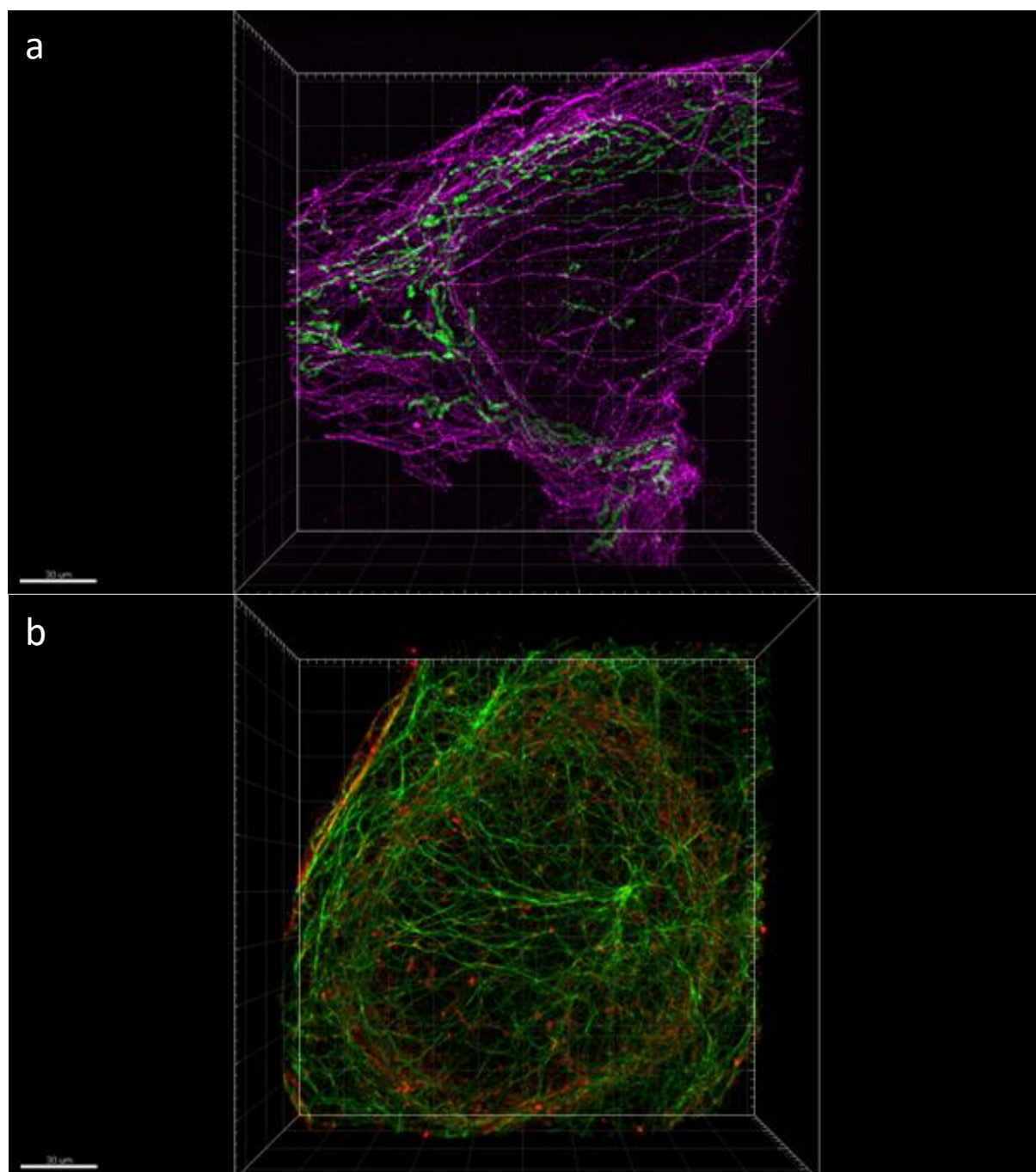
Figure 30 CLSM image of tenfold expanded U20S cells. Both samples were fixed according to the cytoskeleton protocol, immunostained with antibodies directed against (a) β-tubulin and Prx3 or (b) α-tubulin and clathrin, gelated, digested and expanded.

Next, we turned to suspension cells. Hereby, we started again with a conventional α-tubulin staining with Alexa Fluor 488 of Jurkat T-cells followed by gelation, digestion and expansion of the sample. 10x ExM of stained T-cells resulted in tenfold expanded T-cells with a size of >100 μm with an estimated resolution of ~25 - 30 nm at a confocal system (Truckenbrodt et al. 2018, Truckenbrodt et al. 2019) without any switching artifacts possible in *d*STORM or PALM (Fig. 31).
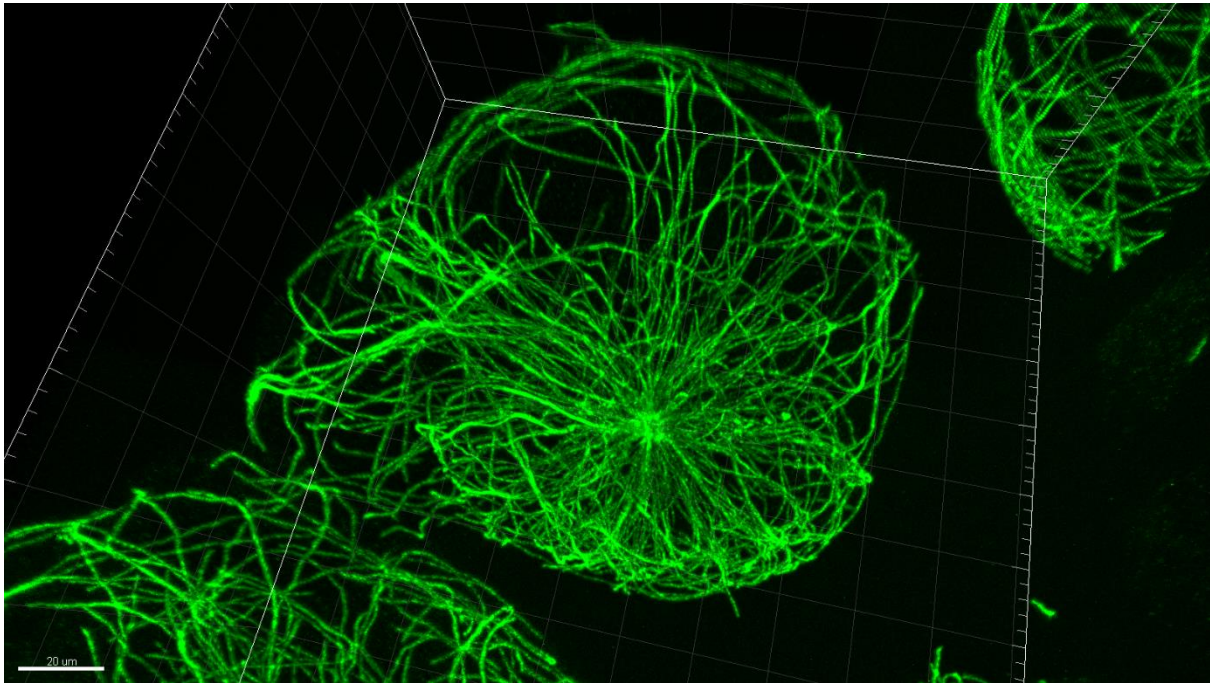
Figure 31 CLSM image of a tenfold expanded Jurkat T-cell immunostained for α-tubulin with Alexa Fluor 488 as secondary antibody. Jurkat T-cells were fixed according to the cytoskeleton protocol, stained, gelated and expanded. The successful tenfold expansion demonstrates the functionality of suspension cells to 10x ExM. This image resolves α-tubulin of a whole Jurkat T-cells with a resolution of ~25 - 30 nm at a CLSM.

To further extend the applicability of 10x ExM, we used Jurkat T-cells stained with antibodies directed against plasma membrane receptors which were directly conjugated with the stable expansion microscopy dye ATTO 643. We started with CD5 due to its clustered distribution on the surface of the plasma membrane which exhibited a strong signal. An efficient labeling of the structure of interest is especially in 10x ExM crucial because tenfold expansion in all dimensions results in a 1000-fold diluted signal density. Figure 32 depicts a tenfold expanded Jurkat T-cell stained for CD5 acquired at a CLSM. This demonstrates the principle compatibility of 10x ExM with whole cell receptor imaging. Contrary to the *d*STORM images of the basal membrane, nearly all CD5 molecules seem to be localized in big clusters. The CD5 quantification using IMARIS of the whole Jurkat T-cell resulted in mean 701 ± 175 CD5-clusters per cell (N=3, SD).
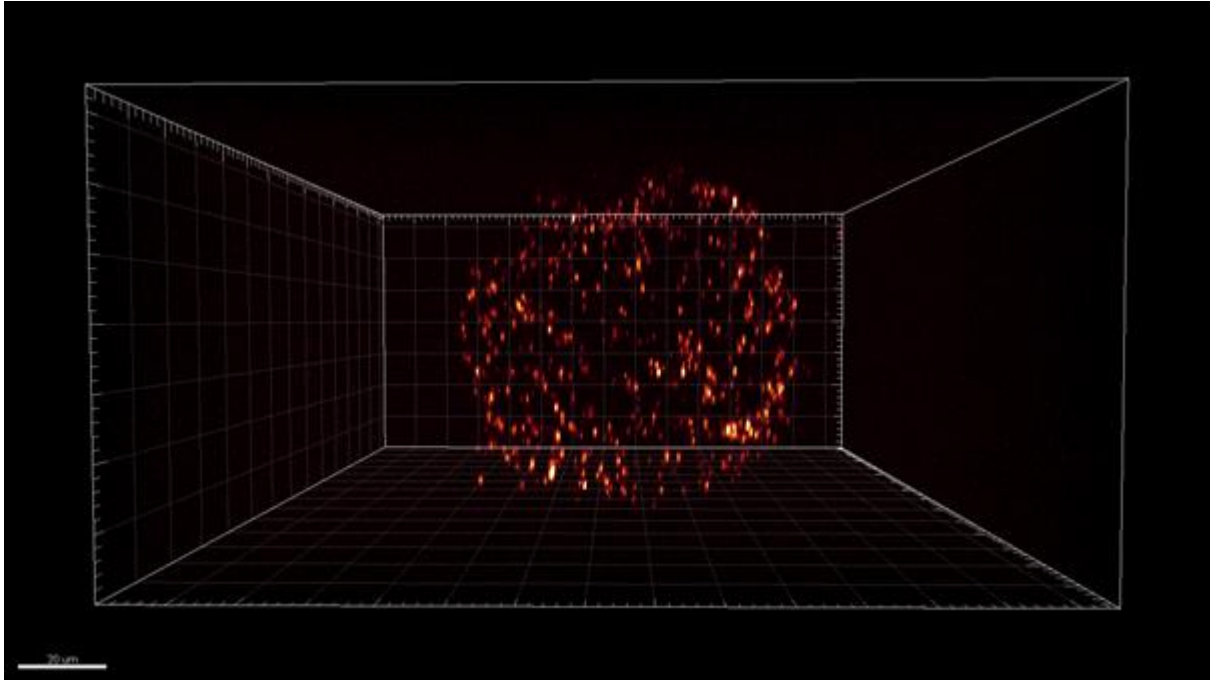
Figure 32 CLSM image of a tenfold expanded Jurkat T-cell live cell stained for CD5. The clustered receptor CD5 can be visualized at the plasma membrane of the whole Jurkat T-cells after tenfold expansion. Most receptors are distributed in clusters.

Next, we investigated if also receptors that are not organized in big clusters like CD5 could be detected at confocal systems using 10x ExM. To address this, we chose the receptor CD3 due to its heterogeneous clustering on the plasma membrane of Jurkat T-cells. After staining of CD3, fixation, gelation and expansion we could acquire images of CD3, albeit it appeared that mostly clustered receptors were detectable (Fig. 33 a). Comparison to LLS 3D-astigmatic *d*STORM images of CD3 with also many unclustered CD3 molecules supported the observation that many dye labeled antibodies cannot be detected by confocal microscopy in 10x ExM. Hence, we decided to amplify the fluorescence signal, as confocal systems are not single molecule sensitive which is necessary to detect single dye conjugated antibodies. Instead of a directly dye conjugated antibody we now applied a biotin conjugated antibody and amplified the fluorescence signal with streptavidin ATTO 643. This was followed by subsequent fixation, gelation and expansion. Now, it seemed that more molecules were detected than before without signal amplification (Fig. 33 b). Quantification using the IMARIS counter revealed without amplification 631 ± 480 CD3-clusters per cell (N=3, SD) while signal amplification using streptavidin ATTO 643 yielded in 2017 ± 130 CD3-clusters per cell (N=5). However, comparing the quantification results of expanded samples with data acquired from *d*STORM is difficult due to the differences in the acquisition and subsequent processing and quantification.
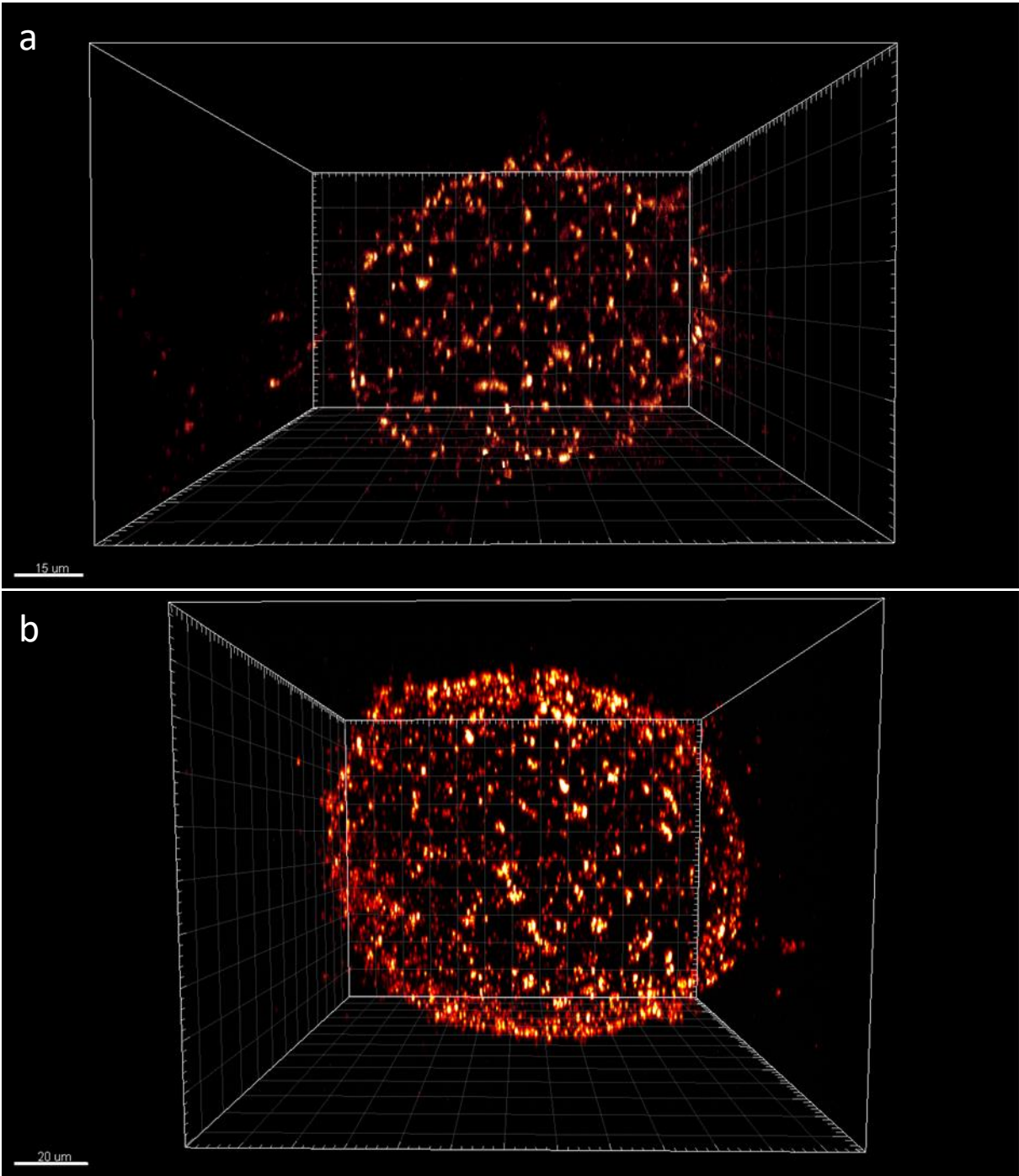
Figure 33 CLSM image of tenfold expanded Jurkat T-cells live cell stained for CD3 with (a) directly ATTO 643 conjugated anti-CD3 antibodies and (b) biotinylated anti-CD3 antibodies with signal amplification *via* streptavidin ATTO 643. Without signal amplification, mostly clustered CD3 molecules can be detected, while signal amplification results in an enhanced and denser CD3-distribution.

To further assess the sensitivity of 10x ExM at confocal systems, we investigated, if we could detect the heterodimer CD11a after signal amplification and tenfold expansion. Following labeling, gelation and expansion we could successfully visualize single antibodies bound to CD11a on the whole Jurkat T-cell membrane at a CLSM (Fig. 34). The counting of CD11a yielded in mean 1788 ± 58 clusters per cell (N=2, SD).
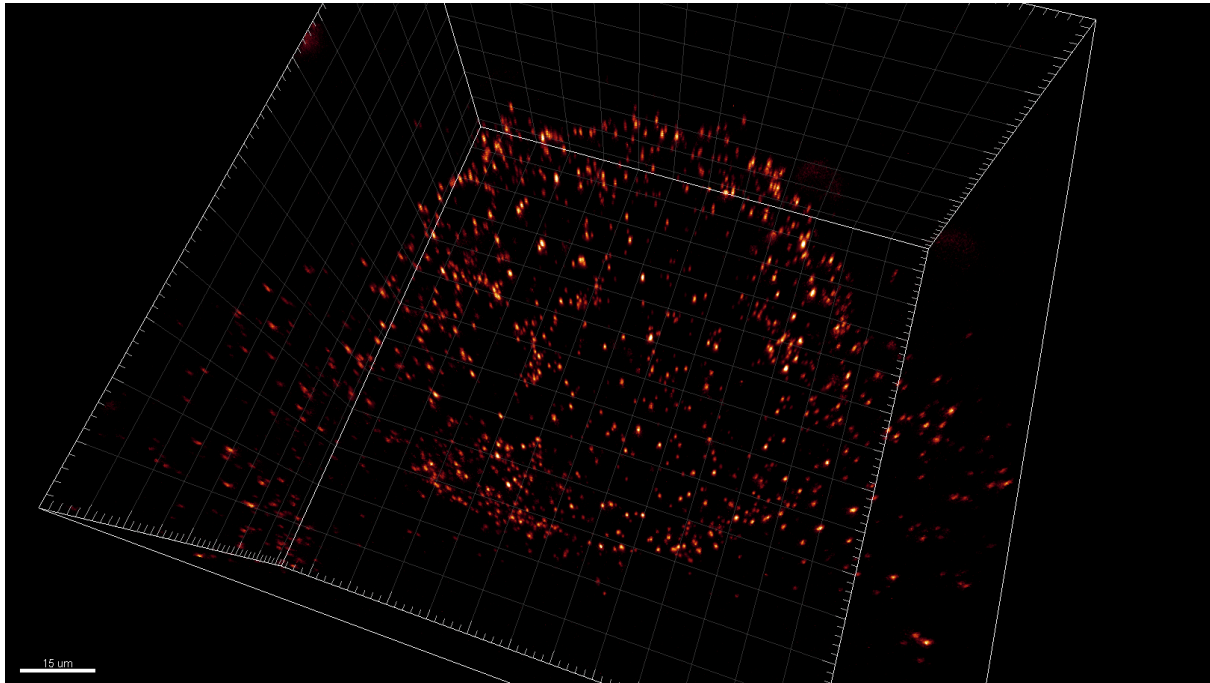
Figure 34 CLSM image of tenfold expanded Jurkat T-cell live cell stained for the heterodimer CD11a with signal amplification *via* streptavidin ATTO 643. This demonstrates that even single antibodies can be detected on confocal systems in 10x ExM after signal amplification using biotin-streptavidin.

A substantial obstacle when trying to image, especially in super-resolution microscopy, is the labeling efficiency. In classical immunofluorescence using antibodies always the question about epitope saturation and in particular epitope accessibility arises. Hence, we wondered, if 10x ExM-SIM with its superior resolution paired with the enourmos label size of an antibody (10 – 15 nm) (Tan et al. 2008) together with streptavidin signal amplification (5 nm) (Kuzuya et al. 2008) might enable the visualization of dimeric receptors. As target we chose CD2 which dimerices to ~15% according to the literature (Murray et al. 1995). First, using only a CLSM no dimers of CD2 could be detected (Fig. 35 a and b). Indeed, after combining our 10x ExM protocol with SIM and doubling the resolution to an estimated resolution of ~15 nm, we could detect dimer-like structures on the surface of Jurkat T-cells (Fig. 35 c). Comparison to similar *d*STORM images of CD2 on Jurkat T-cells acquired by Patrick Eiring demonstrated an estimation of 15 - 30% putative dimeric CD2 with a similar receptor distribution on the membrane surface (Fig. 35 d). The subsequent quantification of tenfold expanded Jurkat T-cells stained for CD2 resulted in 1799 ± 469 clusters per cell (N=6). In summary, this data demonstrates the potential of 10x ExM for whole cell receptor imaging.
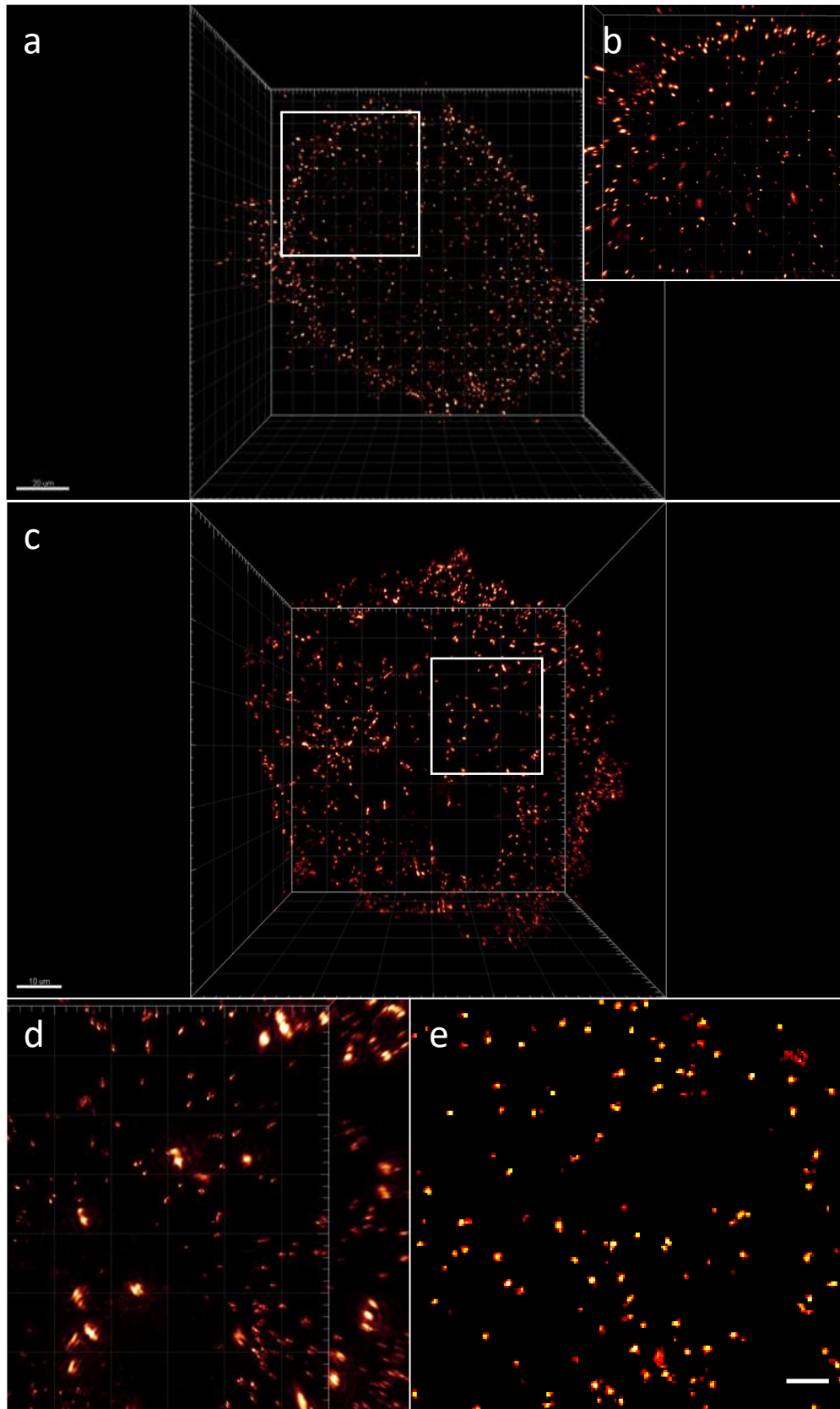
Figure 35 Super-resolution images of Jurkat T-cells stained for CD2. (a) 10x ExM CLSM image of a whole Jurkat T-cell stained for CD2 with signal amplification *via* streptavidin ATTO 643. (b) Magnified view of the white box within the main image. (c) 10x ExM-SIM image of a whole Jurkat T-cell stained for CD2 with signal amplification *via* streptavidin ATTO 643. (d) Magnified view of the white box within the main image displays putative CD2-dimers. (e) *d*STORM image of a basal membrane of Jurkat T-cells stained for CD2 with Alexa Fluor 647 demonstrates a comparable putative CD2 dimerization.

3.2 ExM of pathogens

After imaging receptors of whole T-cells with a superior resolution we now sought to further extend the applicability of expansion microscopy. First, we expanded the bacterial pathogen *Chlamydia trachomatis*, followed by the expansion of not only proteins, but also lipids in *Chlamydia trachomatis*, *Simkania negevensis* and *Neisseria gonorrhoeae*. After that, we applied ExM to even more challenging targets, the three fungi *Ustilago maydis, Fusarium oxysporum* and *Aspergillus fumigatus*, with their extremely solid and stable cell wall as obstacle.

All projects involving bacteria were performed entirely collaboratively with Tobias C. Kunz and the projects involving fungal pathogens with Sabine Panzer and Nora Trinks.

3.2.1 ExM of *Chlamydia trachomatis*

As proof of concept study if expansion microscopy could be used for bacteria, we applied fourfold ExM to the obligate intracellular gram-negative pathogen *C. trachomatis* (Kunz et al. 2019). ExM was hereby carried out completely according to Chozinski et al. (Chozinski et al. 2016), there was no need to apply further lysozyme digestions to *C. trachomatis* infected HeLa 229 cells, as reported for other bacteria (Lim et al. 2019). The first successfully expanded chlamydial proteins were the heat-shock protein HSP60, as chlamydial marker, and the protease CPAF which is secreted *via* a T2SS (Patton et al. 2016). In both, confocal and ExM images, after 22 hours post infection (hpi) HSP60 localizes within the single *Chlamydia*, while CPAF is already secreted. 30 h after infection CPAF is even stronger secreted and is sometimes even resident within single *Chlamydia* (Fig. 36). In both cases, ExM improves the resolution by a factor of four compared to the confocal images to enable the visualization of single, different sized *Chlamydia*. In the cases of 22 hpi, however, CPAF is only weakly visible due to signal dilution of the ExM experiment. By contrast, the T2SS-deficient mutant could not secret CPAF and therefore CPAF accumulated within *C. trachomatis*. Interestingly, also here single *Chlamydia* could be visualized using ExM.
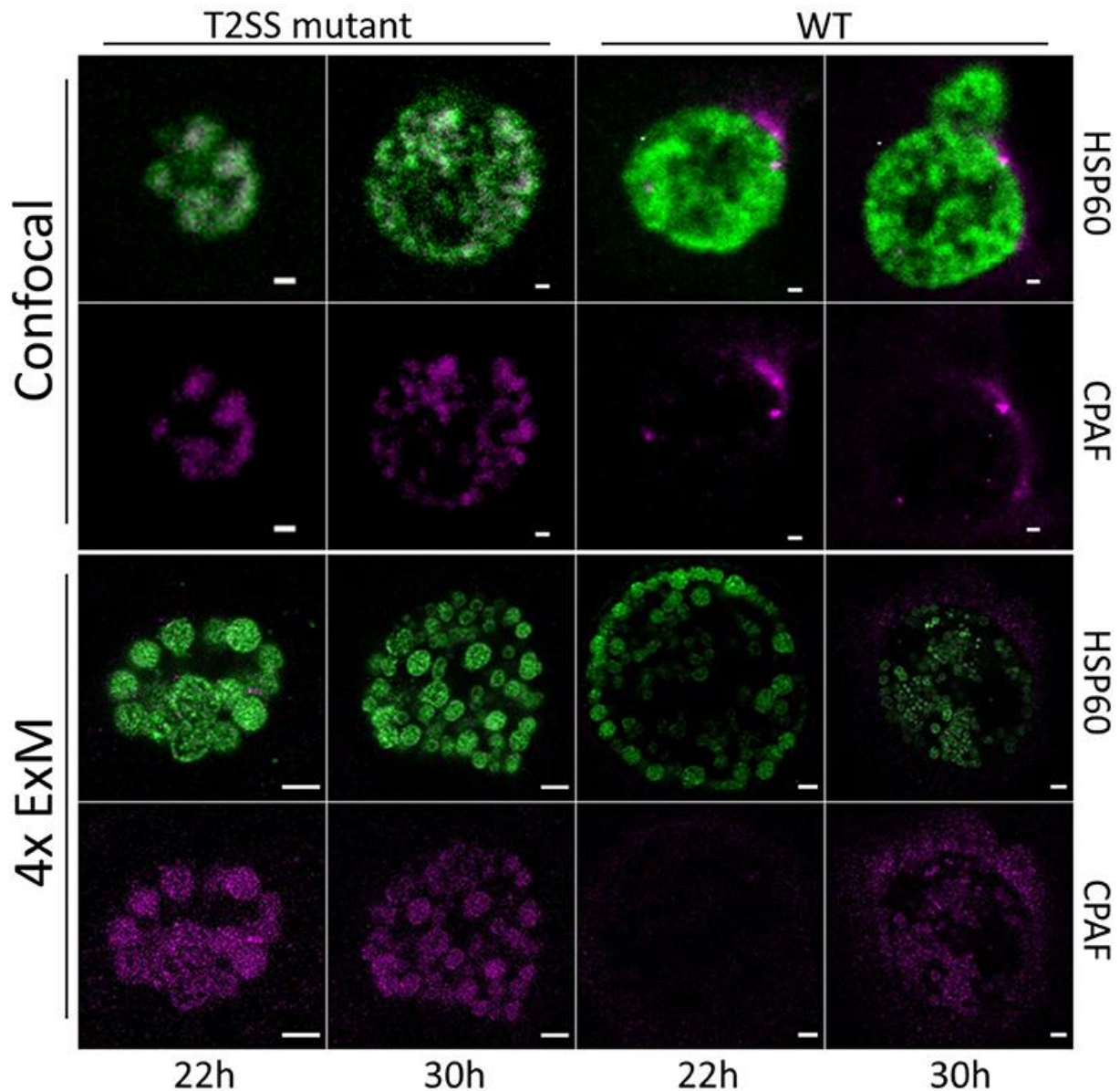
Figure 36 CLSM images of with *C. trachomatis* infected and expanded HeLa 229 cells. Cells were infected for 22 or 30 h with the wildtype or the T2SS mutant of *C. trachomatis*. The sample was immunostained for HSP60 (green, Alexa 488) and CPAF (magenta, ATTO 647N). In wildtype *C. trachomatis* CPAF localizes on individual chlamydial particles and is secreted using a T2SS. CPAF-expression increases from 22 hpi to 30 hpi. The *C. trachomatis* T2SS-mutant cannot secret CPAF and CPAF accumulates within individual chlamydial particles. Scale bars, 1 µm (confocal) and 5 µm (4x ExM). With permission from Kunz et al. 2019.

As next step we expanded additionally to HSP60 the chlamydial deubiquitinase 1 (Cdu1). Again, when expanding HSP60, single *Chlamydia* became visible and Cdu1, present at the inclusion membrane, could be visualized even better around the membrane. Moreover, beforehand barely detectable, distinct spots and an irregular distribution of Cdu1 became apparent at the inclusion after expanding *C. trachomatis* infected cells. Within the mutant *C. trachomatis* Cdu1:: Tn bla, Cdu1 was by contrast not localized at the inclusion membrane (Fig. 37).
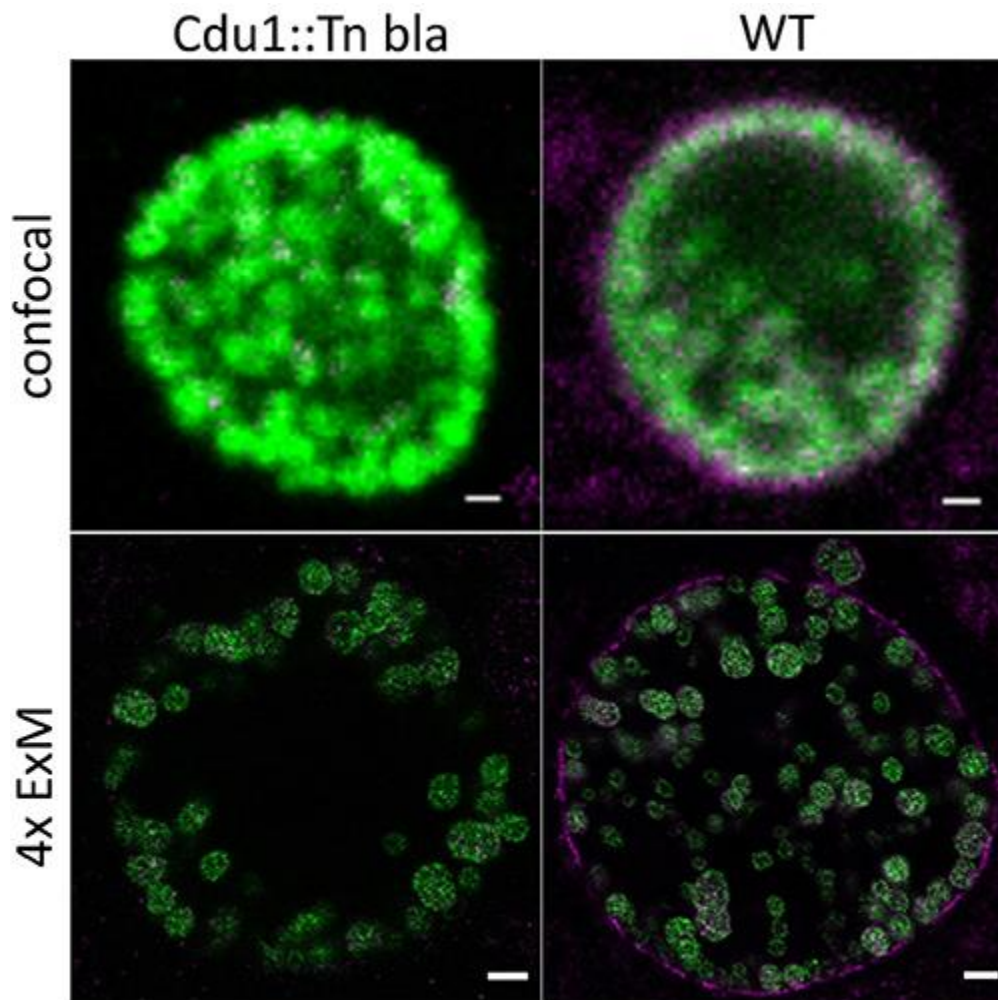
Figure 37 Cdu1 localizes at the inclusion membrane of both unexpanded and expanded samples. HeLa 229 cells were infected for 24 h with *C. trachomatis* or *C. trachomatis* Cdu1:: Tn bla. Cells were immunostained for chlamydial HSP60 (green, Alexa 488) and Cdu1 (magenta, ATTO 647N). In wildtype *C. trachomatis* Cdu1 localizes in the inclusion membrane, whereas it does not in the mutant Cdu1::Tn bla. Scale bars, 1 µm (confocal) and 5 µm (4x ExM). With permission from Kunz et al. 2019.

In the two previous experiments we could show not only the visualization of single *Chlamydia*, but also noticed different sizes among expanded *Chlamydia*. Hence, we hypothesized that we might be able to distinguish EBs (~300 nm) and RBs (~1 µm) (Rank 2009) by ExM. Fortunately, we could make use of the recently published *Chlamydia* strain *Ct* mCh(GroL2) GFP(OmcAL2) which expressed mCherry under the control of the RB-associated constitutive *groESL* operon promoter and GFP under the control of the EB-associated *omc* promoter. The within this study newly engineered *Chlamydia* strain allowed us to distinguish between EBs and RBs by the expression of GFP and mCherry and to monitor the RB conversion to EBs (Cortina et al. 2019). To test our hypothesis we infected HeLa 229 with this new *Chlamydia* strand and expanded the sample according to our established protocol. In confocal images prior to expansion the GFP and mCherry expressing *Chlamydia* were visible although only minor size differences were noticeable. Following expansion it became evident that solely the small *Chlamydia* expressed GFP and only the bigger ones expressed mCherry. This confirms our theory that the

small expanded *Chlamydia* represent EBs and the big expanded *Chlamydia* RBs. This data demonstrates that ExM is an ideal tool to study the infection by *C. trachomatis* and to distinguish the two different chlamydial developmental forms during infection (Fig. 38).
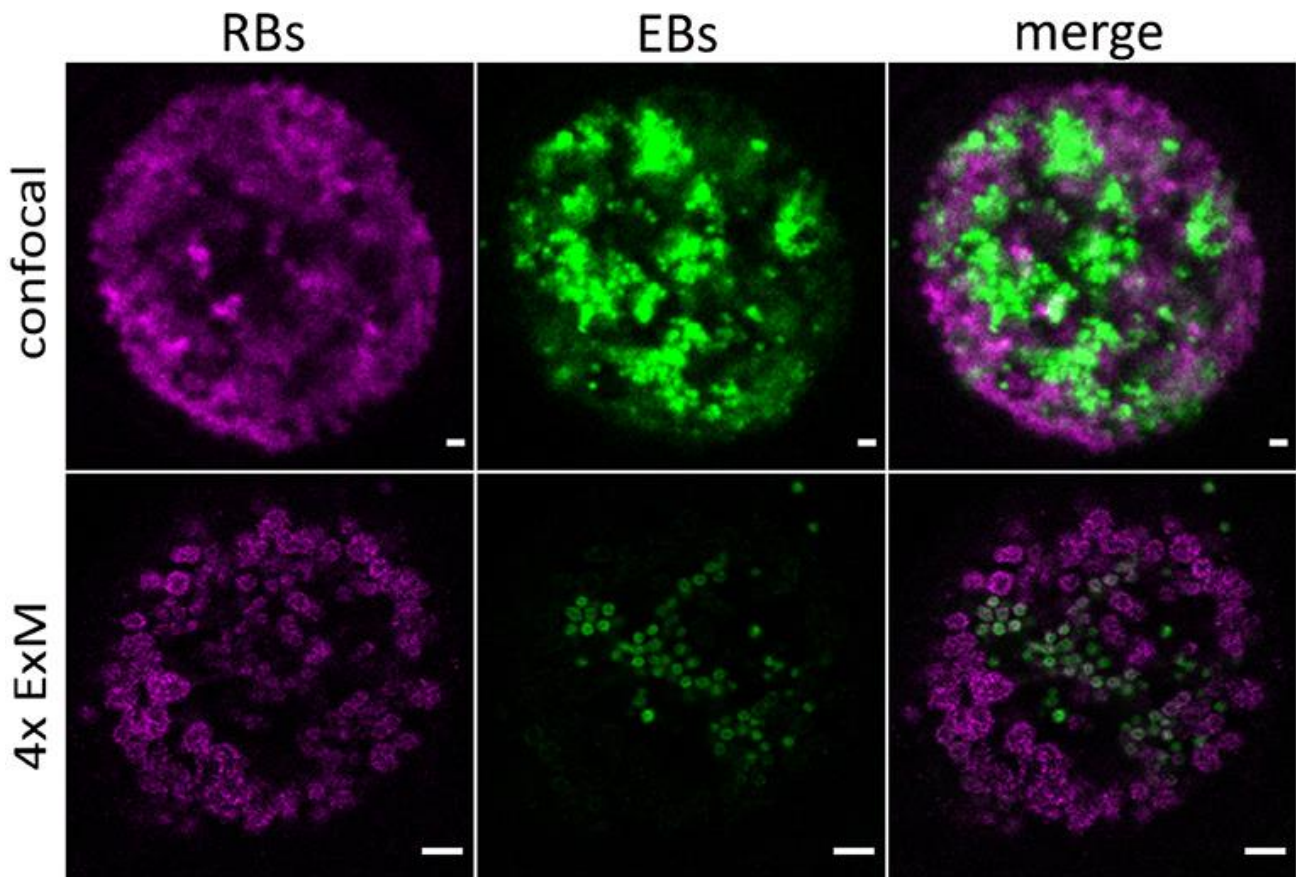
Figure 38 ExM enables the detection of single chlamydial EBs and RBs. CLSM images of unexpanded and expanded HeLa 229 cells infected with *C. trachomatis* mCh(GroeL2) GFP(OmcAL2) for 30 h. Additionally, an immunostaining for GFP (green, Alexa 488) and mCherry (magenta, ATTO 647N) was performed. The expanded images demonstrate a substantial size difference between EBs and RBs. Scale bars, 1 µm (confocal) and 5 µm (4x ExM). With permission from Kunz et al. 2019.

3.2.2 Sphingolipid ExM of intracellular pathogens

In the following project we not only applied fourfold expansion, but also tenfold expansion microscopy to *Chlamydia trachomatis* and *Simkania negevensis* infected HeLa 229 cells. Hereby, we also extended the applicability of ExM to lipids, in this case sphingolipids, enabled by the modification with a primary amine.

To first validate the idea of expansion experiments with lipids bearing solely one primary amine, Tobias C. Kunz and Franziska Solger tested ExM with ω-sphingosine fed to with *Neisseria gonorrhoeae* infected Chang cells, since the protocol of infection and feeding with ω-sphingosine was already well established. ω-sphingosine was an ideal model to test ExM with lipids, as it possesses exactly one primary amine. SIM images before expansion demonstrate the sphingosine incorporation of *N. gonorrhoeae*, although after expansion according to our established ExM protocol (Kunz et al. 2019) the single *Neisseria* were far better visible (Fig. 39). Not only the expansion of the anti-*Neisseria gonorrhoeae* antibody was isotropic, but also the expansion of sphingosine could be demonstrated successfully. It should be noted that the successful and isotropic expansion of *N. gonorrhoeae* required the additional treatment with lysozyme to degrade the bacterial membrane according to Lim et al. (Lim et al. 2019).
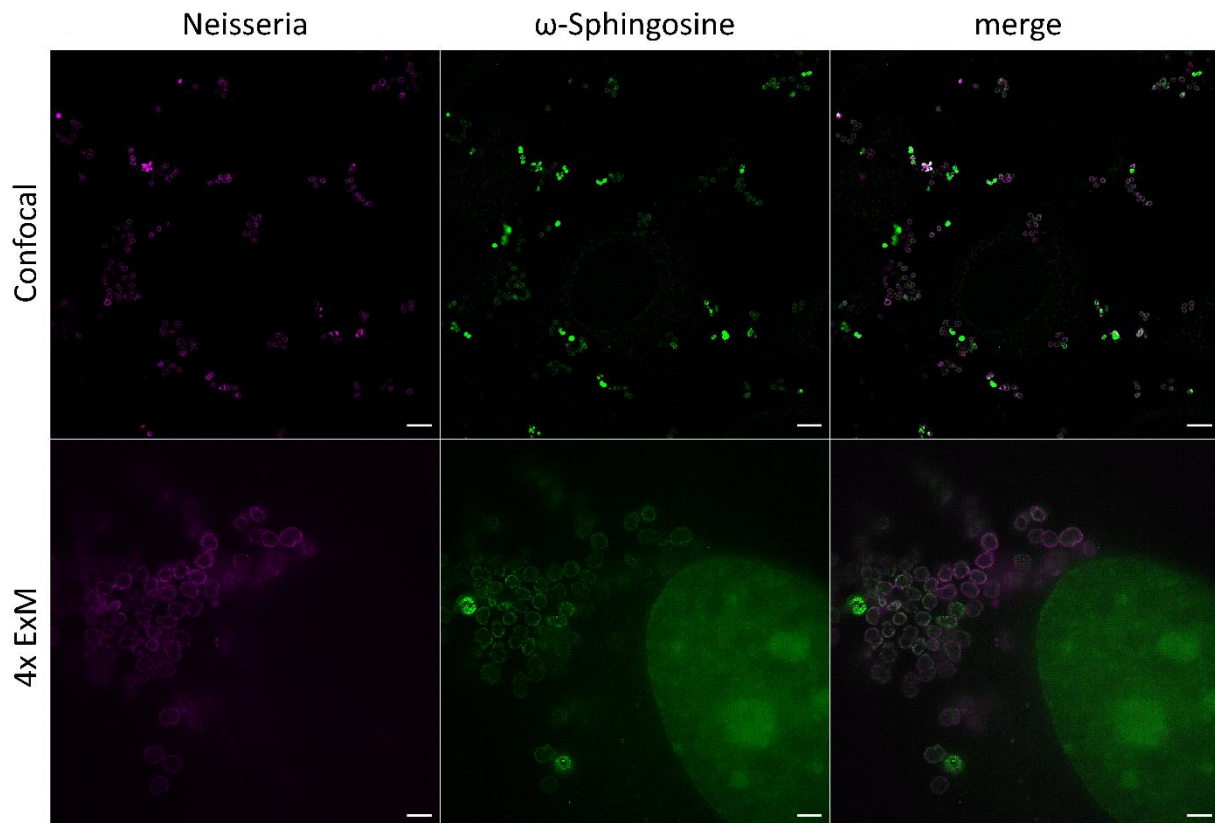
Figure 39 Unexpanded SIM- (upper row) and 4x ExM-SIM images (lower row) of with *Neisseria gonorrhoeae* for 4 h infected Chang cells. Cells were fed with ω-sphingosine, fixed and after permeabilization stained with DIBO-Alexa Flour 488 (green) and an anti-*Neisseria gonorrhoeae* antibody (magenta). 4x ExM-SIM images demonstrate the incorporation of ω-sphingosine into the neisserial membrane. Scale bars, 5 µm (unexpanded confocal), 4 µm (4x Ex). With permission from Götz et al. 2020a.

Because of this successful proof of concept experiment, Julian Fink and Prof. Dr. Jürgen Seibel synthesized an α-NH$_2$-ω-N$_3$-C$_6$-ceramide (Fig. 40 a) that should be theoretically incorporable into a hydrogel due to the primary amine and be click-labeled by a SPAAC-reaction using DBCO-dyes. To assess the ceramide uptake, we fed HeLa 229 cells 1 h with 10 µM of the newly synthesized ceramide, fixed the sample with formaldehyde and glutaraldehyde and stained after permeabilization for 30 min at 37°C with DBCO Alexa Fluor 488. As control for the uptake served the already established ω-N$_3$-C$_6$-ceramide without an additional primary amine. Both ceramides showed a comparable localization within the cell, with most ceramides resident within intracellular organelles. As the addition of a primary amine should also enable the fixation of the fed ceramides, we additionally treated the fixed and stained samples with various concentrations of the detergent Triton X-100. The samples with the α-NH$_2$-ω-N$_3$-C$_6$-ceramide showed only a slight signal decrease upon Triton X-100 exposure and remained constant with increasing detergent concentrations. By contrast, the ω-N$_3$-C$_6$-ceramide without the amine modification vanished rapidly after treatment with Triton X-100 (Fig. 40 c). FRAP-experiments by Jan Schlegel further approved this with a decreased mobile fraction of the amine-modified ceramide (22.2%, Fig. 40 b) compared to the conventional one (48.1%). These results indicate an efficient fixation of the amino-modified ceramides by the crosslinker glutar-aldehyde within cellular membranes.

As glutaraldehyde is known to link proteins into hydrogels (Chozinski et al. 2016, Weston and Avrameas 1971), we concluded that our α-NH$_2$-ω-N$_3$-C$_6$-ceramide could be also compatible for ExM. Consequently, we applied 4x and 10x ExM to HeLa 229 cells treated, as described in the upper section, to test the applicability of sphingolipid expansion. For both expansion factors an isotropic expansion could clearly be confirmed and the ceramides localized strongly within cellular organelles (Fig. 41).
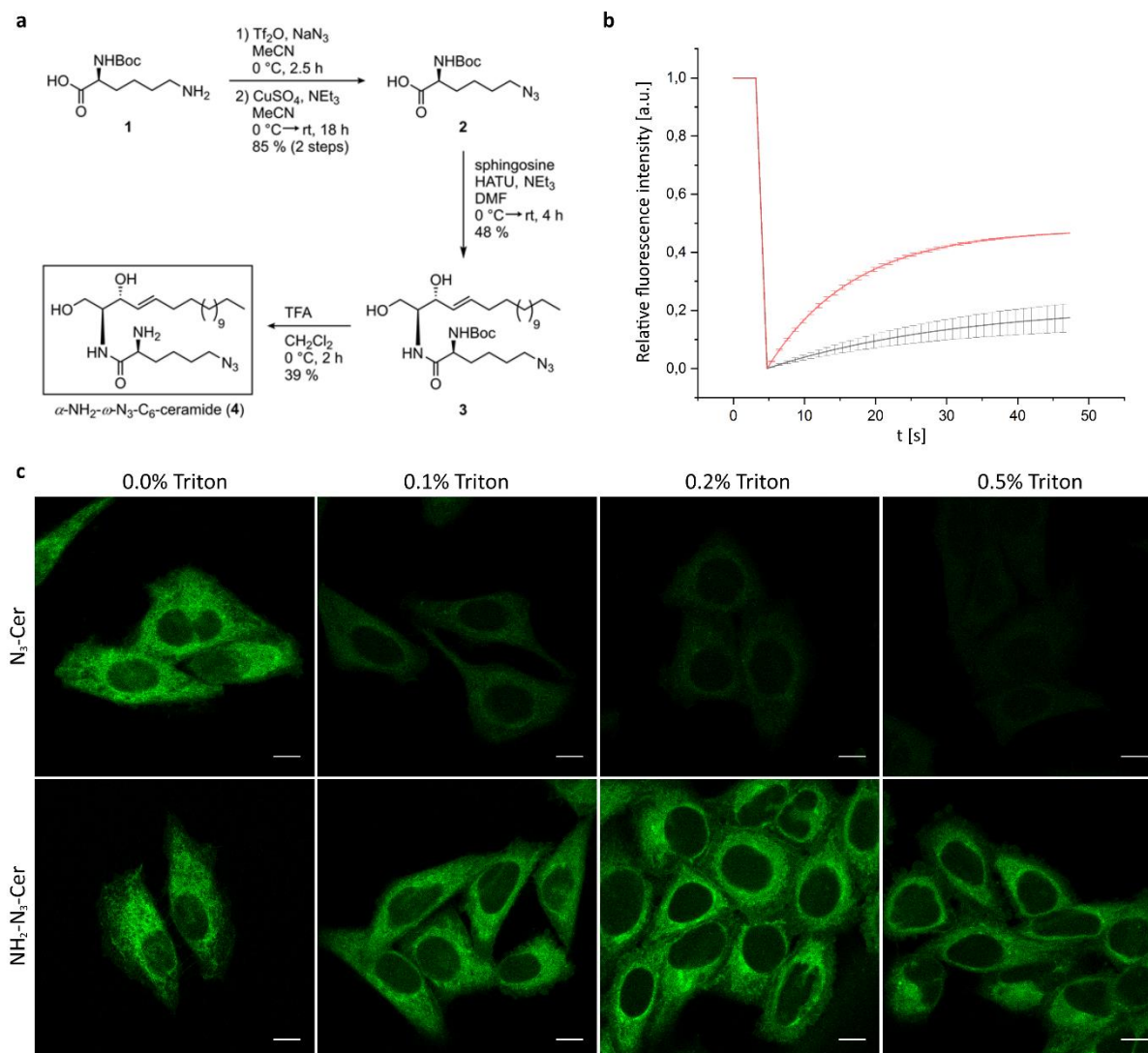
Figure 40 Bifunctional amino- and azido-modified ceramides enable the fixation and fluorescence labeling of lipids. (a) Synthesis of our α-NH$_2$-ω-N$_3$-C$_6$-ceramide. The functionalized ceramides α-NH$_2$-ω-N$_3$-C$_6$-ceramide or ω-N$_3$-C$_6$-ceramide (10 μM) were fed to HeLa 229 cells for 1 h. After incorporation into the membrane the cells were fixed and after permeabilization stained with DBCO Alexa Fluor 488. (b) To investigate the mobility, FRAP experiments with the two incorporated ceramide analogues were performed after fixation with glutaraldehyde and permeabilisation. During FRAP-measurements, after three imaging frames, a circular region with a radius of 0.9 μm was bleached and fluorescence recovery was recorded over time. The α-NH$_2$-ω-N$_3$-C$_6$-ceramide showed a substantially lower mobility rate with a mean mobile fraction of 22.2% compared to the ceramide without the amino group with a mean mobile fraction of 48.1%. (c) CLSM images of fixed and labeled HeLa 229 cells incubated in increasing concentrations of the detergent Triton-X100. The ω-N$_3$-C$_6$-ceramide is efficiently washed out after exposure to Triton-X100, whereas the α-NH$_2$-ω-N$_3$-C$_6$-ceramide signal remains conserved. Scale bars, 10 μm. With permission from Götz et al. 2020a.
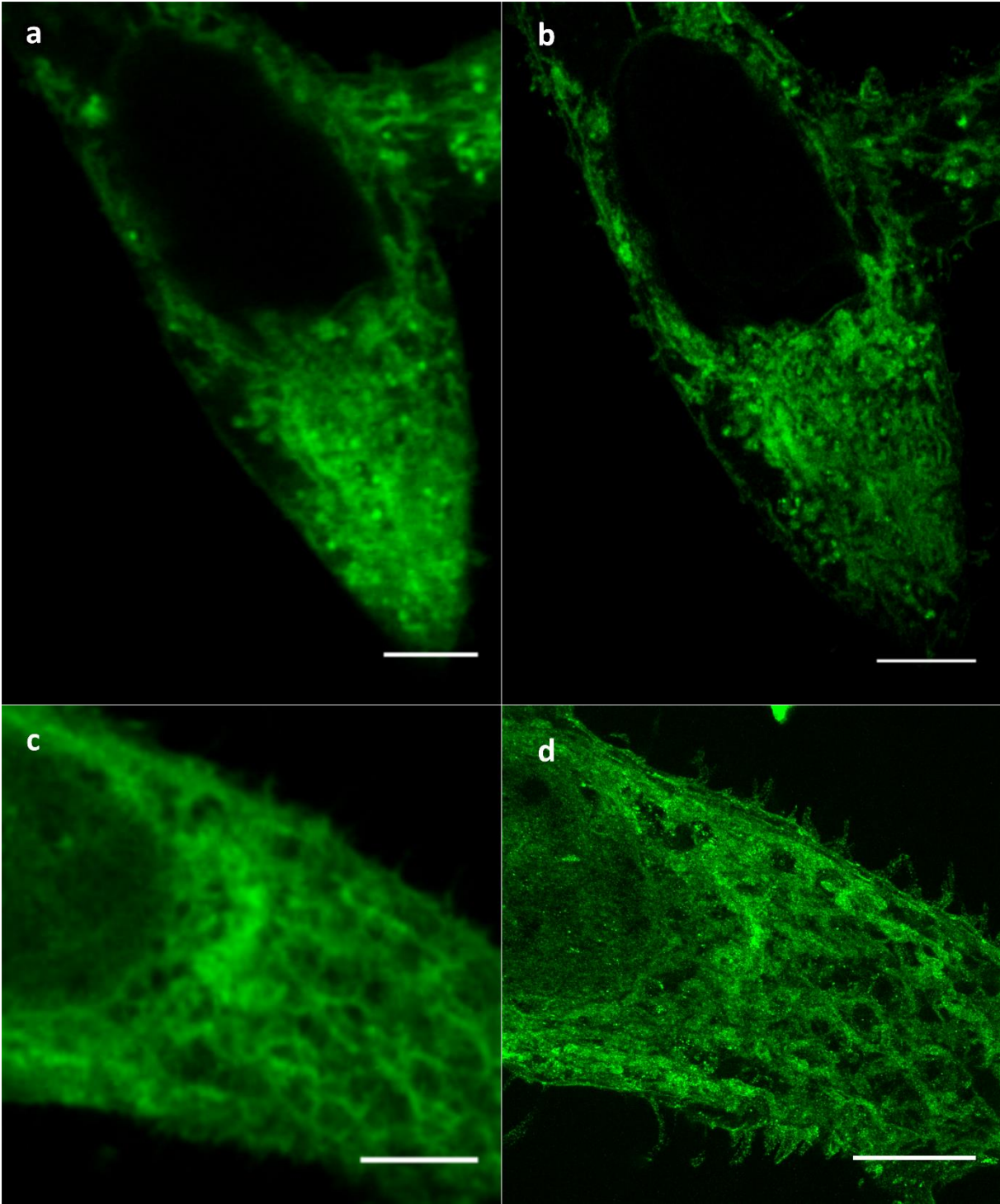
Figure 41 Unexpanded, 4x ExM and 10x ExM images of Hela 229 cells incubated in 10 μM α-NH$_2$-ω-N$_3$-C$_6$-cera-mide which were fixed, permeabilized and stained with DBCO Alexa Fluor 488 (green). (a, c) Pre-expansion and (b, d) post-expansion CLSM images of HeLa 229 cells after isotropic (b) fourfold and (d) tenfold expansion. With permission from Götz et al. 2020a.

In the case of fourfold expansion, the ceramides clearly localized within organelles like the ER and mitochondria which could be confirmed by the colocalization of ceramides with peroxiredoxin 3 (Prx3), a mitochondrial matrix protein (Fig. 42 a). Moreover, the ceramide signal was very specific and localized not only within the organelles, but also in the plasma and nuclear membrane. In case of tenfold ExM we also performed a plasma membrane staining using mCling ATTO 643 (Revelo et al. 2014) as mCling should also be compatible with ExM due to its lysine residues. Both, the bifunctional α-NH$_2$-ω-N$_3$-C$_6$-ceramide and mCling, could be successfully expanded tenfold with mCling staining mainly the plasma membrane and the ceramide staining the plasma- and nuclear membrane as well as again the organelle membranes (Fig. 42 b). Here, possibly even the double nuclear membrane could be resolved. These results clearly demonstrate the compatibility of the α-NH$_2$-ω-N$_3$-C$_6$-ceramide with the super-resolution method ExM to visualize cellular membranes at two different expansion factors.
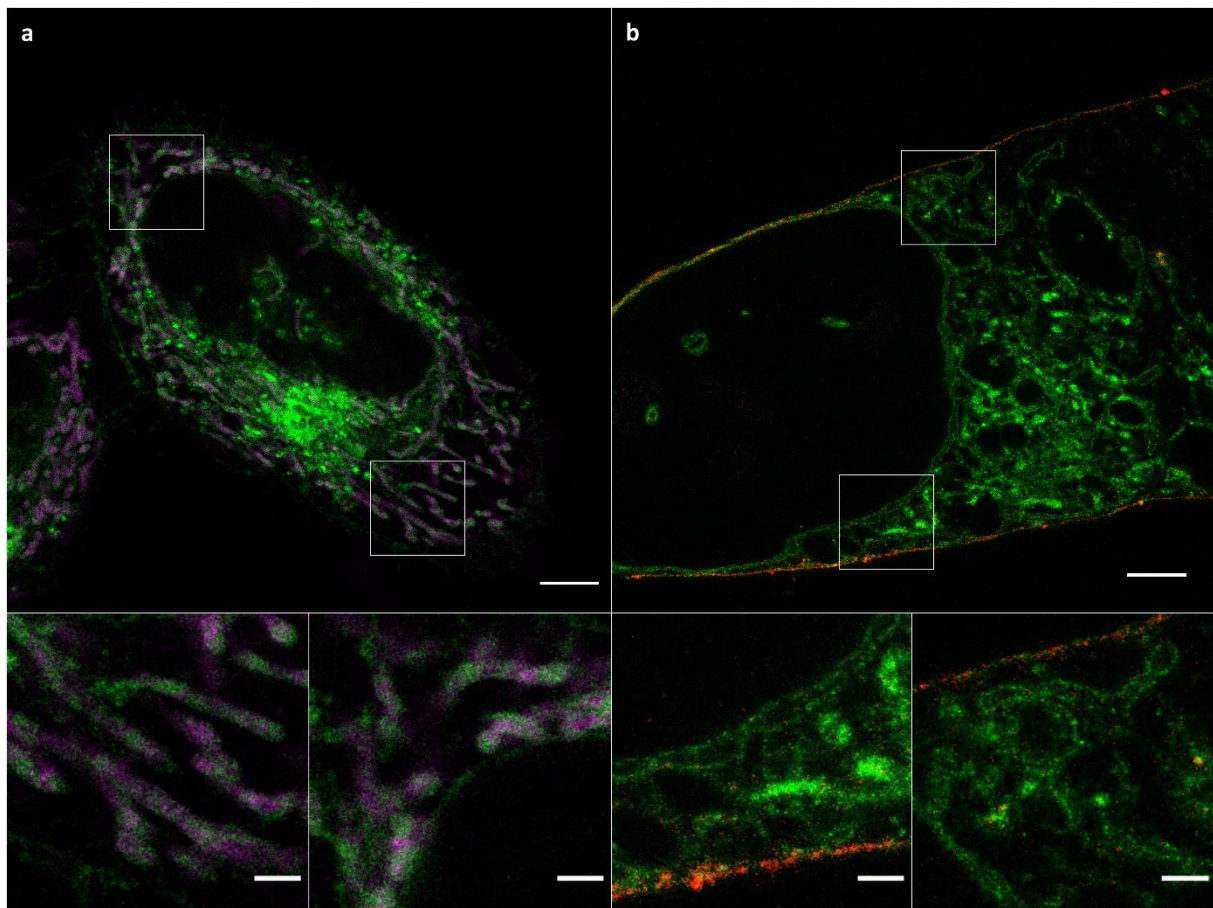
Figure 42 Sphingolipid ExM visualizes cellular membranes and protein interactions. (a) Fourfold expanded CLSM image of HeLa 229 cells. HeLa 229 cells were incubated in 10 µM α-NH$_2$-ω-N$_3$-C$_6$-ceramide, fixed, permeabilized, and click-stained with DBCO Alexa Fluor 488 (green). In addition, the mitochondrial matrix protein Prx3 was immunostained using ATTO 647N conjugated secondary antibodies. (b) Tenfold expanded CLSM images of HeLa 229 cells incubated in mCling-ATTO 643 (red) and α-NH$_2$-ω-N$_3$-C$_6$-ceramide labeled with DBCO Alexa Fluor 488 (green). Scale bars, 20 µm. The bottom images show magnifications of the by white boxes outlined main images. Scale bars, 5 µm. With permission from Götz et al. 2020a.

Next, we sought to visualize ceramides in infected cells because ceramides are of crucial im-
portance during infections with bacterial pathogens like *Chlamydia trachomatis* (Hackstadt et
al. 1996, Kunz and Kozjak-Pavlovic 2019) and *Simkania negevensis* (Herweg et al. 2016). To
first study the uptake of the bifunctional ceramide, we fed the α-NH$_2$-ω-N$_3$-C$_6$-ceramide for 5 –
60 min to HeLa 229 cells infected for 24 h with *C. trachomatis*. Confocal imaging showed
already after 5 min a rapid and highly effective integration into the bacterial membrane. This
signal increased further with longer incubation times and after 1 h the signal was even stronger
within the *Chlamydia* than in the cells' organelles (Fig. 43). Moreover, we applied HPA-12, a
specific inhibitor of the ceramide transporter CERT which is hijacked by *C. trachomatis* to gain
ceramides. The fluorescence images recorded after HPA-12 application demonstrate an im-
pediment of the ceramide uptake by the *Chlamydia* after 5 and 15 min at two HPA-12 concen-
trations. If the ceramide was fed for longer incubation times, the inhibition of HPA-12 was neg-
ligible (Fig. 43).
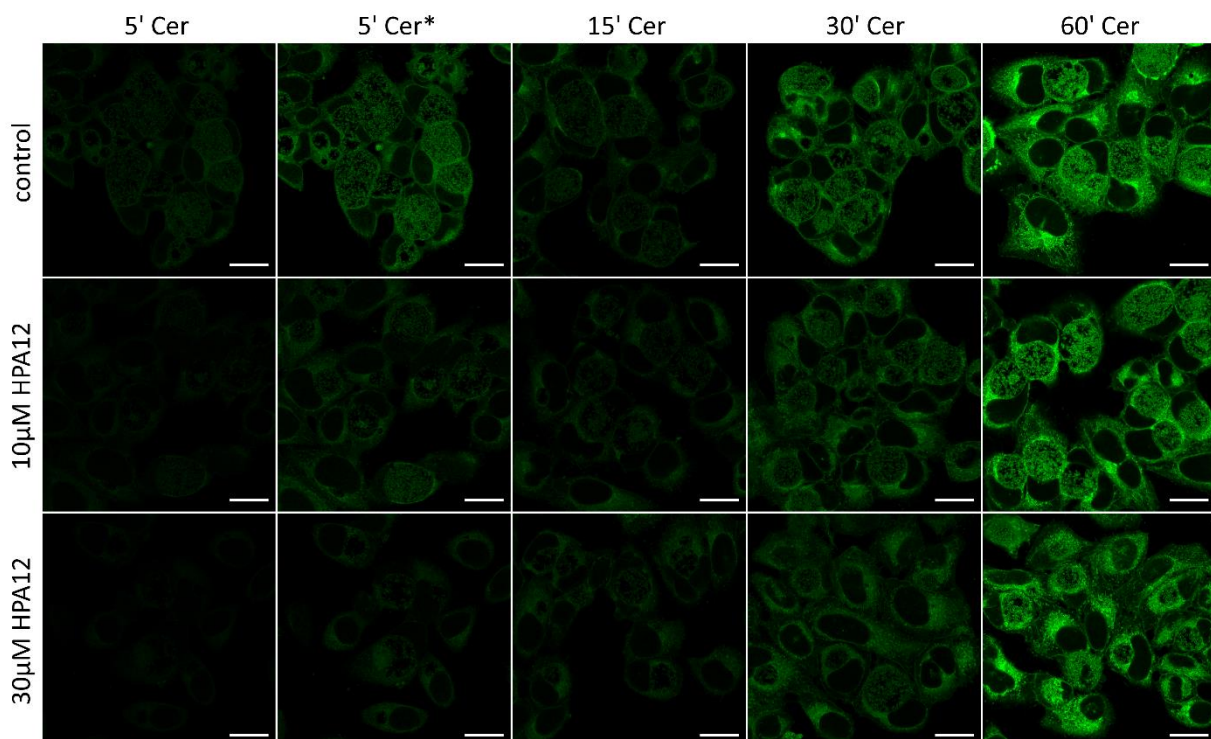
Figure 43 The CERT specific inhibitor HPA-12 inhibits the uptake of α-NH$_2$-ω-N$_3$-C$_6$-ceramides. HeLa 229 cells
were infected for 24h with *C. trachomatis* and treated with HPA-12. 8 h later HeLa 229 cells were fed with 10 µM α-
NH$_2$-ω-N$_3$-C$_6$-ceramide for 5 - 60 min, fixed, followed by permeabilization and stained with DBCO Alexa Fluor 488
(green). CLSM images demonstrate reduced ceramide uptake during the first 5 - 15 min after inhibition. For longer
incubation times little to no differences were observed. In the 5' Cer* images the contrast was enhanced for better
ceramide visualization. Scale bars, 20 µm. With permission from Götz et al. 2020a.

Next, we consequently fed our bifunctional ceramide to HeLa 229 cells infected with *S. neg-evensis* or *C. trachomatis*, fixed, permeabilized and click-stained them with Alexa Fluor 488. This was followed by the consequent application of 4x and 10x expansion protocols. As shown in previous results, fourfold expansion was sufficient to distinguish between EBs and RBs of *C. trachomatis*, however, 10x ExM was necessary to clearly identify individual *S. negevensis* bacteria (Fig. 44 a-c). Ceramides strongly accumulate in both pathogens, which becomes most obvious in 10x ExM images, compared to the relatively dim host cells (Fig. 44). Moreover, in 10x ExM, the size differences are more apparent, possibly enabling an even more delicate separation of developmental forms from *C. trachomatis* (Fig. 44 d-f) into EB, RB, dividing RBs and intermediary bodies (IB) (Lee et al. 2018).

To further demonstrate the usability of our NH_2-ω-N_3-C_6-ceramide, we studied chlamydial interactions with immunolabeled mitochondria (Prx3), since, up to now, all super-resolved studies of these interactions have been investigated using electron microscopy (Lee et al. 2018). To even further improve the resolution, we combined 10x ExM with SIM which revealed a mitochondrial reorganization around the chlamydial inclusion (Fig. 44 g). Frequently, we could even detect Prx3 signals within single *C. trachomatis*, possibly indicating an unspecific protein uptake (Fig. 44 h).

Control experiments without the primary anti-Prx3 antibody using solely the secondary antibody conjugated with ATTO 647N exclude unspecific antibody binding within the bacteria and confirm the specificity of the Prx3 signal within the *Chlamydia* (Fig. 45).

We further performed 10x ExM experiments to exclude unspecific binding of DBCO Alexa Fluor 488 and the incorporation of the not amino-modified ceramide into the gel. Neither the samples without any fed ceramide (Fig. 46 a) nor samples fed with the ω-N_3-C_6-ceramide (Fig. 46 b) showed any signal compared to our α-NH_2-ω-N_3-C_6-ceramide (Fig. 46 c).
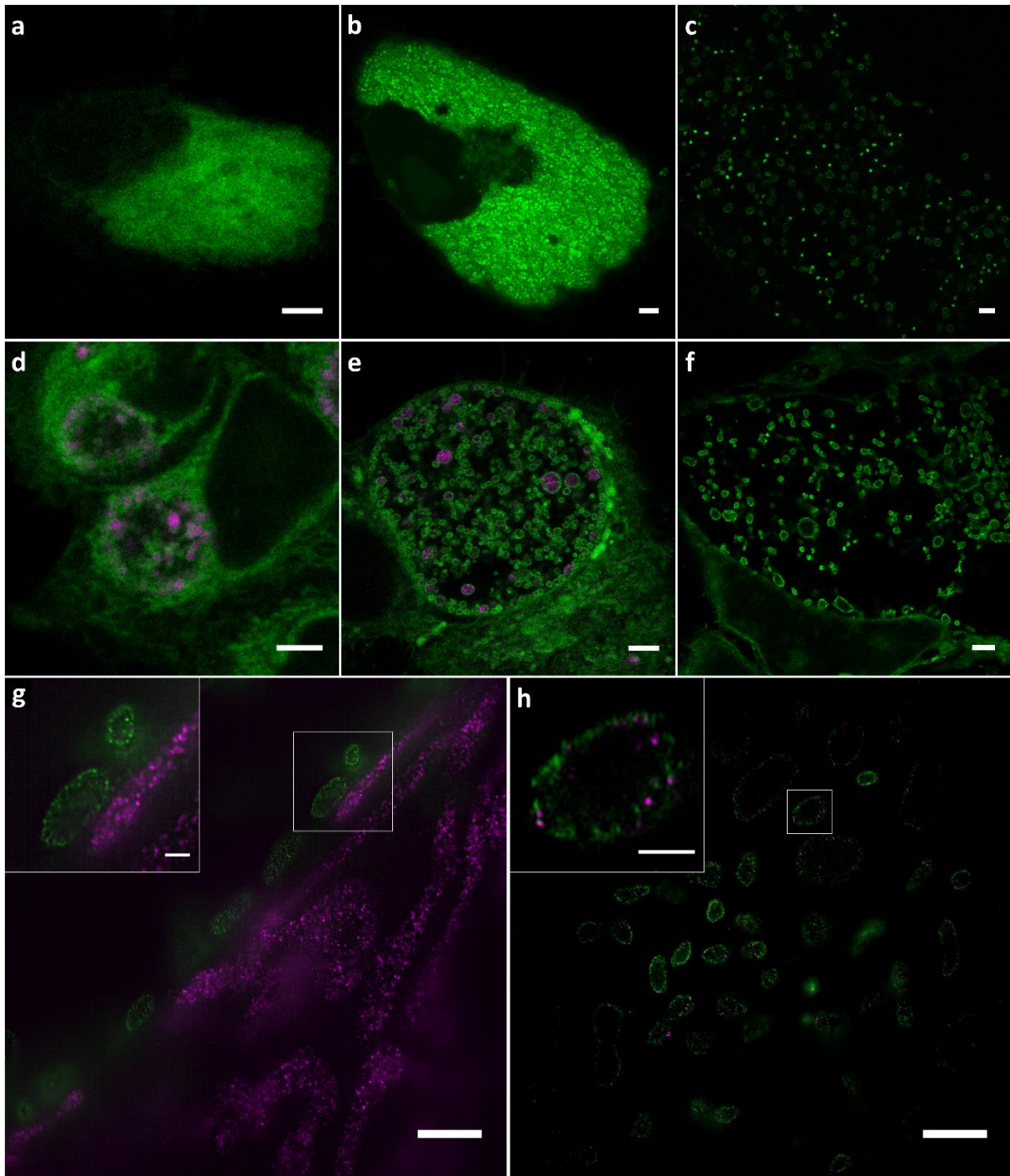
Figure 44 10x ExM of sphingolipids allows the visualization of intracellular pathogens and their interactions with mitochondria. (a-c) HeLa 229 were infected with *S. negevensis* for 96 h, fed with our α-NH₂-ω-N₃-C₆-ceramide and after fixation the samples were permeabilized and stained with DBCO Alexa Fluor 488 (green). Samples were imaged on a CLSM (a) before expansion, (b) after 4x expansion and (c) 10x expansion. (d-f) HeLa 229 were infected with *C. trachomatis* for 24 h, fed with the α-NH₂-ω-N₃-C₆-ceramide and after fixation the samples were permeabilized and stained with DBCO Alexa Fluor 488 (green). Samples were imaged on a CLSM (d) before expansion, after (e) 4x expansion and (f) 10x expansion. (g) Moreover, the mitochondrial matrix protein Prx3 was stained by immunolabeling (ATTO 647N; magenta). SIM images of tenfold expanded samples elucidate a close contact between reorganized mitochondria at the inclusion membrane and *Chlamydia*. (h) 10x ExM-SIM images reveal some Prx3-molecules within *C. trachomatis*. Scale bars, 10 μm (4x and 10x expanded samples b, c, e, f, g, h), and 2 μm (Magnifications g,h). With permission from Götz et al. 2020a.
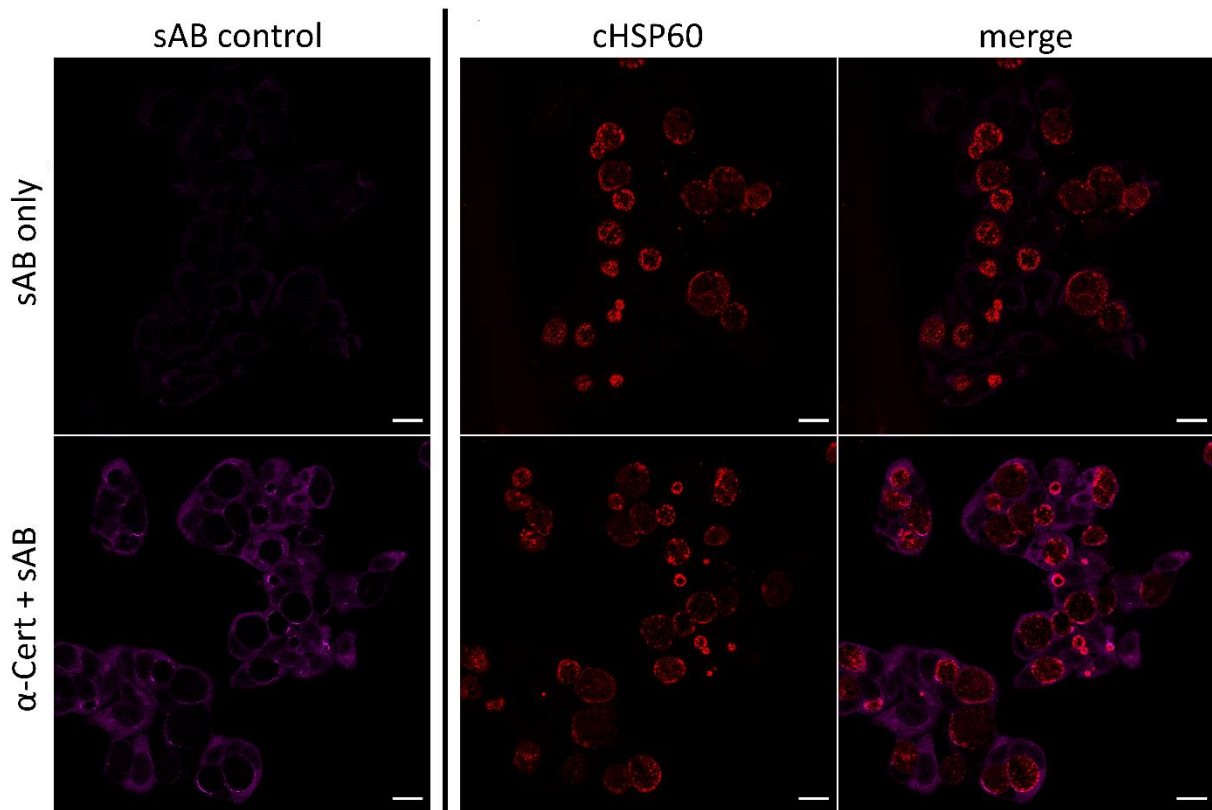
Figure 45 Confocal images of HeLa 229 cells. The cells were infected with *C. trachomatis* for 24 h, fed with α-NH$_2$-ω-N$_3$-C$_6$-ceramide, fixed, permeabilized and immunolabeled with an anti-CERT antibody (ATTO 647N; magenta) and chlamydial HSP60 (Cy3; red). The control with solely the secondary antibody resulted in no staining of the individual *Chlamydia* (sAB only/sAB control). Scale bars, 20 μm. With permission from Götz et al. 2020a.
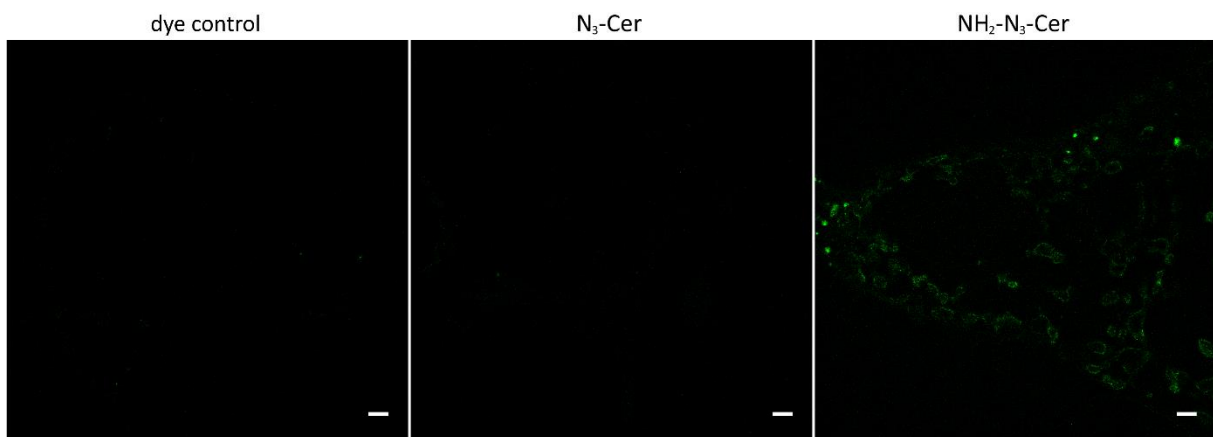
Figure 46 Confocal 10x ExM fluorescence images of with *Chlamydia trachmomatis* infected HeLa 229 cells, (a) without the incubation in ceramides (dye control), (b) with ω-N$_3$-C$_6$-ceramide (N$_3$-Cer) incubation or (c) with α-NH$_2$-ω-N$_3$-C$_6$-ceramide (NH$_2$-N$_3$-Cer) incubation. This was followed by fixation, permeabilization and staining with DBCO Alexa Fluor 488 of the sample. Only the sample incubated in the α-NH$_2$-ω-N$_3$-C$_6$-ceramide showed a staining. Scale bars, 10 μm. With permission from Götz et al. 2020a.

Ceramide transport from the host cell to the inclusion has already been investigated earlier. Hereby, it could be shown that the ceramide transporter CERT is hijacked by IncD and ceramides accumulate at the inclusion membrane and within single *Chlamydia*. However, one unanswered question remains about the localization of ceramides in the bacterial membrane. It is completely unknown whether ceramides get incorporated in the inner bacterial membrane (IM), the outer bacterial membrane (OM), or both. To address this question, we again combined 10x ExM with SIM and applied our bifunctional ceramide demonstrating an efficient ceramide incorporation into the chlamydial IM and OM. Exploiting this high spatial resolution of at least 20 nm by sphingolipid 10x ExM-SIM, we could determine the distance between the two bacterial membranes to mean 30 ± 9.2 nm (N=10) by fitting the intensity profiles at various positions using a bimodal Gaussian fit (Fig. 47) which is in good agreement with data from electron microscopy (Asmar et al. 2017). To sum up, we could expand ceramides four- and tenfold in cell lines with and without bacterial infections and demonstrated the incorporation of ceramides in both bacterial membranes.
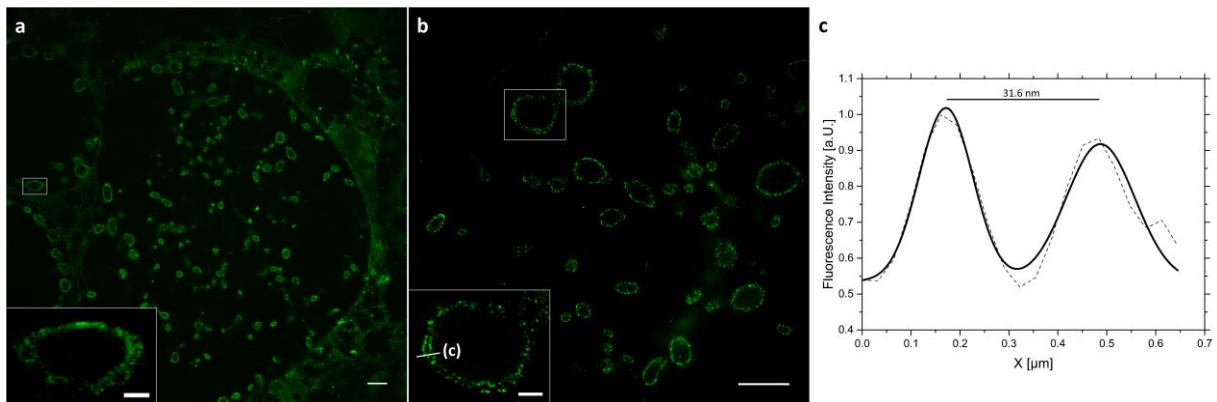
Figure 47 10x sphingolipid ExM resolves in combination with SIM the inner and outer bacterial membrane of *C. trachomatis*. With *Chlamydia trachomatis* infected HeLa 229 cells were fed for 1 h with our α-NH$_2$-ω-N$_3$-C$_6$-ceramide and fixed followed by permeabilization and click-labeling with DBCO Alexa Fluor 488 (green). (a) CLSM and (b) SIM images depict ceramide integration into the inner and outer bacterial membrane. (c) Intensity profile of a *C. trachomatis* double membrane imaged by ExM-SIM reveal a distance of 31.6 nm between the two bacterial membranes. Scale bars, 10 µm (a, b) and 2 µm (white boxes). With permission from Götz et al. 2020a.

3.2.3 Expansion microscopy of fungal pathogens

As demonstrated in the previous two chapters, ExM can provide new insights into bacterial infections. Fortunately, resolution is not only a limiting factor during bacterial, but also in fungal infections. Fluorescence microscopy of fungi is often restricted by the small size of fungal organelles making the limited resolution a severe obstacle (Chapuis, Ballou and MacCallum 2019, Hickey et al. 2004). Causing even more issues for fluorescence imaging, fungi frequently exhibit strong autofluorescence (Knaus et al. 2013). These limitations make ExM an attractive method for fungal research, as autofluorescence is strongly reduced due to signal dilution and the resolution is enhanced in ExM. To enable an isotropic expansion, the fungal cell wall first has to be degraded completely. We applied published protocols for fungal cell wall digestion and protoplast isolation and could successfully adopt ExM to *Ustilago maydis, Fusarium oxysporum* and *Aspergillus fumigatus.*

For *Ustilago maydis* we could either digest the cell wall of living fungi to obtain protoplasts or digest the cell wall directly after fixation. Both protocols can successfully be used for ExM and enabled an approximately fourfold isotopic expansion. In protoplasts the cytoskeleton, stained for α-tubulin, is reorganized compared to naïve hyphae and sporidia (Fig. 48) (Anderson and Millbank 1966, Peberdy 1979).

Importantly, incomplete digestion of the cell wall resulted in an impeded or in no expansion. This incomplete digestion could be confirmed by chitin staining of the chitin specific dye Calcofluor white. It should be noted that only in case of an incomplete cell wall digestion a Calcofluor staining could be detected and only in these regions an isotropic expansion was not successful (Fig. 49).
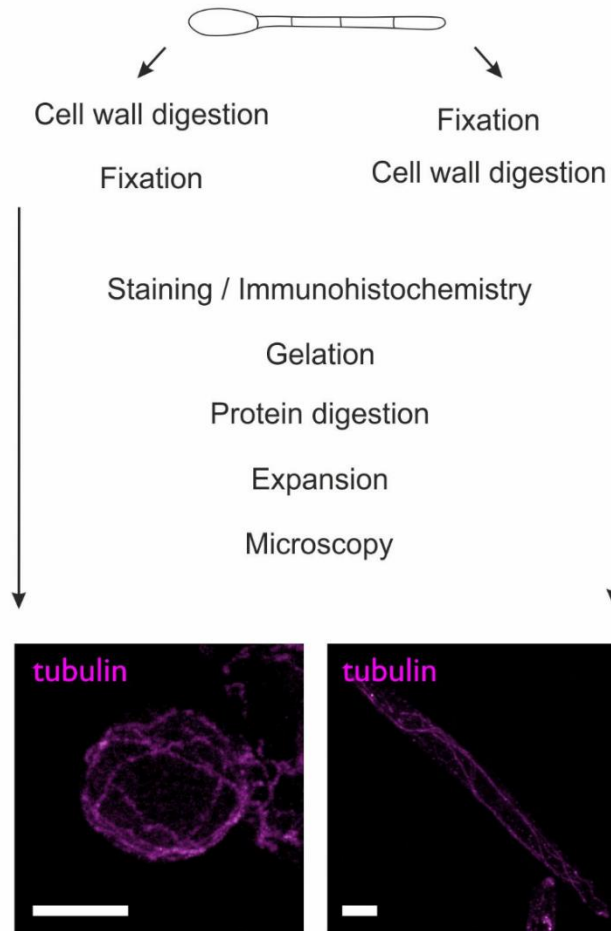
Figure 48 Schematic overview of the ExM protocol for fungi. Cell wall digestion as most crucial step was performed either before fixation to form protoplasts or after fixation to sustain sporidia of *U. maydis*. Confocal ExM images of protoplasts (left) and sporidia (right) immunostained for α-tubulin with ATTO 647N are shown. Scale bar, 10 μm. With permission from Götz et al. 2020b.
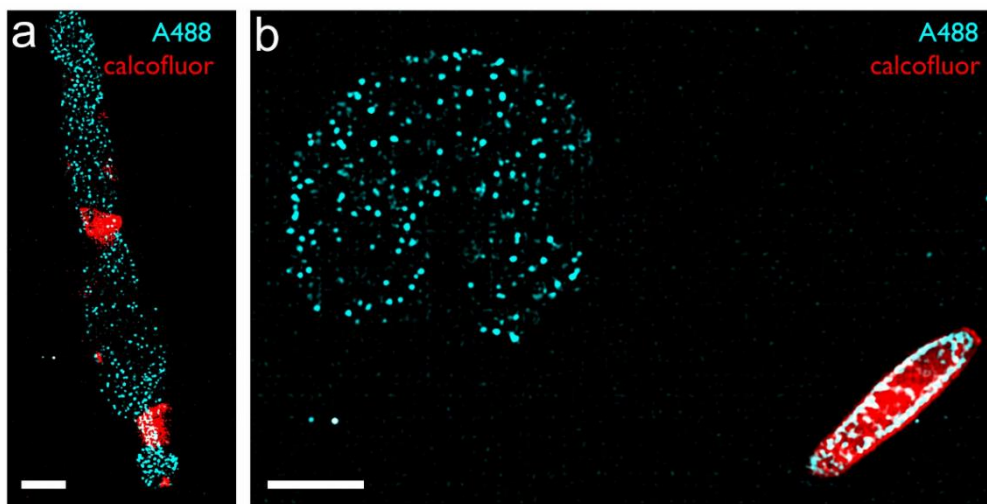
Figure 49 SIM images of incomplete digested of *U. maydis* (a) sporidia and (b) protoplasts. Incomplete cell wall digestion results in non isotropic expansion of both sporidia and protoplasts. Remaining cell wall parts are stained with Calcofluor white (red). The fungal shape was visualized by unspecific binding of an Alexa Fluor 488 conjugated secondary antibody. Only regions stained by Calcofluor show an impeded expansion. Scale bars, 5 μm. With permission from Götz et al. 2020b.

We next immunostained α-tubulin with Alexa Fluor 488 conjugated secondary antibodies and the plasma membrane of *Ustilago maydis* using mCling ATTO 643. Following expansion, the exact comparison of pre-expansion (diameter of 2.4 ± 0.35 µm) and post-expansion (diameter 11.0 ± 1.08 µm) fungi confirms an isotropic expansion by a factor of 4.6 of both structures in *Ustilago maydis*. Importantly, membrane vesicles were clearly detectable in expanded *Ustilago maydis* (Fig. 50 B). Moreover, we analyzed the compatibility of fungal ExM with membrane proteins like the green light-driven proton pump UmOps1 which was fused to GFP (Panzer et al. 2019). In both, pre- and post-expansion images UmOps1 could be detected within the membrane. In the expanded sample however, the membrane protein UmOps1 seemed more dot like due to the improved resolution and the high signal dilution during expansion.
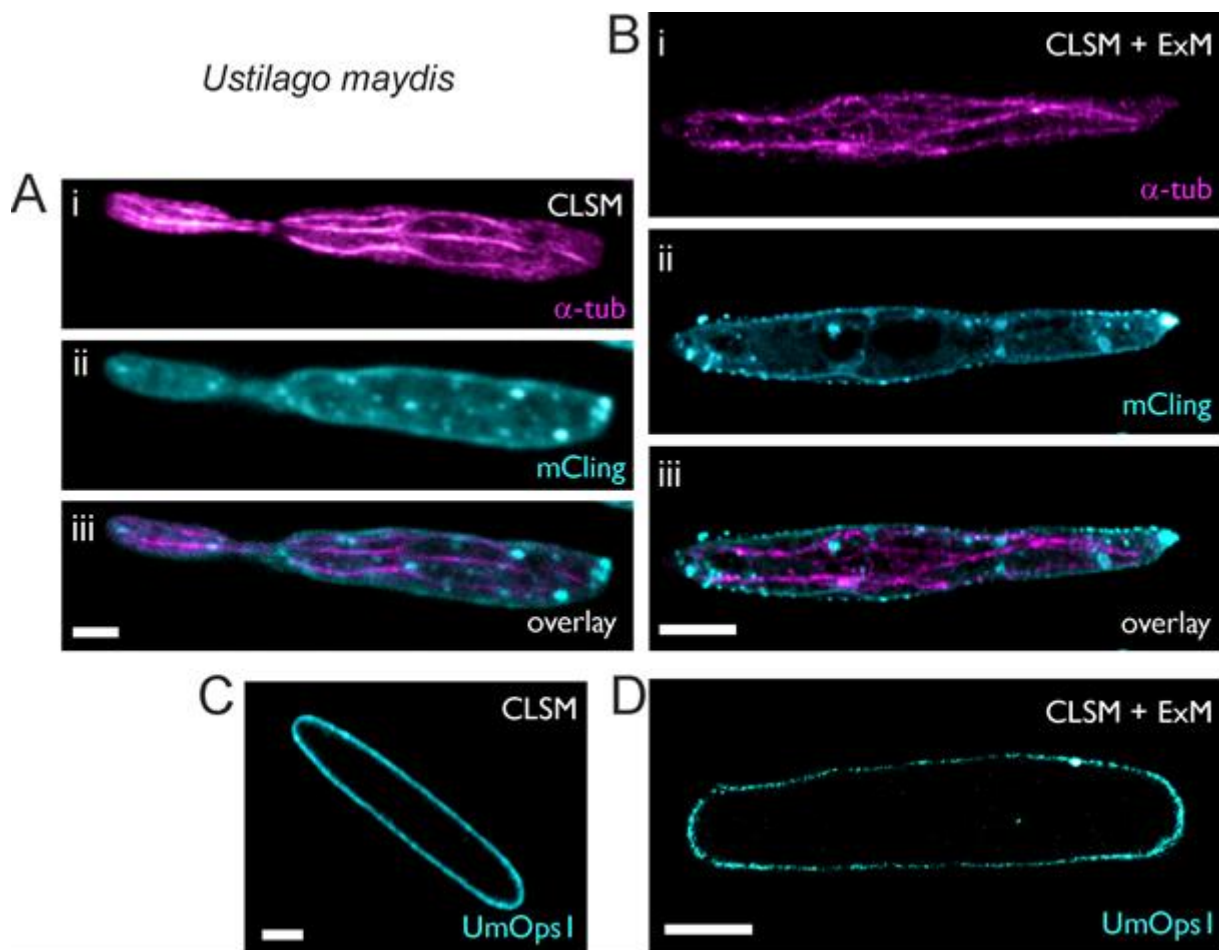
Figure 50 Expansion microscopy of *Ustilago maydis* sporidia (A, C) before and (B, D) after expansion. Sporidia were immunostained for α-tubulin with Alexa Fluor 488 (i, magenta) and additionally the plasma membrane was stained with mCling ATTO 643 (ii, cyan). Both, tubulin and stained vesicles, benefit from an improved resolution by ExM. Confocal images of the fungal rhodopsin UmOps1 fused to eGFP which localizes in the plasma membrane *of U. maydis* sporidia. (D) After expansion, the UmOps1 distribution is more dot like within the membrane than (D) before expansion. Scale bars, 2 µm (A, C) and 10 µm (B, D). With permission from Götz et al. 2020b.

The ascomycete *F. oxysporum* on the other hand inhabits the soil and causes wilt disease in over 100 crop species. Moreover, reports about opportunistic human pathogenicity exist. In these experiments we used a *F. oxysporum* strain which expressed the histone H1 together with mCherry (Ruiz-Roldan et al. 2010). Again, we first imaged unexpanded *F. oxysporum* (diameter of 2.89 ± 0.49 µm; n=17) using SIM with a by mCling ATTO 643 stained plasma membrane additionally to the H1-mCherry expression. Following cell wall digestion and expansion the diameter of the hyphae increased to 12.73 ± 0.71 µm (n=4) resulting in an expansion factor of 4.4. Moreover, as SIM provides an only limited resolution for fungal intracellular structures, ExM-SIM clearly resolves detailed organelles, vesicles and H1-labeled nuclei with different densities. Interestingly, depending on the incubation time, mCling also labeled the membrane of intracellular organelles (Fig. 51 B).

Additionally to the nucleus, we sought to visualize the cytoskeleton of *F. oxysporum*. Hence, we generated a strain which expressed the F-actin reporter LifeAct-GFP (Riedl et al. 2008) together with H1-mCherry. The actin filaments clearly localized at the hyphal tip. After expansion by contrast, the actin filaments were substantially better distinguishable and even single cables were visible. Moreover, not only in SIM-ExM as before, but also in confocal ExM different histone densities within the nucleus were apparent (Fig. 51 D).

Especially in *F. oxysporum* we noticed a deteriorated expansion after long germination times due to incomplete cell wall digestion (Fig. 52). It is known that, depending on the germination time, the cell wall composition of fungi changes (Reilly and Doering 2010, Li et al. 2017) and therefore the germination time has to be carefully considered when using ExM to avoid artifacts.
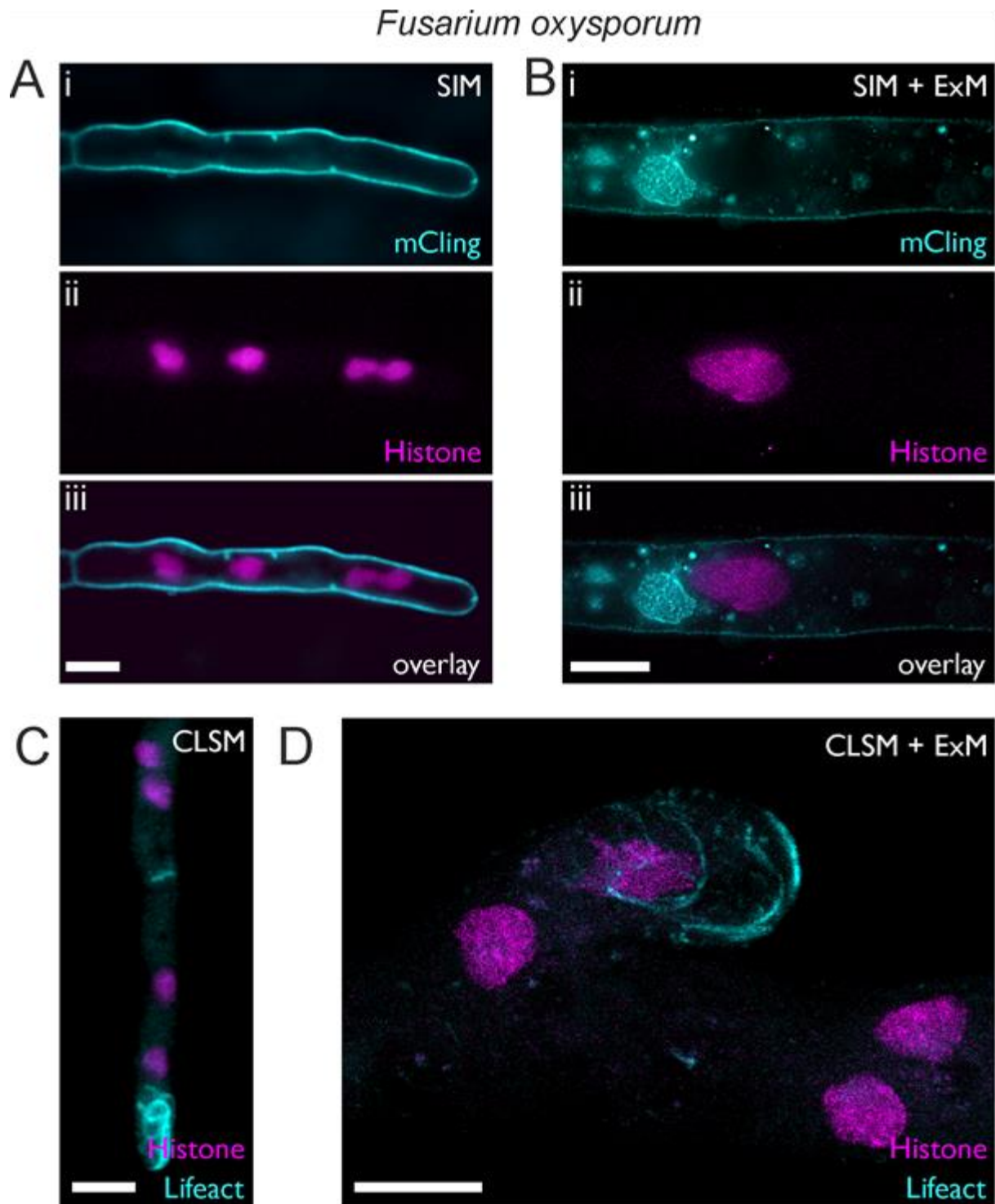
Figure 51 SIM and confocal images of expanded *F. oxysporum* acquired (A, C) before and (B, D) after expansion. *F. oxysporum* hyphae expressed histone H1-mCherry and are stained additionally with mCling ATTO 643. After expansion more details within the nucleus were visible. (C, D) Confocal ExM images of *F. oxysporum* expressing additionally Lifeact-GFP visualize single actin fibres with an improved resolution after expansion. Scale bars, 5 µm (A, C) and 10 µm (B, D). With permission from Götz et al. 2020b.
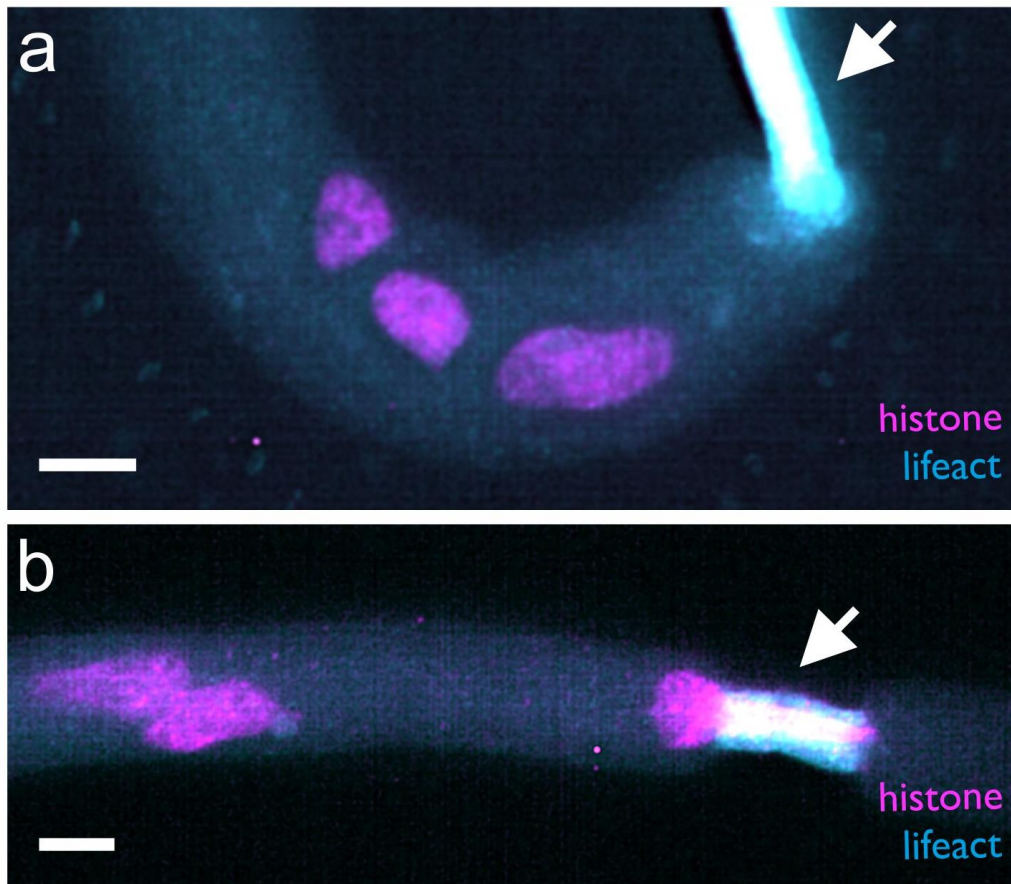
Figure 52 Confocal images of not isotropic expansion of *F. oxysporum* hyphae expressing histone H1-mCherry (magenta) and LifeAct-GFP (cyan). (a, b) Due to incomplete cell wall digestion not all parts of the hyphae could be expanded isotropically. The arrows indicate the areas of incomplete expansion and an accumulation of actin fluorescence. Scale bars, 5 μm. With permission from Götz et al. 2020b.

After working with plant pathogens, we focused on *Aspergillus fumigatus* which can cause the invasive disease aspergillosis, especially in immunocompromised patients (Brown et al. 2012). This fungus is nearly ubiquitous present in the air due to the enormous conidia production. For our investigations we used an *A. fumigatus* strain expressing mRFP together with the N-terminus of a citrate synthase localizing in mitochondria. To label the plasma membrane and visualize the shape of the hyphae we used again mCling ATTO 643. Prior to the expansion, we measured a hyphae diameter of 2.43 ± 0.27 μm (n=9) which increased after expansion by a factor of 4.4 to 10.7 ± 0.7 μm (n=17). Moreover, the shape of single mitochondria was barely distinguishable before expansion, whereas after expansion single mitochondria could clearly be resolved (Fig. 53). Unfortunately, RFP strongly suffers from the proteinase's digestion resulting in only a weak fluorescence signal (Tillberg et al. 2016). To improve this, other fluorescent proteins like mCherry or tdTomato and an additional immunostaining could be beneficial. Collectively, we could demonstrate here the successful application of ExM to three different fungi after removal of their cell wall.
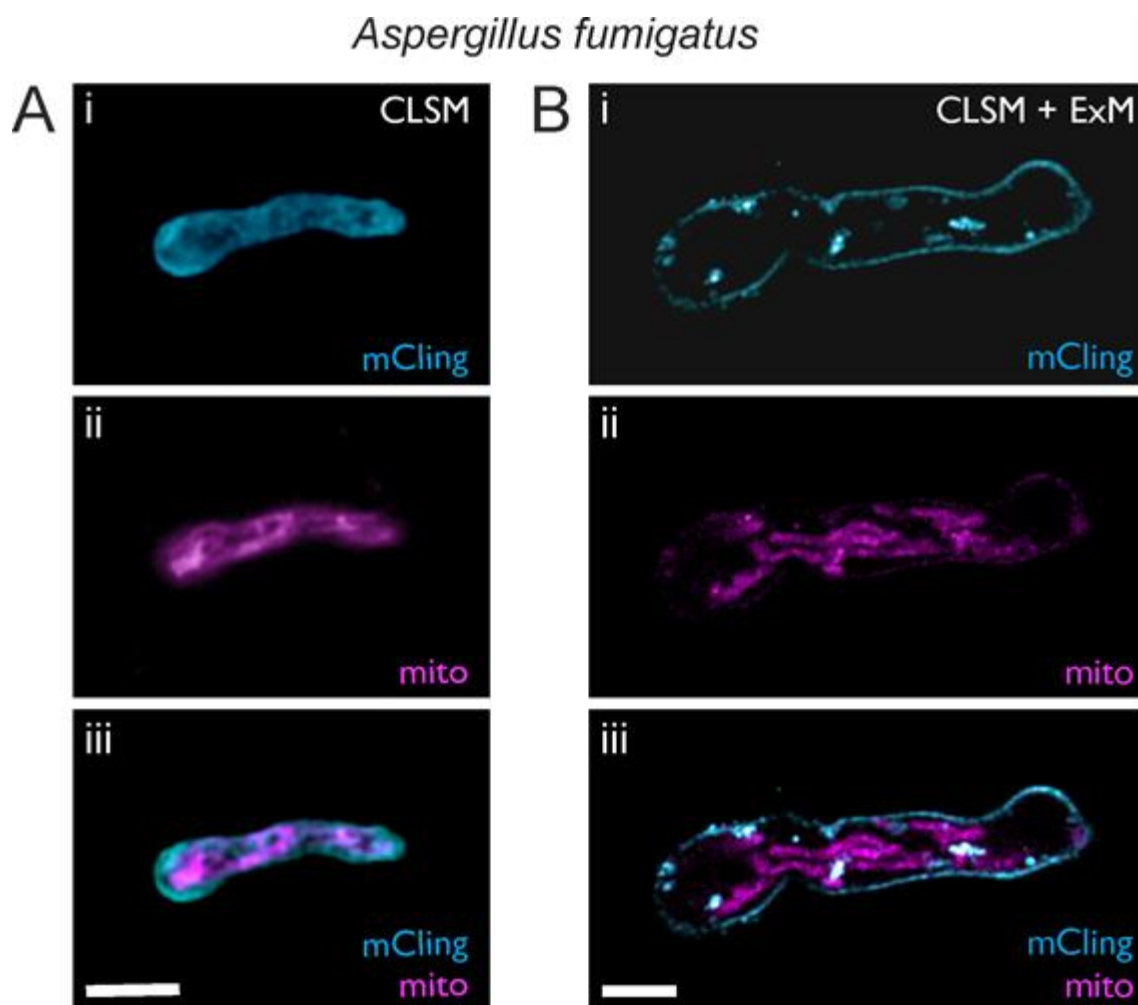
Figure 53 Confocal images of *A. fumigatus* with mRFP-labeled mitochondria (magenta) and mCling ATTO 643 (cyan) labeled plasma membrane (A) before and (B) after expansion. Single color images of (i) mCling, (ii) mitochondria and (iii) the overlay. After expansion, the mitochondrial shape and the plasma membrane can clearly be better resolved. Scale bars, 5 µm (A) and 10 µm (B). With permission from Götz et al. 2020b.

3.3 Summary

To summarize the results, we could successfully establish a staining protocol for the single molecule sensitive quantification of membrane receptors on not only Jurkat T-cells but also primary T-cells with up to three colors. After that, we applied this quantification protocol to the receptors CD38 and BCMA after exposure to various drugs and demonstrated a superior sensitivity of *d*STORM compared flow cytometry. Moreover, we used LLS-3D *d*STORM and 10x ExM to visualize whole T-cells excluding artifacts caused cell adherence or interactions. We also established ExM to investigate bacterial and fungal infections, in case of fungi by removing the cell wall enzymatically. Next, we could even enable the expansion of ceramides by the addition of a primary amine which enabled the first successful ExM experiments of lipids.

4 Discussion and outlook

4.1 Receptor imaging and quantification

In the first part of this thesis we could successfully establish *d*STORM for the single molecule sensitive quantification of plasma membrane receptors of Jurkat T-cells and primary naïve and activated T-cells. We further implemented this method in clinically relevant projects involving the receptors CD38, BCMA and CD20. First, we introduced a novel method to visualize and quantify the "Receptome", the entirety of all membrane receptors on T-cells, with so far unprecedented sensitivity. We could demonstrate a mostly homogeneous receptor distribution for the investigated antigens (CD2, CD4, CD11a, CD20, CD28, CD45, CD69 and CD105), while others tended to form clusters (CD3, CD5 and CD7). Using *d*STORM, we could quantify these antigens and determine receptor densities ranging from 0.8 ± 0.1 cluster/µm² for CD20 in primary activated CD8⁺ T-cells to 81.4 ± 1.7 cluster/µm² for CD45 in naïve CD8⁺ T-cells. Considering the total number of antigens, the amount of antigens ranged from 241 ± 161 in naïve primary CD4⁺ cells to even 13630 ± 2464 CD45-molecules in activated CD4⁺ T-cells. These differences underline the importance of considering the cell size, as not only the antigen density, but also the differing total antigen number might be relevant, especially when comparing *d*STORM results to those obtained by flow cytometry, where always the whole cell is analyzed. This could also demonstrate that our quantification protocol can not only be used in cell lines, but also be translated to primary cells. Furthermore, we also revealed substantial differences in both, the total number and density of the analyzed antigens between cultured Jurkat T-cells and primary T-cells. This raises questions about the comparability between cultured cells in general and primary cells which has already been addressed by many others laboratories (Pan et al. 2009, Kaur and Dufour 2012).

Moreover, we could also confirm that in naïve primary T-cells CD3 is homogeneously distributed, as recently published (Rossboth et al. 2018). Solely upon activation, we could detect clustered CD3 molecules in both, activated primary cells and Jurkat T-cells which are known to be at least partially activated due to IL-2 production (Pawelec et al. 1982).

However, also unspecific antibody binding within a range of 0.2 cluster/µm² occurred corresponding to ~70 molecules on the cell. This might be limiting in further experiments and should therefore be optimized as much as possible by precleaning the glass surfaces of the imaging chambers and by the use of carefully optimized antibody concentrations.

After demonstrating a severe signal loss when using Alexa Fluor 532 compared to Alexa Fluor 647, we also established DNA-exchange *d*STORM (Schueder et al. 2017) which showed to be

reliable in quantification experiments. Albeit successful in the end, alternative protocols to efficiently conjugate oligonucleotides at specific antibody sites might be beneficial to improve the degree of labeling. Possible approaches could be the introduction of unnatural amino acids (Axup et al. 2012, Beliu et al. 2019), SNAP-tags (Cole 2013, Hussain et al. 2019) or proximity induced antibody conjugations (Yu et al. 2018).

However, when using antibodies for quantitative imaging, the question of epitope accessibility will arise in this context. This very reasonable concern could even be encouraged by a recent comparison of antibodies directed against NMDA-receptors with click chemistry using unnatural amino acids which allowed the labeling of considerably more receptors than with antibodies (Neubert et al. 2018). Although this is a valid argument, this concern is not of relevance in case of quantitative imaging for diagnostics in immunotherapy because nearly all immunotherapeutic approaches including monoclonal antibodies, CAR T-cells, bispecific antibodies or splitted antibodies use at least fragments derived from antibodies (Feins et al. 2019, Frankel and Baeuerle 2013, Banaszek et al. 2019, Plesner and Krejcik 2018). Hence, after staining with antibodies, the quantifications will detect as much antigens as can be addressed by the corresponding immunotherapy. Therefore, it is not only sufficient, but even fundamental to use antibodies to label the antigen of interest.

Within this work we also applied 3D-LLS *d*STORM to enable the super-resolved visualization of a whole Jurkat T-cell stained with antibodies directed against CD45 (Wäldchen et al. 2020) and CD3. Using this technique, we could successfully exclude potential artifacts induced by interactions between the glass surface and the T-cell or membrane proteins.

In the collaborative projects together with the Hudecek group of the University Hospital of Würzburg we could further demonstrate the applicability of our approach to primary patient cells. First, we performed correlative studies using microscopy and flow cytometry measurements to investigate the response of multiple myeloma cells after the exposure to histone deacetylase (HDAC) inhibitors and ATRA on the antigens CD38 and BCMA. Hereby, we could first demonstrate in MM1.S cell lines that the novel drug ricolinostat, a specific histone deacetylase 6 inhibitor, could increase the CD38-expression more effective than the approved drugs panobinostat and ATRA. Importantly, this effect occurred also in primary cells from multiple myeloma patients, even after prior treatment with the therapeutic antibody daratumumab and subsequent decrease in CD38 levels. Using *d*STORM was especially beneficial when investigating the daratumumab pretreated primary cells because in this case the CD38-expression was at a low level of only 6.8 ± 1.1 cluster/µm². Upon treatment with ricolinostat, *d*STORM could detect also very subtle changes in the CD38-expression to 10.8 ± 1.7 cluster/µm² which were barely detectable by flow cytometry, but still of therapeutic relevance. Similarly, we could also detect a slight but significant increase of BCMA-levels in MM1.S cell upon treatment with 100 µM ATRA from mean 6.1 ± 0.4 to 8.2 ± 0.6 cluster /µm². In both cases the quantification

using *d*STORM provides the potential to accurately measure antigen numbers with a strongly enhanced sensitivity compared to flow cytometry.

This superior sensitivity could be demonstrated within the CD20-project, where we visualized and quantified CD20 in primary multiple myeloma patient cells. The comparison to flow cytometry analysis revealed, similarly to previous CD19 investigations (Nerreter et al. 2019), that the sensitivity of flow cytometry is not high enough to detect all CD20-positive myeloma cells. According to flow cytometry analysis of the two CD20-positive patients, solely 17% to 33% of all cells were positive for CD20, while *d*STORM revealed 65% to 77% CD20-positive cells. We assume that in many cases a low antigen expression below the flow cytometry sensitivity, as in the Garfall et al. study (Garfall et al. 2015), is present. In this case, a patient estimated CD19-negative by flow cytometry was treated with CD19 CAR T-cells resulting in a complete response. As with a second antigen, CD20, more CD20-positive cells could be detected by dSTORM compared to flow cytometry, we expect that many tumor associated antigens cannot be detected within the clinical routine.

Although very useful for antigen quantifications with superior sensitivity, *d*STORM is extremely time consuming when large sample sizes are needed. This is mostly apparent when quantifying primary cells from cancer patients to ensure the greatest accuracy within these experiments. This issue will cause even more problems in the future, as in most cancer types not only one, but many antigens will be important possible target molecules. Examples are in case of multiple myeloma the receptors CD19, CD20, CD38, CD40, CD44v6, CD138, CD229, SLAMF7, BCMA and EGFR (Nerreter et al. 2019, Chu et al. 2014, Giuliani and Malavasi 2019, Prommersberger et al. 2018, Liebisch et al. 2005, Atanackovic et al. 2011). Hence, there will be the need to image and quantify whole antigen "panels" with huge statistics to approach personalized immunotherapy with single molecule sensitivity.

To address this, it is indispensable, although very challenging, to automatize the whole process of *d*STORM imaging. Hereby, many things need to be perfectly optimized. First, the initial identification of appropriate cells has to be solved by using for example deep learning algorithms. By applying such approaches, many exemplary cell images can be used to train the algorithm, even with only ten training images for specialized algorithms. However, if the training images are not ideal, this may also cause wrong or dead cell recognition (Falk et al. 2019). Furthermore, the imaging itself might cause problems when considering the correct adjustment of the TIRF, possible drift or high background conditions.

As already mentioned, in many cases also several antigens within one sample will be important which will necessitate also an automated washing and restaining procedure. Here, again DNA-exchange *d*STORM might be the method of choice as it could be shown within this work that the quantitative use of this method for receptor imaging is possible. Importantly, DNA-exchange is also extremely fast, accelerating multi-color experiments dramatically. In order to

efficiently and fast exchange all the required buffers, microfluidics could be applied. Microfluidics were already shown to be perfectly suited for sequential stainings and imaging which was demonstrated by a recent example from Nir et al., where microfluidics were used to "walk" on chromosome 19 within 21 rounds of sequential *d*STORM and PAINT imaging (Nir et al. 2018). Of course, not only single tumor suspension cells need to be quantified with *d*STORM sensitivity, but ultimately also slid tumor tissue. Hereby, other issues will arise considering efficient antibody penetration of the sample, extensive background from other planes and enhanced autofluorescence. To enable an improved antibody penetration, tissue clearing protocols like CLARITY (Du et al. 2018, Chung et al. 2013) have been involved. Similarly to expansion microscopy, the tissue is covalently cross linked with formaldehyde and hydrogel monomers which allows its incorporation into a hydrogel mesh after polymerization. Instead of a digestion step like in expansion microscopy, now an electric field is applied to the sample within an electrophoretic tissue clearing (ETC) chamber to rigorously transport micelles into and lipids out of the sample. Importantly, the fine structure is preserved because the prior crosslinked biomolecules remain in place within the hydrogel meshwork. Following clearing, the sample can be rapidly immunostained and after imaging the antibodies can efficiently be removed again using detergents. This could consequently enable quantitative multi-color *d*STORM imaging of solid tumor tissue like breast cancer or melanoma tissue.

Even if *d*STORM analysis would be completely automatized, flow cytometry will probably remain the standard diagnostic method due to its enormous speed for higher expressed antigens, albeit the severe lack in sensitivity could be demonstrated. Nevertheless, in cases of uncertain antigen expression or no antigen detection *via* flow cytometry, *d*STORM can be an indispensable tool for diagnostics within the clinics, especially in the field of personalized immunotherapy.

Although immunotherapies are nowadays widely used, there is still a lack of knowledge about the precise mechanism of immune cell signaling and signal transduction between immune cells (Rossy et al. 2013). Here, super-resolution microscopy could already shed some light on the distribution of CD3 (Rossboth et al. 2018), the remodeling of the adaptor protein LAT upon TCR activation (Sherman et al. 2011) or the formation of immunological synapses (Yakovian et al. 2018, Hu, Cang and Lillemeier 2016). Unfortunately, although three-dimesional super-resolution of whole e.g. interacting T-cells is urgently needed, conventional *d*STORM is mostly limited to 2D imaging due to the need of TIRF imaging for an ideal signal to noise ratio. Here, 3D-LLS *d*STORM could provide the possibility of quantitative super-resolved 3D imaging of whole cells. This can enable the visualization of the three dimensional interaction sides of a T-cell and an antigen presenting cell or pave the way for investigations between the cytoskeleton and membrane proteins on immune cells. Especially highly three-dimensional structures like the reorganization of actin or tubulin upon antigen recognition could be beautifully addressed

using this technique. It would be also interesting to compare the killing of various immunotherapeutic approaches not only involving CAR T-cells, but also monoclonal antibodies, bispecific T-cell-engaging antibodies (BiTes) (Frankel and Baeuerle 2013) or split T-cell engaging antibodies (hemibodies) (Banaszek et al. 2019). Contrary to monoclonal antibodies and CARs, BiTes are composed of two single chain antibodies directed against CD3 and a tumor associated antigen. Hence, BiTes induce the formation of an immunological synapse by simultaneous binding to a T-cell and a tumor cell expressing the targeted tumor associated antigen resulting in the lysis of this cell. Similarly to CAR T-cells this response is also MHC-independent, bypassing immune escape mechanisms as well as complex T-cell regulations. Split antibodies on the other hand address the issue of target antigen expression by non-tumor cells, as this has already led to severe side effects (Hansel et al. 2010, Morgan 2013). Therefore, the tri-specific antibody is halved, and each half (hemibody) consists out of an antigen binding domain (scFv) and a heavy or light chain of a T-cell activating antibody directed against CD3. Upon complementary hemibody binding to two different antigens in close vicinity, the light and heavy domains associate and form a CD3 binding site to activate T-cells and induce tumor cell lysis. Also here, the exact mechanism of the formation of the immunological synapse could not be elucidated yet, due to current microscopic limitations which makes super-resolved 3D imaging of whole cells by 3D-LLS dSTORM extremely valuable.

Another less elaborate method used within this thesis to visualize whole cells at a resolution of ~25 - 30 nm is 10x ExM (Truckenbrodt et al. 2018, Truckenbrodt et al. 2019). Here, there would be no need for a measurement lasting for hours and an intensive post-processing to render a final image like in 3D-LLS dSTORM. Within this thesis, it could be demonstrated that both, adherent U2OS and Jurkat T-cells, could be isotropically expanded tenfold. 10x ExM was not only compatible with the imaging of standard intracellular targets like tubulin or mitochondria using primary and secondary antibodies, but also with the imaging of plasma membrane receptors labeled with directly conjugated primary antibodies. However, in 10x ExM CSLM was not able to detect unclustered receptors stained solely with directly dye conjugated primary antibodies. Signal amplification using biotinylated antibodies and streptavidin ATTO 643 on the other hand could successfully visualize also unclustered receptors, even the heterodimer CD11a. This demonstrates that after signal amplification even single antibodies can be visualized using the 10x ExM protocol. Yet, it is very unclear how many antibodies are incorporated into the hydrogel, although the NHS-reaction using AcX to link the antibodies into the gel should be efficient. But unfortunately, it is also unknown if all acrydite groups are incorporated into the gel. Hence, it would be very beneficial for the whole field of expansion microscopy if this issue could be addressed.

Another strongly limiting step is besides the dye loss during gelation, the digestion by the unspecific proteinase K which can decrease the signal by up to 50% causing detection problems,

especially at high expansion factors (Truckenbrodt et al. 2019, Tillberg et al. 2016). Therefore, if the remaining fluorescence may be too weak, a decrease in the digestion duration may preserve the fluorescence signal. But when decreasing the digestion time, care has to be taken to avoid artifacts by non isotropic expansion. Lastly, as in 10x ExM the signal density is diluted tenfold in every dimension, which results in a 1000-fold decrease in signal density, it will be substantial to equip all setups used for ExM with higher expansion factors with single molecule sensitive cameras or photodetectors. This might enable the detection of even single into the gel incorporated antibodies without signal amplification.

Due to these limitations, it is very unlikely that ExM will be used in the near future for quantitative single molecule imaging, although the comparison of CD3 data coming from *d*STORM imaging of the basal membrane and 10x ExM was very surprising. According to the extrapolated *d*STORM data a Jurkat T-cell has on average 1440 ± 1353 CD3-clusters on the membrane surface, while in ExM on average 2017 ± 130 CD3-clusters were counted. Considering the unknown biotinylation degree of the antibodies, different antigen "counting" *via* IMARIS in ExM and clustering with the DBSCAN in localization data, the small sample size in ExM, it is difficult to really compare these results. Moreover, in case of CD2 and CD11a less receptors were counted in ExM than in *d*STORM making an interpretation of the data even more challenging.

Especially fascinating was the observation of CD2 dimers after staining with a biotinylated antibody directed against CD2, signal amplification and subsequent tenfold expansion. First, as already discussed, it is not expected that all antigens are labeled when using antibodies in both, ExM and *d*STORM. Second, both the biotinylation degree of the anti-CD2 antibody and the incorporation effectivity of the antibody into the hydrogel are completely unknown. Third, the digestion step by the unspecific proteinase K will also cleave before and after dye molecules resulting in the loss of dyes (Truckenbrodt et al. 2019, Tillberg et al. 2016). Lastly, probably not all antibody labeled molecules will be detected due to insufficient sensitivity of the used detector in CLSM and SIM.

Therefore, to address the label efficiency, it could be beneficial to use the fast and effective labeling of tetrazine-modified dyes and *trans*-cyclooctene-lysine (TCO) *via* a strain-promoted inverse electron-demanding Diels-Alder cycloaddition. Hereby, a requirement would be a site directed mutagenesis in the protein of interest to introduce an amber stop codon and the transfection with both, an unnatural tRNA-synthetase and the mutated protein sequence. Simultaneously, the unnatural amino acid is introduced which will be effectively incorporated into the mutated protein. The TCO-modified proteins can then be stoichiometrically "clicked" by the addition of tetrazine-modified dyes (Neubert et al. 2018, Beliu et al. 2019). Besides effective labeling, the label size is a major advantage of using this click chemistry. Here, the dye is directly labeled to the protein of interest resulting in the smallest possible linkage error.

This approach could be adopted to label not only dimers like CD69, but also trimers like TNF receptors (Cui et al. 2018), especially in comparison with antibodies. Due to stoichiometric labeling, the signal will have to be amplified in 10x ExM as well which could be a major limitation in this approach. Unfortunately, each amplification method will increase the label size again, making a staining after expansion inevitable, especially at higher expansion factors.

Although protocols for tenfold and even twentyfold expansion by iterative ExM already exist, a molecular resolution is not available yet which resulted in attempts to combine ExM with other super-resolution methods. This combination might enable also the visualization of multimerized receptors.

Due to no special photophysical requirements and no need for a switching buffer, STED was first combined with ExM called ExSTED (Gao et al. 2018). Hereby, STED was solely applied to fourfold expanded gels and further investigations will be needed to evaluate the compatibility of STED with 10x or iterative ExM.

Recently, also the combination of fourfold ExM with *d*STORM was reported (Xu et al. 2019), although only a threefold expansion was provided due to slight shrinking caused by the applied switching buffer. Hence, the authors claim to achieve an impressive lateral resolution of up to 10 nm in mouse spermatocytes. Of course, also in this case the combination with higher expansion factors would be highly interesting to push the resolution even below 10 nm to approach a molecular resolution. However, as already discussed, the label and the label size itself will have to be carefully considered.

4.2 Expansion microscopy of pathogens

Within the second part of this thesis it could be demonstrated that expansion microscopy was successfully extended to visualize not only bacterial, but also fungal pathogens. Even more important, we could open a new field of potential target molecules in expansion microscopy by the introduction of an amine into a C_6-ceramide.

First, fourfold expansion microscopy was established to investigate the infection by *C. trachomatis.* We could demonstrate that ExM is applicable to this gram-negative bacterium, although these bacteria possess a complex cell envelope. ExM could also be applied to the closely related pathogen *S. negevensis*, while *N. gonorrhoeae* required an additional treatment with lysozyme for isotropic expansion. This is in conformity with expansion microscopy experiments involving other bacteria like *Salmonella* which also necessitated lysozyme treatment (Lim et al. 2019). Hence, *C. trachomatis* was an ideal first bacterial pathogen to establish ExM. We could also demonstrate a highly important benefit delivered by the fourfold expansion and consequently improved resolution. Upon expansion, single *Chlamydia* were detectable, even with obvious size differences resulting in the hypothesis that these different sized single *Chlamydia* might be infectious EBs and metabolic active RBs. This hypothesis could be confirmed after fourfold expansion of the *Chlamydia* strain *Ct* mCh(GroL2) GFP(OmcAL2), where mCherry was under the control of the RB-associated constitutive *groESL* operon promoter and GFP was controlled by the EB-associated *omc* promoter. Hereby, it could clearly be confirmed that all big RBs expressed mCherry while all small *Chlamydia* expressed GFP. As these size differences are not visible in standard confocal or SIM imaging, ExM paves the way to investigations of the two chlamydial forms at different infection stages under chosen conditions. Moreover, ExM offers the possibility to study the secretion of effector proteins like CPAF in single *Chlamydia*.

After demonstrating the compatibility of fourfold ExM with *C. trachomatis*, we extended the expansion factor and also the applicability of ExM to lipids. Hereby, we successfully synthesized an amino-modified α-NH$_2$-ω-N$_3$-C_6-ceramide which allowed not only the staining *via* a SPAAC-reaction, but also the fixation and consequently also the expansion exploiting this new primary amine. Our new ceramide was strongly incorporated into cell organelles and into the plasma membrane, similarly to the control without amine modification, indicating an unperturbed uptake by the cell. First, we could demonstrate strongly enhanced fixation properties of the amino-modified ceramide compared to the conventional ceramide in FRAP experiments. This was already a big improvement as most lipids do not bear a primary amine making them unfixable. The introduction of this amine enabled an efficient fixation resulting in an only mild signal decrease upon detergent exposure, while the unmodified ceramide was washed out.

We hypothesize that this fixation might also enable SMLM experiments, but this has to be verified in the future.

Next, we successfully tested our compound in fourfold and tenfold ExM which clearly confirmed our hypothesis that a single primary amine enables the incorporation into the hydrogel used in ExM. The exact mechanism how glutaraldehyde can enable both the fixation and expansion with only one primary amine is not entirely clear. Chozinski et al. reason that glutaraldehyde is present in aqueous solutions in an equilibrium between monomeric and polymeric forms which contain aldehyde and alkene groups (Chozinski et al. 2016, Migneault et al. 2004). Both of these groups on glutaraldehyde could be covalently incorporated into the polyacrylamide gel. Other possible mechanisms involve linking of the glutaraldehyde polymer to the gel by entanglement with the polymers (Kim and Park 2004) or even a combination of covalent and entanglement mechanisms. Albeit we cannot clearly quantify how many ceramides are incorporated, these experiments provide first strategies to adapt ExM for any target molecule, even if it does not bear a primary amine. Here, correlative studies using dSTORM might answer these questions, although highly dense targets like ceramides might require several adjustments for successful dSTORM imaging. However, the ceramides localized mostly within the cells' organelles, comparable to non expanded samples in both four- and tenfold ExM, excluding most artifacts. Moreover, we could also expand lipids of the plasma membrane in general for the first time, as mCling labeled with ATTO 643 could efficiently be used in ExM.

We also investigated the highly efficient ceramide uptake during infection by *C. trachomatis* and *S. negevensis* using ExM in combination with SIM providing a lateral resolution of at least 15 nm. This uptake could be inhibited in case of *C. trachomatis* by the CERT specific inhibitor HPA-12, although a potent inhibition could only be demonstrated for ceramide incubations of maximum 15 minutes. This clearly indicates at least one other pathway for ceramide uptake, which is independent of the CERT. A potential pathway could be vesicle trafficking from the Golgi-apparatus (Zeidan and Hannun 2007) which is affirmed by reports involving IncE. These studies hypothesized that IncE could mediate the disruption of retromer trafficking which mediates the vesicle trafficking between endosomes and the trans Golgi-apparatus (Elwell et al. 2017). To address this question, an additional vesicle staining might help to answer this question.

Moreover, also the chlamydial ceramide uptake mediated by CERT is not entirely clear, although it is known that IncD hijackes CERT and therefore colocalizes with CERT at the inclusion membrane. The lipid transfer itself is then mediated by the interaction with vesicles present in the ER and the protein VAPB into the chlamydial inclusion. The exact mechanism of ceramide distribution into single *Chlamydia* resident within the inclusion remains to be investigated. Interestingly, there are speculations that ceramides might be taken up by a T3SS, similarly to the nanotube formation of *E. coli,* to extract nutrients from its host (Pal et al. 2019).

Hereby, the T3SS might act as needle to connect *Chlamydia* present at the inclusion membrane to the host as demonstrated in EM-studies (Nans et al. 2015). Such assumptions are affirmed by frequent observations from us and others that RBs often localize in close vicinity to the inclusion membrane, presumably to gain nutrients (Elwell et al. 2011) and as a part of chlamydial development (Hoare et al. 2008).

As already demonstrated, we could clearly distinguish EBs and RBs by fourfold ExM just by the size of single *Chlamydia* (Kunz et al. 2019). Interestingly, after tenfold expansion, we could detect even more size differences within the chlamydial population. We assume that these other sized *Chlamydia* are intermediate bodies (IM) and *Chlamydia* which are converting from RBs to EBs. This categorization was only recently possible using serial block face scanning microscopy (Lee et al. 2018). As this method is extremely time consuming with an average acquisition time of ~25 hours for each 3D-image and additional post processing, 10x ExM is here again an attractive alternative. Using this method, the complete life cycle after various time points following infection can be investigated with respect to the different developmental forms of *C. trachomatis.* Especially interesting would be the depletion of nutrients and its impact on the ratio of RBs and EBs as the depletion of nutrients normally results in the transition to aberrant, reproductively impaired RBs, similarly to antibiotics treatment (Wyrick 2010).

Here, even two other proteins of interest can be localized to single *Chlamydia* during infection additionally to a *Chlamydia* staining to shed light on the interaction between the host and pathogen. We also applied 10x ExM to study the interaction between *C. trachomatis* and mitochondria. Hereby, we could successfully visualize the mitochondrial reorganization at a resolution only exceeded by electron microscopy. This allowed us to demonstrate direct interactions between mitochondria arranged around the inclusion and the chlamydial inclusion. It is expected that this rearrangement serves *C. trachomatis* to gain nutrients, similarly to the fragmentation of the Golgi-apparatus which is required for spingholipid transport to the inclusion (Saka and Valdivia 2010).

We could even frequently detect the mitochondrial matrix protein Prx3 within single bacteria, which suggests an unspecific protein uptake by *Chlamydia.* Unfortunately, only speculations can be made about the mechanism of this uptake as in the case of the ceramides previously. This detection of mitochondrial proteins seems certainly reasonable because NAD(P)H could already be detected at and within the inclusion (Szaszák et al. 2011).

However, not only the interaction between the host and pathogen can be visualized at a superior resolution, but also the interaction between two pathogens. An interesting model would be a coinfection with *Chlamydia trachomatis* and *Neisseria gonorrhoeae* because these two potentially occur together (Guy et al. 2015). This coinfection is poorly understood, although mathematical models estimate the occurrence of coinfections are too high to be random (Althaus et al. 2014) assuming an active interplay between these pathogens (Leonard et al. 2019).

Finally, we could resolve the inner and outer bacterial membrane and demonstrate a ceramide integration into both membranes making use of the resolution power of 10x ExM-SIM which would barely be possible with any other light microscopy method. This allowed us to determine the mean distance between these membranes to 30 ± 9.2 nm in agreement with data coming from electron microscopy (Asmar et al. 2017). This again raises questions about the exact mechanism of the ceramide transport from the inclusion membrane to single *Chlamydia* and also about the importance of ceramides for *C. trachomatis.*

Moreover, it would be highly interesting to modify other ceramides or even lipids in general with an azide and an amine to investigate if also other lipids are integrated as well into both bacterial membranes.

Furthermore, a factor limiting the function of antibiotics is often their poor penetration of bacterial membranes. As our new compound in combination with ExM enabled the visualization of the bacterial double membrane, ExM could be a highly relevant tool for the development of antibiotics, especially against multidrug-resistant bacteria (Ghai and Ghai 2018). We further assume that not only bacterial infections but possibly viral infections might be investigated using the resolution power of ExM in the near future. Ultimately, it could also be attempted to incubate, possibly even by *C. trachomatis* infected, living tissue in our new ceramide compound. If successful, this would enable the visualization of a bacterial infection under more realistic conditions and to track the ceramide metabolism.

When thinking about the only poorly investigated infection by *S. negevensis* also a lot of open questions remain. Using ExM the developmental cycle could be tracked in more detail after different durations of infection, again with respect to the different developmental forms. It is also known that *S. negevensis* remodels mitochondria and the entire cellular ER, possibly involving inclusion membrane like proteins (sInc) which could establish and control the ER-vacuole sites (Mehlitz et al. 2014). In both cases, ExM would be an ideal tool for further investigations.

Within this work not only the expansion of bacterial, but also of fungal pathogens was established. In this proof of principle study we expanded protoplasts and sporidia of the basidiomycete *U. maydis* and hyphae of the two ascomycetes *F.oxysporum* and *A. fumigatus* by a factor of ~4.5, boosting the resolution to ~60 nm (Chen et al. 2015) and in combination with SIM to estimated even ~30 nm. The most crucial step was hereby the enzymatic degradation of the fungal cell wall using a mixture of driselase, chitinase and lysing enzyme of *T. harzanium*. If this digestion was skipped, or, in case of *F.oxysporum*, a too long germination time was allowed, this resulted in an impeded cell wall digestion and the sample was either not expanded or solely partially. Hence, especially when working with fungi, care has to be taken to avoid artifacts caused by incomplete expansion and the cell wall digestion should be optimized for each new fungus, ideally confirmed by an additional Calcofluor white staining. If the cell wall

digestion is not successful, the incubation temperature, the medium or the germination might need to be adjusted, as these parameters strongly influence the cell wall composition in yeasts (Terpitz et al. 2012) and filamentous fungi (Reilly and Doering 2010, Li et al. 2017). However, under suitable conditions the cell wall was efficiently removed and labeled fungal cytoskeleton, histones, mitochondria, membrane proteins and even the cell membrane itself could be expanded. An important part of our protocol is that the cell wall degradation can be applied to either living cells producing protoplasts or in fixed cells to visualize the naïve fungus. Upon applying SIM to fourfold expanded *F. oxysporum*, even different dense histone regions became apparent and also actin fibres could be better visualized. Also in case of *A. fumigatus* the benefit of ExM was shown by the improved separation of single mitochondria. When working with small fungi like in these experiments, ExM provides a substantial resolution improvement without the need for sophisticated SMLM setups. The importance of the right fluorophore choice was also obvious in the case of mRFP expressed by *A. fumigatus*, as RFP suffers strongly from the digestion step making only short proteinase K incubations necessary. To improve this signal, other more stable fluorescent proteins like mCherry or tdTomato could be used (Tillberg et al. 2016) which would be even more crucial when thinking about tenfold expansion of fungi. Although in principle possible, fungi always exhibited relatively weak fluorescence signals making a 1000-fold signal dilution more challenging for image acquisition. Thus, similarly to the receptor expansion part, signal amplification might solve this issue. The interactions between *A. fumigatus* and natural killer cells could be investigated more in detail in the future. Activated NK-cells release granzymes and perforin to damage the hyphae. Involved in this activation is CD56 which was demonstrated to accumulate at the interaction site in dependence of actin (Ziegler et al. 2017). As blocking of CD56 did not fully inhibit NK-cell activation, this suggests that also other molecules might be involved in NK-cell activation by *A. fumigatus*. Due to the highly three-dimensional nature of these interaction sides, both fourfold and tenfold ExM with its high lateral and also high axial resolution might be suitable methods to further study these interactions.

Although the applicability of ExM could be extended within this thesis, many problems concerning ExM still need to be addressed. One of the most limiting steps is the dye loss during proteinase K digestion which is caused by cutting out dyes conjugated to antibodies. Here, not only the digestions times can be minimized according to the target structure, but also labels resistant to such digestions or milder proteinases could improve this issue. Other, ultimately resolution limiting problems are the unknown density and possible nanoscale heterogeneity within the hydrogel mesh caused by the radical polymerization (Orakdogen and Okay 2006, Di Lorenzo and Seiffert 2015). Hence, Gao et al. (Gao et al. 2019) recently introduced a "tetragel" composed of tetra polyethylene glycol monomers which was shown to form a diamond lattice like meshwork with high structural homogeneity (Sakai et al. 2008). The gel is then

formed by a click chemistry based and not radical involving linking of two complementary tetrahedral monomers. Similarly to the proExM protocol (Tillberg et al. 2016), a NHS-reaction is used as sample linker, albeit here the compound NHS-azide is applied instead of NHS-AcX which reacts with the alkynes of the tetrahedral monomers. Tetragels result in optically transparent gels with possible expansion factors of 3.0 - 3.5 and in combination with iterative ExM expansion factors of ~10 are possible. Another crucial advantage of this approach is the avoidance of a radical reaction making the use of cyanines like Alexa Fluor 647 possible which might facilitate the combination with *d*STORM in the future. In this study, the improved homogeneity of the expanded gels could be demonstrated by a significantly decreased deviation from the circular shape of the herpes simplex virus type 1 (Gao et al. 2019). One other possibility to introduce Alexa Fluor 647 or to label structures in general could be a post-expansion labeling procedure according to the MAP (Ku et al. 2016) or U-ExM protocol (Gambarotto et al. 2019). In these protocols the sample is embedded into the hydrogel, the proteins are denatured by SDS and boiled followed by an immunostaining. This procedure results in a smaller linkage error due to the post-expansion labeling compared to other ExM protocols and a reduced dye loss during gelation and digestion. Moreover, even new epitopes might get accessible due to the denaturation step (Gambarotto et al. 2019). However, not all antibodies will recognize denatured epitopes and it could not be shown yet that denaturation is sufficient for higher expansion factors than four.

Of course, after the development of ExM from a fourfold to a ten- and even twentyfold expansion, even higher expansion factors will follow. The most straight forward approach would probably be the combination of 10x ExM with iterative ExM. Even if a 10x monomer solution with the additional crosslinker N,N′-(1,2-dihydroxyethylene) bisacrylamide (DHEBA) would not be compatible, at least the second monomer solution in iterative ExM could be replaced by a 10x monomer solution resulting in an expansion factor of ~45 and a potential resolution of ~5 nm. Again, the combination with SIM could push the resolution even further, close to MINFLUX (Balzarotti et al. 2017) with a resolution of few nanometers or electron microscopy. After applying such expansion factors, not only dimers like CD69, as described in the previous section, but also ringforming protein complexes like the mitochondrial inner membrane proteins prohibitin 1 and 2 with a diameter of 20 - 25 nm (Merkwirth and Langer 2009) or alternating α- and β-tubulin monomers with a distance of ~6 - 8 nm (Kalra et al. 2019, Kononova et al. 2014) could be resolvable.

As already discussed, at high expansion factors alternatives for the big immunolabeling with 17.5 nm (Chang et al. 2017) and a resulting linkage error of 175 nm after tenfold expansion will be indispensable. Hence, our newly introduced α-NH_2-ω-N_3-C_6-ceramide is also attractive for ExM due to the negligible linkage error cause by the DBCO-azide SPAAC-reaction.

With increasing expansion factors of course also the size of the gel itself is drastically increasing. Already at an expansion factor of ten a conventional U2OS cell will grow to a size of 200 µm which already is problematic to image due to the imageable region limited by the chip size of the detector. With an increasing region of interest also the imaging duration drastically increases in ExM, especially in whole cell imaging. A possible solution for this issue could be the use of a LLS which would accelerate the imaging and also decrease photodamage. However, also here the sample size will ultimately be a limiting factor when thinking of tissue or whole organs.

Hence, an important consideration for each ExM experiment has to be the required resolution to avoid unnecessary, time consuming imaging of huge regions of interest. Recently, a method termed ZOOM (Park et al. 2019) was introduced to tune the expansion factor according to the needs of the experiment and to balance the required expansion and the necessary time for imaging. Hereby, the sample is embedded into an electrically neutral gel and then primary amides are hydrolyzed at 80°C to ionic carboxylates. This hydrolysis controls the amount of negative charges and the achievable expansion factor from two to maximal eight. ZOOM was demonstrated to be applicable to cell lines, bacteria and even human samples from a Parkinson's disease patient making ZOOM a highly versatile and tunable expansion microscopy method.

Overall, this thesis provides several advancements within the field of super-resolved quantitative single and multi-color imaging as well as whole cell imaging. The quantitative approaches were successfully applied to three clinically relevant projects and the superior sensitivity of *d*STORM compared to flow cytometry was confirmed for a second antigen, CD20. Hopefully, more ultra-low expressed antigens can be identified to improve immunotherapy in the future.

Additionally, ExM was established for the investigation of bacterial and fungal infections. Both will be of huge interest to these fields, as this enables the detailed tracking of distinct developmental forms of bacteria and introduces super-resolution imaging to a wider audience. Lastly, we could also extend the possible target molecules for ExM by the introduction of a primary amine into a C_6-ceramide. Furthermore, this amine also enables an efficient ceramide fixation, making other SMLM methods feasible.

List of publications

Super-resolution microscopy reveals ultra-low CD19 expression on myeloma cells that triggers elimination by CD19 CAR-T

Thomas Nerreter, Sebastian Letschert, Ralph Götz, Sophia Danhof, Sören Doose, Hermann Einsele, Markus Sauer & Michael Hudecek

Nat Commun **10**, 3137 (2019), https://doi.org/10.1038/s41467-019-10948-w

Detection of *Chlamydia* Developmental Forms and Secreted Effectors by Expansion Microscopy

Tobias C. Kunz* & Ralph Götz*, Markus Sauer & Thomas Rudel

*Contributed equally

Front Cell Infect Microbiol **9**, 276 (2019), https://doi.org/10.3389/fcimb.2019.00276

Whole-cell imaging of plasma membrane receptors by 3D lattice light-sheet *d*STORM

Felix Wäldchen, Jan Schlegel, Ralph Götz, Sören Doose & Markus Sauer

Nat Commun **11,** 887 (2020), https://doi.org/10.1038/s41467-020-14731-0

Expansion microscopy for cell biology analysis in fungi

Ralph Götz, Sabine Panzer, Nora Trinks, Janna Eilts, Johannes Wagener, David Turrà, Antonio Di Pietro, Markus Sauer & Ulrich Terpitz

Front. Microbiol. **11**, 574 (2020), https://doi.org/10.3389/fmicb.2020.00574

Nanoscale imaging of cellular and bacterial membranes by sphingolipid expansion microscopy

Ralph Götz*, Tobias C. Kunz*, Julian Fink, Franziska Solger, Jan Schlegel, Jürgen Seibel, Vera Kozjak-Pavlovic, Thomas Rudel & Markus Sauer

*Contributed equally

In revision at *ACS nano*

Upregulation of CD38 Expression on Multiple Myeloma Cells by Novel HDAC6 Inhibitors is a Class Effect and Augments the Efficacy of Daratumumab

Estefanía García-Guerrero, Ralph Götz, Sören Doose, Markus Sauer, Alfonso Rodriguez-Gil, Thomas Nerreter, Martin Kortüm, José A. Pérez-Simón, Hermann Einsele, Michael Hudecek & Sophia Danhof

In revision at *Leukemia*

Quantification of membrane receptors by super-resolution microscopy

Ralph Götz, Patrick Eiring, Thomas Nerreter, Felix Wäldchen, Alexander Kuhlemann, Hermann Einsele, Michael Hudecek, Sören Doose & Markus Sauer

In preparation

Enhancing the efficacy of chimeric antigen receptors (CARs) against BCMA by combinatorial treatment with ATRA

Estefanía García-Guerrero, Sophia Danhof, Tea Gogishvili, Ralph Götz, Markus Sauer, Thomas Nerreter, Jose Antonio Pérez-Simón, Hermann Einsele, Michael Hudecek & Sabrina Prommersberger

In preparation

Further publications

Cyanine Conformational Restraint in the Far-Red Range

Megan S. Michie, Ralph Götz, Christian Franke, Matthew Bowler, Nikita Kumari, Valentin Magidson, Marcia Levitus, Jadranka Loncarek, Markus Sauer & Martin J. Schnermann

J Am Chem Soc **139**, 12406-12409 (2017), https://doi.org/10.1021/jacs.7b07272

Sharpening emitter localization in front of a tuned mirror

Hannah S. Heil, Benjamin Schreiber, Ralph Götz, Monika Emmerling, Marie-Christine Dabauvalle, Georg Krohne, Sven Höfling, Martin Kamp, Markus Sauer & Katrin G. Heinze

Light: Science & Applications **7**, 99 (2018), https://doi.org/10.1038/s41377-018-0104-z

Analysis of the putative tumor suppressor gene cdkn2ab in pigment cells and melanoma of Xiphophorus and medaka

Janine Regneri, Barbara Klotz, Brigitta Wilde, Verena A. Kottler, Michael Hausmann, Susanne Kneitz Martina Regensburger, Katja Maurus, Ralph Götz, Yuan Lu, Ronald B. Walter, Amaury Herpin & Manfred Schartl

Pigment Cell Melanoma Res **32**, 248-258 (2019), https://doi.org/10.1111/pcmr.12729

Far-red cyanine dye Cy5B for single-molecule localization microscopy

Ralph Götz, Dominic Helmerich, Christian Werner, Sören Doose, Martin Schnermann & Markus Sauer

In preparation

Bibliography

Aandahl, E. M., J. K. Sandberg, K. P. Beckerman, K. Tasken, W. J. Moretto & D. F. Nixon (2003) CD7 is a differentiation marker that identifies multiple CD8 T cell effector subsets. *J Immunol,* 170**,** 2349-55.

Abbe, E. (1873) Beiträge zur Theorie des Mikroskops und der mikroskopischen Wahrnehmung. *Archiv für Mikroskopische Anatomie,* 9**,** 413-468.

Abdel Hameed, A. A., I. H. Yasser & I. M. Khoder (2004) Indoor air quality during renovation actions: a case study. *J Environ Monit,* 6**,** 740-4.

Agaisse, H. & I. Derre (2014) Expression of the effector protein IncD in Chlamydia trachomatis mediates recruitment of the lipid transfer protein CERT and the endoplasmic reticulum-resident protein VAPB to the inclusion membrane. *Infect Immun,* 82**,** 2037-47.

Agaisse, H. & I. Derré (2015) STIM1 Is a Novel Component of ER-Chlamydia trachomatis Inclusion Membrane Contact Sites. *PLOS ONE,* 10**,** e0125671.

Agard, N. J., J. M. Baskin, J. A. Prescher, A. Lo & C. R. Bertozzi (2006) A comparative study of bioorthogonal reactions with azides. *ACS Chem Biol,* 1**,** 644-8.

Aggarwal, C., Reddy, C. (2014) Data Clustering. *Chapman and Hall/CRC.*

Al-Zeer, M. A., H. M. Al-Younes, M. Kerr, M. Abu-Lubad, E. Gonzalez, V. Brinkmann & T. F. Meyer (2014) Chlamydia trachomatis remodels stable microtubules to coordinate Golgi stack recruitment to the chlamydial inclusion surface. *Mol Microbiol,* 94**,** 1285-97.

Ali, S. A., V. Shi, I. Maric, M. Wang, D. F. Stroncek, J. J. Rose, J. N. Brudno, M. Stetler-Stevenson, S. A. Feldman, B. G. Hansen, V. S. Fellowes, F. T. Hakim, R. E. Gress & J. N. Kochenderfer (2016) T cells expressing an anti-B-cell maturation antigen chimeric antigen receptor cause remissions of multiple myeloma. *Blood,* 128**,** 1688-700.

Althaus, C. L., K. M. Turner, C. H. Mercer, P. Auguste, T. E. Roberts, G. Bell, S. A. Herzog, J. A. Cassell, W. J. Edmunds, P. J. White, H. Ward & N. Low (2014) Effectiveness and cost-effectiveness of traditional and new partner notification technologies for curable sexually transmitted infections: observational study, systematic reviews and mathematical modelling. *Health Technol Assess,* 18**,** 1-100, vii-viii.

Anderson, F. B. & J. W. Millbank (1966) Protoplast formation and yeast cell-wall structure. The action of the enzymes of the snail, Helix pomatia. *The Biochemical journal,* 99**,** 682-687.

Andreska, T., S. Aufmkolk, M. Sauer & R. Blum (2014) High abundance of BDNF within glutamatergic presynapses of cultured hippocampal neurons. *Front Cell Neurosci,* 8**,** 107.

Asmar, A. T., J. L. Ferreira, E. J. Cohen, S. H. Cho, M. Beeby, K. T. Hughes & J. F. Collet (2017) Communication across the bacterial cell envelope depends on the size of the periplasm. *PLoS Biol,* 15**,** e2004303.

Atanackovic, D., J. Panse, Y. Hildebrandt, A. Jadczak, S. Kobold, Y. Cao, J. Templin, S. Meyer, H. Reinhard, K. Bartels, N. Lajmi, A. R. Zander, A. H. Marx, C. Bokemeyer & N. Kröger (2011) Surface molecule CD229 as a novel target for the diagnosis and treatment of multiple myeloma. *Haematologica,* 96**,** 1512.

Axup, J. Y., K. M. Bajjuri, M. Ritland, B. M. Hutchins, C. H. Kim, S. A. Kazane, R. Halder, J. S. Forsyth, A. F. Santidrian, K. Stafin, Y. Lu, H. Tran, A. J. Seller, S. L. Biroc, A. Szydlik, J. K. Pinkstaff, F. Tian, S. C. Sinha, B. Felding-Habermann, V. V. Smider & P. G. Schultz (2012) Synthesis of site-specific antibody-drug conjugates using unnatural amino acids. *Proceedings of the National Academy of Sciences of the United States of America,* 109**,** 16101-16106.

Balmer, J. E. & R. Blomhoff (2002) Gene expression regulation by retinoic acid. *J Lipid Res,* 43**,** 1773-808.

Balzarotti, F., Y. Eilers, K. C. Gwosch, A. H. Gynnå, V. Westphal, F. D. Stefani, J. Elf & S. W. Hell (2017) Nanometer resolution imaging and tracking of fluorescent molecules with minimal photon fluxes. *Science,* 355**,** 606-612.

Bamberger, M., A. M. Santos, C. M. Goncalves, M. I. Oliveira, J. R. James, A. Moreira, F. Lozano, S. J. Davis & A. M. Carmo (2011) A new pathway of CD5 glycoprotein-mediated T cell inhibition dependent on inhibitory phosphorylation of Fyn kinase. *J Biol Chem,* 286**,** 30324-36.

Banaszek, A., T. G. P. Bumm, B. Nowotny, M. Geis, K. Jacob, M. Wolfl, J. Trebing, K. Kucka, D. Kouhestani, T. Gogishvili, B. Krenz, J. Lutz, L. Rasche, D. Honemann, H. Neuweiler, J. C. Heiby, R. C. Bargou, H. Wajant, H. Einsele, G. Riethmuller & G. Stuhler (2019) On-target restoration of a split T cell-engaging antibody for precision immunotherapy. *Nat Commun,* 10**,** 5387.

Baskin, J. M., J. A. Prescher, S. T. Laughlin, N. J. Agard, P. V. Chang, I. A. Miller, A. Lo, J. A. Codelli & C. R. Bertozzi (2007) Copper-free click chemistry for dynamic in vivo imaging. *Proc Natl Acad Sci U S A,* 104**,** 16793-7.

Bastidas, R. J., C. A. Elwell, J. N. Engel & R. H. Valdivia (2013) Chlamydial intracellular survival strategies. *Cold Spring Harb Perspect Med,* 3**,** a010256.

Baumgart, F., A. M. Arnold, K. Leskovar, K. Staszek, M. Folser, J. Weghuber, H. Stockinger & G. J. Schutz (2016) Varying label density allows artifact-free analysis of membrane-protein nanoclusters. *Nat Methods,* 13**,** 661-4.

Bausch-Fluck, D., A. Hofmann, T. Bock, A. P. Frei, F. Cerciello, A. Jacobs, H. Moest, U. Omasits, R. L. Gundry, C. Yoon, R. Schiess, A. Schmidt, P. Mirkowska, A. Hartlova, J. E. Van Eyk, J. P. Bourquin, R. Aebersold, K. R. Boheler, P. Zandstra & B. Wollscheid (2015) A mass spectrometric-derived cell surface protein atlas. *PLoS One,* 10**,** e0121314.

Beliu, G., A. J. Kurz, A. C. Kuhlemann, L. Behringer-Pliess, M. Meub, N. Wolf, J. Seibel, Z. D. Shi, M. Schnermann, J. B. Grimm, L. D. Lavis, S. Doose & M. Sauer (2019) Bioorthogonal labeling with tetrazine-dyes for super-resolution microscopy. *Commun Biol,* 2**,** 261.

Belland, R., D. M. Ojcius & G. I. Byrne (2004) Chlamydia. *Nat Rev Microbiol,* 2**,** 530-1.

Belland, R. J., G. Zhong, D. D. Crane, D. Hogan, D. Sturdevant, J. Sharma, W. L. Beatty & H. D. Caldwell (2003) Genomic transcriptional profiling of the developmental cycle of Chlamydia trachomatis. *Proc Natl Acad Sci U S A,* 100**,** 8478-83.

Betzig, E., G. H. Patterson, R. Sougrat, O. W. Lindwasser, S. Olenych, J. S. Bonifacino, M. W. Davidson, J. Lippincott-Schwartz & H. F. Hess (2006) Imaging intracellular fluorescent proteins at nanometer resolution. *Science,* 313**,** 1642-5.

Blair, H. A. (2017) Daratumumab: A Review in Relapsed and/or Refractory Multiple Myeloma. *Drugs,* 77**,** 2013-2024.

Blom, H. & H. Brismar (2014) STED microscopy: increased resolution for medical research? *J Intern Med,* 276**,** 560-78.

Bose, T. O., Q. M. Pham, E. R. Jellison, J. Mouries, C. M. Ballantyne & L. Lefrancois (2013) CD11a regulates effector CD8 T cell differentiation and central memory development in response to infection with Listeria monocytogenes. *Infect Immun,* 81**,** 1140-51.

Brown, G. D., D. W. Denning, N. A. Gow, S. M. Levitz, M. G. Netea & T. C. White (2012) Hidden killers: human fungal infections. *Sci Transl Med,* 4**,** 165rv13.

Burgert, A., S. Letschert, S. Doose & M. Sauer (2015) Artifacts in single-molecule localization microscopy. *Histochem Cell Biol,* 144**,** 123-31.

Burgert, A., J. Schlegel, J. Becam, S. Doose, E. Bieberich, A. Schubert-Unkmeir & M. Sauer (2017) Characterization of Plasma Membrane Ceramides by Super-Resolution Microscopy. *Angew Chem Int Ed Engl,* 56**,** 6131-6135.

Chang, J. B., F. Chen, Y. G. Yoon, E. E. Jung, H. Babcock, J. S. Kang, S. Asano, H. J. Suk, N. Pak, P. W. Tillberg, A. T. Wassie, D. Cai & E. S. Boyden (2017) Iterative expansion microscopy. *Nat Methods,* 14**,** 593-599.

Chapuis, F. A., R. E. Ballou & M. D. MacCallum (2019) A Bright Future for Fluorescence Imaging of Fungi in Living Hosts. *Journal of Fungi,* 5.

Chen, B. C., W. R. Legant, K. Wang, L. Shao, D. E. Milkie, M. W. Davidson, C. Janetopoulos, X. S. Wu, J. A. Hammer, 3rd, Z. Liu, B. P. English, Y. Mimori-Kiyosue, D. P. Romero, A. T. Ritter, J. Lippincott-Schwartz, L. Fritz-Laylin, R. D. Mullins, D. M. Mitchell, J. N. Bembenek, A. C. Reymann, R. Bohme, S. W. Grill, J. T. Wang, G. Seydoux, U. S. Tulu, D. P. Kiehart & E. Betzig (2014) Lattice light-sheet microscopy: imaging molecules to embryos at high spatiotemporal resolution. *Science,* 346**,** 1257998.

Chen, F., P. W. Tillberg & E. S. Boyden (2015) Optical imaging. Expansion microscopy. *Science,* 347**,** 543-8.

Chen, F., A. T. Wassie, A. J. Cote, A. Sinha, S. Alon, S. Asano, E. R. Daugharthy, J. B. Chang, A. Marblestone, G. M. Church, A. Raj & E. S. Boyden (2016) Nanoscale imaging of RNA with expansion microscopy. *Nat Methods,* 13**,** 679-84.

Chozinski, T. J., A. R. Halpern, H. Okawa, H. J. Kim, G. J. Tremel, R. O. Wong & J. C. Vaughan (2016) Expansion microscopy with conventional antibodies and fluorescent proteins. *Nat Methods,* 13**,** 485-8.

Chu, J., Y. Deng, D. M. Benson, S. He, T. Hughes, J. Zhang, Y. Peng, H. Mao, L. Yi, K. Ghoshal, X. He, S. M. Devine, X. Zhang, M. A. Caligiuri, C. C. Hofmeister & J. Yu (2014) CS1-specific chimeric antigen receptor (CAR)-engineered natural killer cells enhance in vitro and in vivo antitumor activity against human multiple myeloma. *Leukemia,* 28**,** 917-927.

Chung, K., J. Wallace, S. Y. Kim, S. Kalyanasundaram, A. S. Andalman, T. J. Davidson, J. J. Mirzabekov, K. A. Zalocusky, J. Mattis, A. K. Denisin, S. Pak, H. Bernstein, C. Ramakrishnan, L. Grosenick, V. Gradinaru & K. Deisseroth (2013) Structural and molecular interrogation of intact biological systems. *Nature,* 497**,** 332-7.

Cole, N. B. (2013) Site-specific protein labeling with SNAP-tags. *Current protocols in protein science,* 73**,** 30.1.1-30.1.16.

Cortina, M. E., R. J. Ende, R. C. Bishop, C. Bayne & I. Derre (2019) Chlamydia trachomatis and Chlamydia muridarum spectinomycin resistant vectors and a transcriptional fluorescent reporter to monitor conversion from replicative to infectious bacteria. *PLoS One,* 14**,** e0217753.

Cui, X., L. Chang, Y. Li, Q. Lv, F. Wang, Y. Lin, W. Li, J. D. Meade, J. C. Walden & P. Liang (2018) Trivalent soluble TNF Receptor, a potent TNF-α antagonist for the treatment collagen-induced arthritis. *Scientific Reports,* 8**,** 7327.

de Bekker, C., A. Wiebenga, G. Aguilar & H. A. Wosten (2009) An enzyme cocktail for efficient protoplast formation in Aspergillus niger. *J Microbiol Methods,* 76**,** 305-6.

Debets, M. F., S. S. van Berkel, S. Schoffelen, F. P. Rutjes, J. C. van Hest & F. L. van Delft (2010) Aza-dibenzocyclooctynes for fast and efficient enzyme PEGylation via copper-free (3+2) cycloaddition. *Chem Commun (Camb),* 46**,** 97-9.

Dempsey, G. T., J. C. Vaughan, K. H. Chen, M. Bates & X. Zhuang (2011) Evaluation of fluorophores for optimal performance in localization-based super-resolution imaging. *Nat Methods,* 8**,** 1027-36.

Derré, I. (2015) Chlamydiae interaction with the endoplasmic reticulum: contact, function and consequences. *Cellular Microbiology,* 17**,** 959-966.

Derre, I., R. Swiss & H. Agaisse (2011) The lipid transfer protein CERT interacts with the Chlamydia inclusion protein IncD and participates to ER-Chlamydia inclusion membrane contact sites. *PLoS Pathog,* 7**,** e1002092.

Di Lorenzo, F. & S. Seiffert (2015) Nanostructural heterogeneity in polymer networks and gels. *Polymer Chemistry,* 6**,** 5515-5528.

Dimopoulos, M. A., A. Oriol, H. Nahi, J. San-Miguel, N. J. Bahlis, S. Z. Usmani, N. Rabin, R. Z. Orlowski, M. Komarnicki, K. Suzuki, T. Plesner, S. S. Yoon, D. Ben Yehuda, P. G. Richardson, H. Goldschmidt, D. Reece, S. Lisby, N. Z. Khokhar, L. O'Rourke, C. Chiu, X. Qin, M. Guckert, T. Ahmadi, P. Moreau & P. Investigators (2016) Daratumumab, Lenalidomide, and Dexamethasone for Multiple Myeloma. *N Engl J Med,* 375**,** 1319-1331.

Dita, M., M. Barquero, D. Heck, E. S. G. Mizubuti & C. P. Staver (2018) Fusarium Wilt of Banana: Current Knowledge on Epidemiology and Research Needs Toward Sustainable Disease Management. *Front Plant Sci,* 9**,** 1468.

Du, H., P. Hou, W. Zhang & Q. Li (2018) Advances in CLARITY-based tissue clearing and imaging. *Exp Ther Med,* 16**,** 1567-1576.

Duan, X., F. Yang, E. Antono, W. Yang, P. Pianetta, S. Ermon, A. Mehta & Y. Liu (2016) Unsupervised Data Mining in nanoscale X-ray Spectro-Microscopic Study of NdFeB Magnet. *Scientific Reports,* 6**,** 34406.

Elwell, C. A., N. Czudnochowski, J. von Dollen, J. R. Johnson, R. Nakagawa, K. Mirrashidi, N. J. Krogan, J. N. Engel & O. S. Rosenberg (2017) Chlamydia interfere with an interaction between the mannose-6-phosphate receptor and sorting nexins to counteract host restriction. *eLife,* 6**,** e22709.

Elwell, C. A., S. Jiang, J. H. Kim, A. Lee, T. Wittmann, K. Hanada, P. Melancon & J. N. Engel (2011) Chlamydia trachomatis co-opts GBF1 and CERT to acquire host sphingomyelin for distinct roles during intracellular development. *PLoS Pathog,* 7**,** e1002198.

Erwig, L. P. & N. A. R. Gow (2016) Interactions of fungal pathogens with phagocytes. *Nature Reviews Microbiology,* 14**,** 163-176.

Ester, M., H.-P. Kriegel, J. Sander & X. Xu. 1996. A density-based algorithm for discovering clusters a density-based algorithm for discovering clusters in large spatial databases with noise. In *Proceedings of the Second International Conference on Knowledge Discovery and Data Mining*, 226–231. Portland, Oregon: AAAI Press.

Everett, K. D. E., R. M. Bush & A. A. Andersen (1999) Emended description of the order Chlamydiales, proposal of Parachlamydiaceae fam. nov. and Simkaniaceae fam. nov., each containing one monotypic genus, revised taxonomy of the family Chlamydiaceae, including a new genus and five new species, and standards for the identification of organisms. *International Journal of Systematic and Evolutionary Microbiology,* 49**,** 415-440.

Falk, T., D. Mai, R. Bensch, Ö. Çiçek, A. Abdulkadir, Y. Marrakchi, A. Böhm, J. Deubner, Z. Jäckel, K. Seiwald, A. Dovzhenko, O. Tietz, C. Dal Bosco, S. Walsh, D. Saltukoglu, T. L. Tay, M. Prinz, K. Palme, M. Simons, I. Diester, T. Brox & O. Ronneberger (2019) U-Net: deep learning for cell counting, detection, and morphometry. *Nature Methods,* 16**,** 67-70.

Feins, S., W. Kong, E. F. Williams, M. C. Milone & J. A. Fraietta (2019) An introduction to chimeric antigen receptor (CAR) T-cell immunotherapy for human cancer. *American Journal of Hematology,* 94**,** S3-S9.

Fesnak, A. D., C. H. June & B. L. Levine (2016) Engineered T cells: the promise and challenges of cancer immunotherapy. *Nat Rev Cancer,* 16**,** 566-81.

Fischer, A., K. S. Harrison, Y. Ramirez, D. Auer, S. R. Chowdhury, B. K. Prusty, F. Sauer, Z. Dimond, C. Kisker, P. S. Hefty & T. Rudel (2017) Chlamydia trachomatis-containing vacuole serves as deubiquitination platform to stabilize Mcl-1 and to interfere with host defense. *Elife,* 6.

Fournier, M., M. Peyrou, L. Bourgoin, C. Maeder, I. Tchou & M. Foti (2010) CD4 dimerization requires two cysteines in the cytoplasmic domain of the molecule and occurs in microdomains distinct from lipid rafts. *Mol Immunol,* 47**,** 2594-603.

Frankel, S. R. & P. A. Baeuerle (2013) Targeting T cells to tumor cells using bispecific antibodies. *Current Opinion in Chemical Biology,* 17**,** 385-392.

Friedman, M. G., B. Dvoskin & S. Kahane (2003) Infections with the chlamydia-like microorganism Simkania negevensis, a possible emerging pathogen. *Microbes Infect,* 5**,** 1013-21.

Gambarotto, D., F. U. Zwettler, M. Le Guennec, M. Schmidt-Cernohorska, D. Fortun, S. Borgers, J. Heine, J. G. Schloetel, M. Reuss, M. Unser, E. S. Boyden, M. Sauer, V. Hamel & P. Guichard (2019) Imaging cellular ultrastructures using expansion microscopy (U-ExM). *Nat Methods,* 16**,** 71-74.

Gao, M., R. Maraspini, O. Beutel, A. Zehtabian, B. Eickholt, A. Honigmann & H. Ewers (2018) Expansion Stimulated Emission Depletion Microscopy (ExSTED). *ACS Nano,* 12**,** 4178-4185.

Gao, R., C.-C. Yu, L. Gao, K. D. Piatkevich, R. L. Neve, S. Upadhyayula & E. S. Boyden (2019) A highly homogeneous expansion microscopy polymer composed of tetrahedron-like monomers. *bioRxiv***,** 814111.

Garcia-Guerrero, E., T. Gogishvili, S. Danhof, M. Schreder, C. Pallaud, J. A. Perez-Simon, H. Einsele & M. Hudecek (2017) Panobinostat induces CD38 upregulation and augments the antimyeloma efficacy of daratumumab. *Blood,* 129, 3386-3388.

García-Guerrero, E., R. Götz, S. Doose, M. Sauer, A. Rodriguez-Gil, T. Nerreter, M. K. Kortuem, J. Pérez-Simón, H. Einsele & M. Hudecek (2020) Upregulation of CD38 Expression on Multiple Myeloma Cells by Novel HDAC6 Inhibitors is a Class Effect and Augments the Efficacy of Daratumumab. *Leukemia,* In Revision.

Garcia-Martinez, J., M. Brunk, J. Avalos & U. Terpitz (2015) The CarO rhodopsin of the fungus Fusarium fujikuroi is a light-driven proton pump that retards spore germination. *Sci Rep,* 5**,** 7798.

Garcia-Parajo, M. F., A. Cambi, J. A. Torreno-Pina, N. Thompson & K. Jacobson (2014) Nanoclustering as a dominant feature of plasma membrane organization. *J Cell Sci,* 127**,** 4995-5005.

Garfall, A. L., M. V. Maus, W. T. Hwang, S. F. Lacey, Y. D. Mahnke, J. J. Melenhorst, Z. Zheng, D. T. Vogl, A. D. Cohen, B. M. Weiss, K. Dengel, N. D. Kerr, A. Bagg, B. L. Levine, C. H. June & E. A. Stadtmauer (2015) Chimeric Antigen Receptor T Cells against CD19 for Multiple Myeloma. *N Engl J Med,* 373**,** 1040-7.

Geng, X., R. H. Tang, S. K. Law & S. M. Tan (2005) Integrin CD11a cytoplasmic tail interacts with the CD45 membrane-proximal protein tyrosine phosphatase domain 1. *Immunology,* 115**,** 347-57.

Ghai, I. & S. Ghai (2018) Understanding antibiotic resistance via outer membrane permeability. *Infect Drug Resist,* 11**,** 523-530.

Giuliani, N. & F. Malavasi (2019) Editorial: Immunotherapy in Multiple Myeloma. *Frontiers in immunology,* 10**,** 1945-1945.

Gordon, T. R. (2017) Fusarium oxysporum and the Fusarium Wilt Syndrome. *Annu Rev Phytopathol,* 55**,** 23-39.

Götz, R., T. C. Kunz, J. Fink, F. Solger, J. Schlegel, J. Seibel, V. Kozjak-Pavlovic, T. Rudel & M. Sauer (2020a) Nanoscale imaging of cellular and bacterial membranes by sphingolipid expansion microscopy *ACS Nano,* In Revision.

Götz, R., S. Panzer, N. Trinks, J. Eilts, J. Wagener, D. Turrà, A. D. Pietro, M. Sauer & U. Terpitz (2020b) Expansion Microscopy for Cell Biology Analysis in Fungi. *Front. Microbiol. ,* 11**,** 574.

Gow, N. A. R., J. P. Latge & C. A. Munro (2017) The Fungal Cell Wall: Structure, Biosynthesis, and Function. *Microbiol Spectr,* 5.

Grieshaber, N. A., J. B. Sager, C. A. Dooley, S. F. Hayes & T. Hackstadt (2006) Regulation of the Chlamydia trachomatis histone H1-like protein Hc2 is IspE dependent and IhtA independent. *J Bacteriol,* 188**,** 5289-92.

Grimm, J. B., T. Klein, B. G. Kopek, G. Shtengel, H. F. Hess, M. Sauer & L. D. Lavis (2016) Synthesis of a Far-Red Photoactivatable Silicon-Containing Rhodamine for Super-Resolution Microscopy. *Angew Chem Int Ed Engl,* 55**,** 1723-7.

Gustafsson, M. G. (2000) Surpassing the lateral resolution limit by a factor of two using structured illumination microscopy. *J Microsc,* 198**,** 82-7.

Guy, R., J. Ward, H. Wand, A. Rumbold, L. Garton, B. Hengel, B. Silver, D. Taylor-Thomson, J. Knox, S. McGregor, A. Dyda, C. Fairley, L. Maher, B. Donovan, J. Kaldor & S. I. Group (2015) Coinfection with Chlamydia trachomatis, Neisseria gonorrhoeae and Trichomonas vaginalis: a cross-sectional analysis of positivity and risk factors in remote Australian Aboriginal communities. *Sex Transm Infect,* 91**,** 201-6.

Hackstadt, T., D. D. Rockey, R. A. Heinzen & M. A. Scidmore (1996) Chlamydia trachomatis interrupts an exocytic pathway to acquire endogenously synthesized sphingomyelin in transit from the Golgi apparatus to the plasma membrane. *EMBO J,* 15**,** 964-77.

Hammerschlag, M. R. (2004) Chlamydia trachomatis and Chlamydia pneumoniae infections in children and adolescents. *Pediatr Rev,* 25**,** 43-51.

Hang, H. C., C. Yu, D. L. Kato & C. R. Bertozzi (2003) A metabolic labeling approach toward proteomic analysis of mucin-type O-linked glycosylation. *Proc Natl Acad Sci U S A,* 100**,** 14846-51.

Hannun, Y. A. & L. M. Obeid (2018) Sphingolipids and their metabolism in physiology and disease. *Nat Rev Mol Cell Biol,* 19**,** 175-191.

Hansel, T. T., H. Kropshofer, T. Singer, J. A. Mitchell & A. J. George (2010) The safety and side effects of monoclonal antibodies. *Nat Rev Drug Discov,* 9**,** 325-38.

Heilemann, M., S. van de Linde, M. Schuttpelz, R. Kasper, B. Seefeldt, A. Mukherjee, P. Tinnefeld & M. Sauer (2008) Subdiffraction-resolution fluorescence imaging with conventional fluorescent probes. *Angew Chem Int Ed Engl,* 47**,** 6172-6.

Heintzmann, R. & T. Huser (2017) Super-Resolution Structured Illumination Microscopy. *Chem Rev,* 117**,** 13890-13908.

Hell, S. W. (2007) Far-field optical nanoscopy. *Science,* 316**,** 1153-8.

Heller, J. P., T. Odii, K. Zheng & D. A. Rusakov (2019) Imaging tripartite synapses using super-resolution microscopy. *Methods.*

Herweg, J. A., V. Pons, D. Becher, M. Hecker, G. Krohne, J. Barbier, H. Berger, T. Rudel & A. Mehlitz (2016) Proteomic analysis of the Simkania-containing vacuole: the central role of retrograde transport. *Mol Microbiol,* 99**,** 151-71.

Hickey, P. C., S. R. Swift, M. G. Roca & N. D. Read. 2004. Live-cell Imaging of Filamentous Fungi Using Vital Fluorescent Dyes and Confocal Microscopy. In *Methods in Microbiology*, 63-87. Academic Press.

Hipp, S., Y. T. Tai, D. Blanset, P. Deegen, J. Wahl, O. Thomas, B. Rattel, P. J. Adam, K. C. Anderson & M. Friedrich (2017) A novel BCMA/CD3 bispecific T-cell engager for the treatment of multiple myeloma induces selective lysis in vitro and in vivo. *Leukemia,* 31**,** 1743-1751.

Hoare, A., P. Timms, P. M. Bavoil & D. P. Wilson (2008) Spatial constraints within the chlamydial host cell inclusion predict interrupted development and persistence. *BMC Microbiol,* 8**,** 5.

Hu, Y. S., H. Cang & B. F. Lillemeier (2016) Superresolution imaging reveals nanometer- and micrometer-scale spatial distributions of T-cell receptors in lymph nodes. *Proceedings of the National Academy of Sciences,* 113**,** 7201-7206.

Huang, B., J. Li, J. Liu & J. Gu (2016) CD20-positive multiple myeloma: can conventional chemotherapy still be used to achieve ideal outcome for these patients? *Leuk Lymphoma,* 57**,** 335-340.

Huisken, J. & D. Y. Stainier (2009) Selective plane illumination microscopy techniques in developmental biology. *Development,* 136**,** 1963-75.

Hussain, A. F., P. A. Heppenstall, F. Kampmeier, I. Meinhold-Heerlein & S. Barth (2019) One-step site-specific antibody fragment auto-conjugation using SNAP-tag technology. *Nature Protocols,* 14**,** 3101-3125.

Hybiske, K. & R. S. Stephens (2007) Mechanisms of host cell exit by the intracellular bacterium Chlamydia. *Proc Natl Acad Sci U S A,* 104**,** 11430-5.

Imai, C., K. Mihara, M. Andreansky, I. C. Nicholson, C. H. Pui, T. L. Geiger & D. Campana (2004) Chimeric receptors with 4-1BB signaling capacity provoke potent cytotoxicity against acute lymphoblastic leukemia. *Leukemia,* 18**,** 676-84.

Kahane, S., B. Dvoskin, M. Mathias & M. G. Friedman (2001) Infection of Acanthamoeba polyphaga with Simkania negevensis and S. negevensis survival within amoebal cysts. *Appl Environ Microbiol,* 67**,** 4789-95.

Kahmann, R. & J. Kämper (2004) Ustilago maydis: how its biology relates to pathogenic development. *New Phytologist,* 164**,** 31-42.

Kalra, A. P., P. Kar, J. Preto, V. Rezania, A. Dogariu, J. D. Lewis, J. A. Tuszynski & K. Shankar (2019) Behavior of α, β tubulin in DMSO-containing electrolytes. *Nanoscale Advances,* 1**,** 3364-3371.

Kaur, G. & J. M. Dufour (2012) Cell lines: Valuable tools or useless artifacts. *Spermatogenesis,* 2**,** 1-5.

Kim, D. & K. Park (2004) Swelling and mechanical properties of superporous hydrogels of poly(acrylamide-co-acrylic acid)/polyethylenimine interpenetrating polymer networks. *Polymer,* 45**,** 189-196.

Knaus, H., G. A. Blab, G. Jerre van Veluw, H. C. Gerritsen & H. A. B. Wösten (2013) Label-free fluorescence microscopy in fungi. *Fungal Biology Reviews,* 27**,** 60-66.

Koch-Edelmann, S., S. Banhart, E. M. Saied, L. Rose, L. Aeberhard, M. Laue, J. Doellinger, C. Arenz & D. Heuer (2017) The cellular ceramide transport protein CERT promotes Chlamydia psittaci infection and controls bacterial sphingolipid uptake. *Cell Microbiol,* 19.

Kochenderfer, J. N., M. E. Dudley, S. H. Kassim, R. P. T. Somerville, R. O. Carpenter, M. Stetler-Stevenson, J. C. Yang, G. Q. Phan, M. S. Hughes, R. M. Sherry, M. Raffeld, S. Feldman, L. Lu, Y. F. Li, L. T. Ngo, A. Goy, T. Feldman, D. E. Spaner, M. L. Wang, C. C. Chen, S. M. Kranick, A. Nath, D.-A. N. Nathan, K. E. Morton, M. A. Toomey & S. A. Rosenberg (2015) Chemotherapy-refractory diffuse large B-cell lymphoma and indolent B-cell malignancies can be effectively treated with autologous T cells expressing an anti-CD19 chimeric antigen receptor. *Journal of clinical oncology : official journal of the American Society of Clinical Oncology,* 33**,** 540-549.

Kolb, H. C., M. G. Finn & K. B. Sharpless (2001) Click Chemistry: Diverse Chemical Function from a Few Good Reactions. *Angew Chem Int Ed Engl,* 40**,** 2004-2021.

Kononova, O., Y. Kholodov, K. E. Theisen, K. A. Marx, R. I. Dima, F. I. Ataullakhanov, E. L. Grishchuk & V. Barsegov (2014) Tubulin Bond Energies and Microtubule Biomechanics Determined from Nanoindentation in Silico. *Journal of the American Chemical Society,* 136**,** 17036-17045.

Kraft, M. L. (2016) Sphingolipid Organization in the Plasma Membrane and the Mechanisms That Influence It. *Front Cell Dev Biol,* 4**,** 154.

Kromm, D. T., T.; Wittbrodt, J. , (2016) Chapter 5 - An eye on light-sheet microscopy. *Methods in Cell Biology,* 133**,**, 105-123.

Ku, T., J. Swaney, J. Y. Park, A. Albanese, E. Murray, J. H. Cho, Y. G. Park, V. Mangena, J. Chen & K. Chung (2016) Multiplexed and scalable super-resolution imaging of three-dimensional protein localization in size-adjustable tissues. *Nat Biotechnol,* 34**,** 973-81.

Kuerschner, L., C. S. Ejsing, K. Ekroos, A. Shevchenko, K. I. Anderson & C. Thiele (2005) Polyene-lipids: a new tool to image lipids. *Nat Methods,* 2**,** 39-45.

Kunz, T. C., R. Gotz, M. Sauer & T. Rudel (2019) Detection of Chlamydia Developmental Forms and Secreted Effectors by Expansion Microscopy. *Front Cell Infect Microbiol,* 9**,** 276.

Kunz, T. C. & V. Kozjak-Pavlovic (2019) Diverse Facets of Sphingolipid Involvement in Bacterial Infections. *Front Cell Dev Biol,* 7**,** 203.

Kuzuya, A., K. Numajiri, M. Kimura & M. Komiyama (2008) Single-molecule accommodation of streptavidin in nanometer-scale wells formed in DNA nanostructures. *Nucleic Acids Symp Ser (Oxf)***,** 681-2.

Lakowicz, J. R. 2006. *Principles of fluorescence spectroscopy*. New York: Springer.

Lampe, A., V. Haucke, S. J. Sigrist, M. Heilemann & J. Schmoranzer (2012) Multi-colour direct STORM with red emitting carbocyanines. *Biol Cell,* 104**,** 229-37.

Lampe, A., G. Tadeus & J. Schmoranzer (2015) Spectral demixing avoids registration errors and reduces noise in multicolor localization-based super-resolution microscopy. *Methods Appl Fluoresc,* 3**,** 034006.

Lange, L. (2014) The importance of fungi and mycology for addressing major global challenges*. *IMA Fungus,* 5**,** 463-71.

Lanver, D., M. Tollot, G. Schweizer, L. Lo Presti, S. Reissmann, L. S. Ma, M. Schuster, S. Tanaka, L. Liang, N. Ludwig & R. Kahmann (2017) Ustilago maydis effectors and their impact on virulence. *Nat Rev Microbiol,* 15**,** 409-421.

Latge, J. P. & G. Chamilos (2019) Aspergillus fumigatus and Aspergillosis in 2019. *Clin Microbiol Rev,* 33.

Le Negrate, G., A. Krieg, B. Faustin, M. Loeffler, A. Godzik, S. Krajewski & J. C. Reed (2008) ChlaDub1 of Chlamydia trachomatis suppresses NF-kappaB activation and inhibits IkappaBalpha ubiquitination and degradation. *Cell Microbiol,* 10**,** 1879-92.

Lee, J. K., G. A. Enciso, D. Boassa, C. N. Chander, T. H. Lou, S. S. Pairawan, M. C. Guo, F. Y. M. Wan, M. H. Ellisman, C. Sutterlin & M. Tan (2018) Replication-dependent size reduction precedes differentiation in Chlamydia trachomatis. *Nat Commun,* 9**,** 45.

Legant, W. R., L. Shao, J. B. Grimm, T. A. Brown, D. E. Milkie, B. B. Avants, L. D. Lavis & E. Betzig (2016) High-density three-dimensional localization microscopy across large volumes. *Nat Methods,* 13**,** 359-65.

Lehmann, M., G. Lichtner, H. Klenz & J. Schmoranzer (2016) Novel organic dyes for multicolor localization-based super-resolution microscopy. *J Biophotonics,* 9**,** 161-70.

Leonard, C. A., R. V. Schoborg, N. Low, M. Unemo & N. Borel (2019) Pathogenic Interplay Between Chlamydia trachomatis and Neisseria gonorrhoeae that Influences Management and Control Efforts—More Questions than Answers? *Current Clinical Microbiology Reports,* 6**,** 182-191.

Lesage, G. & H. Bussey (2006) Cell wall assembly in Saccharomyces cerevisiae. *Microbiol Mol Biol Rev,* 70**,** 317-43.

Li, D., Y. Tang, J. Lin & W. Cai (2017) Methods for genetic transformation of filamentous fungi. *Microb Cell Fact,* 16**,** 168.

Li, K., G. Li, F. Xiao, F. Lu, Z. Wang & A. Xu (2012) Unidirectionally optical coupling from free space into silicon waveguide with wide flat-top angular efficiency. *Opt Express,* 20**,** 18545-54.

Li, X. C. & M. H. Sayegh (2007) CD28: beyond just T-cell costimulation. *Blood,* 109**,** 2668-2669.

Lieberman, D., B. Dvoskin, D. Lieberman, S. Kahane & M. Friedman (2002) Serological Evidence of Acute Infection with the Chlamydia-Like Microorganism Simkania negevensis (Z) in Acute Exacerbation of Chronic Obstructive Pulmonary Disease. *European Journal of Clinical Microbiology and Infectious Diseases,* 21**,** 307-309.

Liebisch, P., S. Eppinger, C. Schopflin, G. Stehle, G. Munzert, H. Dohner & M. Schmid (2005) CD44v6, a target for novel antibody treatment approaches, is frequently expressed in multiple myeloma and associated with deletion of chromosome arm 13q. *Haematologica,* 90**,** 489.

Lillemeier, B. F., M. A. Mortelmaier, M. B. Forstner, J. B. Huppa, J. T. Groves & M. M. Davis (2010) TCR and Lat are expressed on separate protein islands on T cell membranes and concatenate during activation. *Nat Immunol,* 11**,** 90-6.

Lim, Y., A. L. Shiver, M. Khariton, K. M. Lane, K. M. Ng, S. R. Bray, J. Qin, K. C. Huang & B. Wang (2019) Mechanically resolved imaging of bacteria using expansion microscopy. *PLoS Biol,* 17**,** e3000268.

Lin, P., R. Owens, G. Tricot & C. S. Wilson (2004) Flow cytometric immunophenotypic analysis of 306 cases of multiple myeloma. *Am J Clin Pathol,* 121**,** 482-8.

Lonial, S., B. M. Weiss, S. Z. Usmani, S. Singhal, A. Chari, N. J. Bahlis, A. Belch, A. Krishnan, R. A. Vescio, M. V. Mateos, A. Mazumder, R. Z. Orlowski, H. J. Sutherland, J. Blade, E. C. Scott, A. Oriol, J. Berdeja, M. Gharibo, D. A. Stevens, R. LeBlanc, M. Sebag, N. Callander, A. Jakubowiak, D. White, J. de la Rubia, P. G. Richardson, S. Lisby, H. Feng, C. M. Uhlar, I. Khan, T. Ahmadi & P. M. Voorhees (2016) Daratumumab monotherapy in patients with treatment-refractory multiple myeloma (SIRIUS): an open-label, randomised, phase 2 trial. *Lancet,* 387**,** 1551-1560.

Los, G. V., L. P. Encell, M. G. McDougall, D. D. Hartzell, N. Karassina, C. Zimprich, M. G. Wood, R. Learish, R. F. Ohana, M. Urh, D. Simpson, J. Mendez, K. Zimmerman, P. Otto, G. Vidugiris, J. Zhu, A. Darzins, D. H. Klaubert, R. F. Bulleit & K. V. Wood (2008) HaloTag: a novel protein labeling technology for cell imaging and protein analysis. *ACS Chem Biol,* 3**,** 373-82.

Löschberger, A., C. Franke, G. Krohne, S. van de Linde & M. Sauer (2014) Correlative super-resolution fluorescence and electron microscopy of the nuclear pore complex with molecular resolution. *J Cell Sci,* 127**,** 4351-5.

Maher, J., R. J. Brentjens, G. Gunset, I. Riviere & M. Sadelain (2002) Human T-lymphocyte cytotoxicity and proliferation directed by a single chimeric TCRzeta /CD28 receptor. *Nat Biotechnol,* 20**,** 70-5.

Majeti, R., Z. Xu, T. G. Parslow, J. L. Olson, D. I. Daikh, N. Killeen & A. Weiss (2000) An inactivating point mutation in the inhibitory wedge of CD45 causes lymphoproliferation and autoimmunity. *Cell,* 103**,** 1059-70.

Mehlitz, A., K. Karunakaran, J. A. Herweg, G. Krohne, S. van de Linde, E. Rieck, M. Sauer & T. Rudel (2014) The chlamydial organism Simkania negevensis forms ER vacuole contact sites and inhibits ER-stress. *Cell Microbiol,* 16**,** 1224-43.

Merkwirth, C. & T. Langer (2009) Prohibitin function within mitochondria: Essential roles for cell proliferation and cristae morphogenesis. *Biochimica et Biophysica Acta (BBA) - Molecular Cell Research,* 1793**,** 27-32.

Meyer, V., M. R. Andersen, A. A. Brakhage, G. H. Braus, M. X. Caddick, T. C. Cairns, R. P. de Vries, T. Haarmann, K. Hansen, C. Hertz-Fowler, S. Krappmann, U. H. Mortensen, M. A. Penalva, A. F. J. Ram & R. M. Head (2016) Current challenges of research on filamentous fungi in relation to human welfare and a sustainable bio-economy: a white paper. *Fungal Biol Biotechnol,* 3**,** 6.

Michie, M. S., R. Gotz, C. Franke, M. Bowler, N. Kumari, V. Magidson, M. Levitus, J. Loncarek, M. Sauer & M. J. Schnermann (2017) Cyanine Conformational Restraint in the Far-Red Range. *J Am Chem Soc,* 139**,** 12406-12409.

Michielse, C. B. & M. Rep (2009) Pathogen profile update: Fusarium oxysporum. *Mol Plant Pathol,* 10**,** 311-24.

Migneault, I., C. Dartiguenave, M. J. Bertrand & K. C. Waldron (2004) Glutaraldehyde: behavior in aqueous solution, reaction with proteins, and application to enzyme crosslinking. *BioTechniques,* 37**,** 790-802.

Moore, E. R. & S. P. Ouellette (2014) Reconceptualizing the chlamydial inclusion as a pathogen-specified parasitic organelle: an expanded role for Inc proteins. *Front Cell Infect Microbiol,* 4**,** 157.

Morgan, R. A. (2013) Risky business: target choice in adoptive cell therapy. *Blood,* 122**,** 3392-4.

Mosser, D. M. & J. P. Edwards (2008) Exploring the full spectrum of macrophage activation. *Nat Rev Immunol,* 8**,** 958-69.

Mukherjee, S., H. Raghuraman, S. Dasgupta & A. Chattopadhyay (2004) Organization and dynamics of N-(7-nitrobenz-2-oxa-1,3-diazol-4-yl)-labeled lipids: a fluorescence approach. *Chem Phys Lipids,* 127**,** 91-101.

Murray, A. J., S. J. Lewis, A. N. Barclay & R. L. Brady (1995) One sequence, two folds: a metastable structure of CD2. *Proc Natl Acad Sci U S A,* 92**,** 7337-41.

Nans, A., M. Kudryashev, H. R. Saibil & R. D. Hayward (2015) Structure of a bacterial type III secretion system in contact with a host membrane in situ. *Nat Commun,* 6**,** 10114.

Nassiri, F., M. D. Cusimano, B. W. Scheithauer, F. Rotondo, A. Fazio, G. M. Yousef, L. V. Syro, K. Kovacs & R. V. Lloyd (2011) Endoglin (CD105): a review of its role in angiogenesis and tumor diagnosis, progression and therapy. *Anticancer Res,* 31**,** 2283-90.

Nerreter, T., S. Letschert, R. Gotz, S. Doose, S. Danhof, H. Einsele, M. Sauer & M. Hudecek (2019) Super-resolution microscopy reveals ultra-low CD19 expression on myeloma cells that triggers elimination by CD19 CAR-T. *Nat Commun,* 10**,** 3137.

Neubert, F., G. Beliu, U. Terpitz, C. Werner, C. Geis, M. Sauer & S. Doose (2018) Bioorthogonal Click Chemistry Enables Site-specific Fluorescence Labeling of Functional NMDA Receptors for Super-Resolution Imaging. *Angew Chem Int Ed Engl,* 57**,** 16364-16369.

Nijhof, I. S., T. Casneuf, J. van Velzen, B. van Kessel, A. E. Axel, K. Syed, R. W. Groen, M. van Duin, P. Sonneveld, M. C. Minnema, S. Zweegman, C. Chiu, A. C. Bloem, T. Mutis, H. M. Lokhorst, A. K. Sasser & N. W. van de Donk (2016) CD38 expression and complement inhibitors affect response and resistance to daratumumab therapy in myeloma. *Blood,* 128**,** 959-70.

Nijhof, I. S., R. W. Groen, H. M. Lokhorst, B. van Kessel, A. C. Bloem, J. van Velzen, R. de Jong-Korlaar, H. Yuan, W. A. Noort, S. K. Klein, A. C. Martens, P. Doshi, K. Sasser, T. Mutis & N. W. van de Donk (2015) Upregulation of CD38 expression on multiple myeloma cells by all-trans retinoic acid improves the efficacy of daratumumab. *Leukemia,* 29**,** 2039-49.

Nir, G., I. Farabella, C. Pérez Estrada, C. G. Ebeling, B. J. Beliveau, H. M. Sasaki, S. D. Lee, S. C. Nguyen, R. B. McCole, S. Chattoraj, J. Erceg, J. AlHaj Abed, N. M. C. Martins, H. Q. Nguyen, M. A. Hannan, S. Russell, N. C. Durand, S. S. P. Rao, J. Y. Kishi, P. Soler-Vila, M. Di Pierro, J. N. Onuchic, S. P. Callahan, J. M. Schreiner, J. A. Stuckey, P. Yin, E. L. Aiden, M. A. Marti-Renom & C. t. Wu (2018) Walking along chromosomes with super-resolution imaging, contact maps, and integrative modeling. *PLOS Genetics,* 14**,** e1007872.

Orakdogen, N. & O. Okay (2006) Correlation between crosslinking efficiency and spatial inhomogeneity in poly(acrylamide) hydrogels. *Polymer Bulletin,* 57**,** 631-641.

Ortoneda, M., J. Guarro, M. P. Madrid, Z. Caracuel, M. I. G. Roncero, E. Mayayo & A. Di Pietro (2004) Fusarium oxysporum as a multihost model for the genetic dissection of fungal virulence in plants and mammals. *Infection and immunity,* 72**,** 1760-1766.

Osherov, N. & O. Yarden. 2010. The Cell Wall of Filamentous Fungi. In *Cellular and Molecular Biology of Filamentous Fungi.* American Society of Microbiology.

Pal, R. R., A. K. Baidya, G. Mamou, S. Bhattacharya, Y. Socol, S. Kobi, N. Katsowich, S. Ben-Yehuda & I. Rosenshine (2019) Pathogenic E. coli Extracts Nutrients from Infected Host Cells Utilizing Injectisome Components. *Cell,* 177**,** 683-696 e18.

Palumbo, A., A. Chanan-Khan, K. Weisel, A. K. Nooka, T. Masszi, M. Beksac, I. Spicka, V. Hungria, M. Munder, M. V. Mateos, T. M. Mark, M. Qi, J. Schecter, H. Amin, X. Qin, W. Deraedt, T. Ahmadi, A. Spencer, P. Sonneveld & C. Investigators (2016) Daratumumab, Bortezomib, and Dexamethasone for Multiple Myeloma. *N Engl J Med,* 375**,** 754-66.

Pan, C., C. Kumar, S. Bohl, U. Klingmueller & M. Mann (2009) Comparative Proteomic Phenotyping of Cell Lines and Primary Cells to Assess Preservation of Cell Type-specific Functions. *Molecular &amp; Cellular Proteomics,* 8**,** 443.

Panzer, S., A. Brych, A. Batschauer & U. Terpitz (2019) Opsin 1 and Opsin 2 of the Corn Smut Fungus Ustilago maydis Are Green Light-Driven Proton Pumps. *Front Microbiol,* 10**,** 735.

Park, H.-E., D. Choi, J. S. Park, C. Sim, S. Park, S. Kang, H. Yim, M. Lee, J. Kim, J. Pac, K. Rhee, J. Lee, Y. Lee, Y. Lee & S.-Y. Kim (2019) Scalable and Isotropic Expansion of Tissues with Simply Tunable Expansion Ratio. *Advanced Science,* 6**,** 1901673.

Patton, M. J., S. McCorrister, C. Grant, G. Westmacott, R. Fariss, P. Hu, K. Zhao, M. Blake, B. Whitmire, C. Yang, H. D. Caldwell & G. McClarty (2016) Chlamydial Protease-Like Activity Factor and Type III Secreted Effectors Cooperate in Inhibition of p65 Nuclear Translocation. *mBio,* 7.

Pawelec, G., A. Borowitz, P. H. Krammer & P. Wernet (1982) Constitutive interleukin 2 production by the JURKAT human leukemic T cell line. *Eur J Immunol,* 12**,** 387-92.

Peberdy, J. F. (1979) Fungal Protoplasts: Isolation, Reversion, and Fusion. *Annual Review of Microbiology,* 33**,** 21-39.

Pehlivan, K. C., B. B. Duncan & D. W. Lee (2018) CAR-T Cell Therapy for Acute Lymphoblastic Leukemia: Transforming the Treatment of Relapsed and Refractory Disease. *Current Hematologic Malignancy Reports,* 13**,** 396-406.

Perez-Villar, J. J., G. S. Whitney, M. A. Bowen, D. H. Hewgill, A. A. Aruffo & S. B. Kanner (1999) CD5 negatively regulates the T-cell antigen receptor signal transduction pathway: involvement of SH2-containing phosphotyrosine phosphatase SHP-1. *Mol Cell Biol,* 19**,** 2903-12.

Pierpont, T. M., C. B. Limper & K. L. Richards (2018) Past, Present, and Future of Rituximab-The World's First Oncology Monoclonal Antibody Therapy. *Front Oncol,* 8**,** 163.

Pinaud, F., X. Michalet, L. A. Bentolila, J. M. Tsay, S. Doose, J. J. Li, G. Iyer & S. Weiss (2006) Advances in fluorescence imaging with quantum dot bio-probes. *Biomaterials,* 27**,** 1679-1687.

Plesner, T. & J. Krejcik (2018) Daratumumab for the Treatment of Multiple Myeloma. *Frontiers in immunology,* 9**,** 1228-1228.

Prommersberger, S., H. Jetani, S. Danhof, R. Monjezi, T. Nerreter, J. Beckmann, H. Einsele & M. Hudecek (2018) Novel targets and technologies for CAR-T cells in multiple myeloma and acute myeloid leukemia. *Curr Res Transl Med,* 66**,** 37-38.

Pruneda, J. N., R. J. Bastidas, E. Bertsoulaki, K. N. Swatek, B. Santhanam, M. J. Clague, R. H. Valdivia, S. Urbe & D. Komander (2018) A Chlamydia effector combining deubiquitination and acetylation activities induces Golgi fragmentation. *Nat Microbiol,* 3**,** 1377-1384.

Ramamoorthy, V., L. Govindaraj, M. Dhanasekaran, S. Vetrivel, K. K. Kumar & E. Ebenezar (2015) Combination of driselase and lysing enzyme in one molar potassium chloride is effective for the production of protoplasts from germinated conidia of Fusarium verticillioides. *J Microbiol Methods,* 111**,** 127-34.

Rank, R. G. 2009. Chapter 44 - Chlamydia. In *Vaccines for Biodefense and Emerging and Neglected Diseases,* eds. A. D. T. Barrett & L. R. Stanberry, 845-867. London: Academic Press.

Rayleigh, L. (1903) On the Theory of Optical Images, with special reference to the Microscope. *Journal of the Royal Microscopical Society,* 23**,** 474-482.

Reilly, M. C. & T. L. Doering. 2010. Chapter 22 - Biosynthesis of fungal and yeast glycans. In *Microbial Glycobiology,* eds. O. Holst, P. J. Brennan, M. v. Itzstein & A. P. Moran, 393-412. San Diego: Academic Press.

Revelo, N. H., D. Kamin, S. Truckenbrodt, A. B. Wong, K. Reuter-Jessen, E. Reisinger, T. Moser & S. O. Rizzoli (2014) A new probe for super-resolution imaging of membranes elucidates trafficking pathways. *J Cell Biol,* 205**,** 591-606.

Riedl, J., A. H. Crevenna, K. Kessenbrock, J. H. Yu, D. Neukirchen, M. Bista, F. Bradke, D. Jenne, T. A. Holak, Z. Werb, M. Sixt & R. Wedlich-Soldner (2008) Lifeact: a versatile marker to visualize F-actin. *Nat Methods,* 5**,** 605-7.

Risso, A., D. Smilovich, M. C. Capra, I. Baldissarro, G. Yan, A. Bargellesi & M. E. Cosulich (1991) CD69 in resting and activated T lymphocytes. Its association with a GTP binding protein and biochemical requirements for its expression. *J Immunol,* 146**,** 4105-14.

Rossboth, B., A. M. Arnold, H. Ta, R. Platzer, F. Kellner, J. B. Huppa, M. Brameshuber, F. Baumgart & G. J. Schutz (2018) TCRs are randomly distributed on the plasma membrane of resting antigen-experienced T cells. *Nat Immunol,* 19**,** 821-827.

Rossy, J., S. V. Pageon, D. M. Davis & K. Gaus (2013) Super-resolution microscopy of the immunological synapse. *Curr Opin Immunol,* 25**,** 307-12.

Ruiz-Roldan, M. C., M. Kohli, M. I. Roncero, P. Philippsen, A. Di Pietro & E. A. Espeso (2010) Nuclear dynamics during germination, conidiation, and hyphal fusion of Fusarium oxysporum. *Eukaryot Cell,* 9**,** 1216-24.

Saka, H. A. & R. H. Valdivia (2010) Acquisition of nutrients by Chlamydiae: unique challenges of living in an intracellular compartment. *Current opinion in microbiology,* 13**,** 4-10.

Sakai, T., T. Matsunaga, Y. Yamamoto, C. Ito, R. Yoshida, S. Suzuki, N. Sasaki, M. Shibayama & U.-i. Chung (2008) Design and Fabrication of a High-Strength Hydrogel with Ideally Homogeneous Network Structure from Tetrahedron-like Macromonomers. *Macromolecules,* 41**,** 5379-5384.

Sauer, L., K. M. Andersen, C. Dysli, M. S. Zinkernagel, P. S. Bernstein & M. Hammer (2018) Review of clinical approaches in fluorescence lifetime imaging ophthalmoscopy. *J Biomed Opt,* 23**,** 1-20.

Sauer, M. & M. Heilemann (2017) Single-Molecule Localization Microscopy in Eukaryotes. *Chem Rev,* 117**,** 7478-7509.

Schafer, P., S. van de Linde, J. Lehmann, M. Sauer & S. Doose (2013) Methylene blue- and thiol-based oxygen depletion for super-resolution imaging. *Anal Chem,* 85**,** 3393-400.

Schermelleh, L., A. Ferrand, T. Huser, C. Eggeling, M. Sauer, O. Biehlmaier & G. P. C. Drummen (2019) Super-resolution microscopy demystified. *Nat Cell Biol,* 21**,** 72-84.

Schindelin, J., I. Arganda-Carreras, E. Frise, V. Kaynig, M. Longair, T. Pietzsch, S. Preibisch, C. Rueden, S. Saalfeld, B. Schmid, J. Y. Tinevez, D. J. White, V. Hartenstein, K. Eliceiri, P. Tomancak & A. Cardona (2012) Fiji: an open-source platform for biological-image analysis. *Nat Methods,* 9**,** 676-82.

Schmidt-Weber, C. B., M. Letarte, S. Kunzmann, B. Rückert, C. Bernabéu & K. Blaser (2005) TGF-β signaling of human T cells is modulated by the ancillary TGF-β receptor endoglin. *International Immunology,* 17**,** 921-930.

Schubert, E., A. Koos, T. Emrich, A. Züfle, K. A. Schmid & A. Zimek (2015) A framework for clustering uncertain data. *Proc. VLDB Endow.,* 8**,** 1976–1979.

Schubert, E., J. Sander, M. Ester, H. P. Kriegel & X. Xu (2017) DBSCAN Revisited, Revisited: Why and How You Should (Still) Use DBSCAN. *ACM Trans. Database Syst.,* 42**,** Article 19.

Schubert, W., B. Bonnekoh, A. J. Pommer, L. Philipsen, R. Bockelmann, Y. Malykh, H. Gollnick, M. Friedenberger, M. Bode & A. W. Dress (2006) Analyzing proteome topology and function by automated multidimensional fluorescence microscopy. *Nat Biotechnol,* 24**,** 1270-8.

Schueder, F., M. T. Strauss, D. Hoerl, J. Schnitzbauer, T. Schlichthaerle, S. Strauss, P. Yin, H. Harz, H. Leonhardt & R. Jungmann (2017) Universal Super-Resolution Multiplexing by DNA Exchange. *Angew Chem Int Ed Engl,* 56**,** 4052-4055.

Schuh, E., K. Berer, M. Mulazzani, K. Feil, I. Meinl, H. Lahm, M. Krane, R. Lange, K. Pfannes, M. Subklewe, R. Gurkov, M. Bradl, R. Hohlfeld, T. Kumpfel, E. Meinl & M. Krumholz (2016) Features of Human CD3+CD20+ T Cells. *J Immunol,* 197**,** 1111-7.

Scitovski, R. & K. Sabo (2019) DBSCAN-like clustering method for various data densities. *Pattern Analysis and Applications.*

Seckinger, A., J. A. Delgado, S. Moser, L. Moreno, B. Neuber, A. Grab, S. Lipp, J. Merino, F. Prosper, M. Emde, C. Delon, M. Latzko, R. Gianotti, R. Luoend, R. Murr, R. J. Hosse, L. J. Harnisch, M. Bacac, T. Fauti, C. Klein, A. Zabaleta, J. Hillengass, E. A. Cavalcanti-Adam, A. D. Ho, M. Hundemer, J. F. San Miguel, K. Strein, P. Umana, D. Hose, B. Paiva & M. D. Vu (2017) Target Expression, Generation, Preclinical Activity, and Pharmacokinetics of the BCMA-T Cell Bispecific Antibody EM801 for Multiple Myeloma Treatment. *Cancer Cell,* 31**,** 396-410.

Sherman, E., V. Barr, S. Manley, G. Patterson, L. Balagopalan, I. Akpan, C. K. Regan, R. K. Merrill, C. L. Sommers, J. Lippincott-Schwartz & L. E. Samelson (2011) Functional nanoscale organization of signaling molecules downstream of the T cell antigen receptor. *Immunity,* 35**,** 705-20.

Shimomura, O., F. H. Johnson & Y. Saiga (1962) Extraction, purification and properties of aequorin, a bioluminescent protein from the luminous hydromedusan, Aequorea. *J Cell Comp Physiol,* 59**,** 223-39.

Simons, K. & M. J. Gerl (2010) Revitalizing membrane rafts: new tools and insights. *Nat Rev Mol Cell Biol,* 11**,** 688-99.

Sletten, E. M. & C. R. Bertozzi (2009) Bioorthogonal chemistry: fishing for selectivity in a sea of functionality. *Angew Chem Int Ed Engl,* 48**,** 6974-98.

Smith-Garvin, J. E., G. A. Koretzky & M. S. Jordan (2009) T cell activation. *Annu Rev Immunol,* 27**,** 591-619.

Snavely, E. A., M. Kokes, J. D. Dunn, H. A. Saka, B. D. Nguyen, R. J. Bastidas, D. G. McCafferty & R. H. Valdivia (2014) Reassessing the role of the secreted protease CPAF in Chlamydia trachomatis infection through genetic approaches. *Pathog Dis,* 71**,** 336-51.

Stanly, T. A., M. Fritzsche, S. Banerji, E. Garcia, J. Bernardino de la Serna, D. G. Jackson & C. Eggeling (2016) Critical importance of appropriate fixation conditions for faithful imaging of receptor microclusters. *Biol Open,* 5**,** 1343-50.

Stashenko, P., L. M. Nadler, R. Hardy & S. F. Schlossman (1980) Characterization of a human B lymphocyte-specific antigen. *J Immunol,* 125**,** 1678-85.

Stelzer, E. H. (2015) Light-sheet fluorescence microscopy for quantitative biology. *Nat Methods,* 12**,** 23-6.

Szaszák, M., P. Steven, K. Shima, R. Orzekowsky-Schröder, G. Hüttmann, I. R. König, W. Solbach & J. Rupp (2011) Fluorescence Lifetime Imaging Unravels C. trachomatis Metabolism and Its Crosstalk with the Host Cell. *PLOS Pathogens,* 7**,** e1002108.

Tan, Y. H., M. Liu, B. Nolting, J. G. Go, J. Gervay-Hague & G. Y. Liu (2008) A nanoengineering approach for investigation and regulation of protein immobilization. *ACS Nano,* 2**,** 2374-84.

Tanaka, K. A., K. G. Suzuki, Y. M. Shirai, S. T. Shibutani, M. S. Miyahara, H. Tsuboi, M. Yahara, A. Yoshimura, S. Mayor, T. K. Fujiwara & A. Kusumi (2010) Membrane molecules mobile even after chemical fixation. *Nat Methods,* 7**,** 865-6.

Terpitz, U., S. Letschert, U. Bonda, C. Spahn, C. Guan, M. Sauer, U. Zimmermann, E. Bamberg, D. Zimmermann & V. L. Sukhorukov (2012) Dielectric Analysis and Multi-cell Electrofusion of the Yeast Pichia pastoris for Electrophysiological Studies. *The Journal of Membrane Biology,* 245**,** 815-826.

Tettamanti, G., R. Bassi, P. Viani & L. Riboni (2003) Salvage pathways in glycosphingolipid metabolism. *Biochimie,* 85**,** 423-37.

Tillberg, P. W., F. Chen, K. D. Piatkevich, Y. Zhao, C. C. Yu, B. P. English, L. Gao, A. Martorell, H. J. Suk, F. Yoshida, E. M. DeGennaro, D. H. Roossien, G. Gong, U. Seneviratne, S. R. Tannenbaum, R. Desimone, D. Cai & E. S. Boyden (2016) Protein-retention expansion microscopy of cells and tissues labeled using standard fluorescent proteins and antibodies. *Nat Biotechnol,* 34**,** 987-92.

Truckenbrodt, S., M. Maidorn, D. Crzan, H. Wildhagen, S. Kabatas & S. O. Rizzoli (2018) X10 expansion microscopy enables 25-nm resolution on conventional microscopes. *EMBO Rep,* 19.

Truckenbrodt, S., C. Sommer, S. O. Rizzoli & J. G. Danzl (2019) A practical guide to optimization in X10 expansion microscopy. *Nat Protoc,* 14**,** 832-863.

Truneh, A. & P. Machy (1987) Detection of very low receptor numbers on cells by flow cytometry using a sensitive staining method. *Cytometry,* 8**,** 562-567.

Turtle, C. J., L. A. Hanafi, C. Berger, M. Hudecek, B. Pender, E. Robinson, R. Hawkins, C. Chaney, S. Cherian, X. Chen, L. Soma, B. Wood, D. Li, S. Heimfeld, S. R. Riddell & D. G. Maloney (2016) Immunotherapy of non-Hodgkin's lymphoma with a defined ratio of CD8+ and CD4+ CD19-specific chimeric antigen receptor-modified T cells. *Sci Transl Med,* 8**,** 355ra116.

Uno, S. N., M. Kamiya, T. Yoshihara, K. Sugawara, K. Okabe, M. C. Tarhan, H. Fujita, T. Funatsu, Y. Okada, S. Tobita & Y. Urano (2014) A spontaneously blinking fluorophore based on intramolecular spirocyclization for live-cell super-resolution imaging. *Nat Chem,* 6**,** 681-9.

Valley, C. C., S. Liu, D. S. Lidke & K. A. Lidke (2015) Sequential superresolution imaging of multiple targets using a single fluorophore. *PLoS One,* 10**,** e0123941.

van de Linde, S., S. Aufmkolk, C. Franke, T. Holm, T. Klein, A. Löschberger, S. Proppert, S. Wolter & M. Sauer (2013) Investigating cellular structures at the nanoscale with organic fluorophores. *Chem Biol,* 20**,** 8-18.

van de Linde, S., A. Löschberger, T. Klein, M. Heidbreder, S. Wolter, M. Heilemann & M. Sauer (2011) Direct stochastic optical reconstruction microscopy with standard fluorescent probes. *Nat Protoc,* 6**,** 991-1009.

van de Veerdonk, F. L., M. S. Gresnigt, L. Romani, M. G. Netea & J. P. Latge (2017) Aspergillus fumigatus morphology and dynamic host interactions. *Nat Rev Microbiol,* 15**,** 661-674.

Verdaasdonk, J. S., A. D. Stephens, J. Haase & K. Bloom (2014) Bending the rules: widefield microscopy and the Abbe limit of resolution. *Journal of cellular physiology,* 229**,** 132-138.

Vogl, D. T., N. Raje, S. Jagannath, P. Richardson, P. Hari, R. Orlowski, J. G. Supko, D. Tamang, M. Yang, S. S. Jones, C. Wheeler, R. J. Markelewicz & S. Lonial (2017) Ricolinostat, the First Selective Histone Deacetylase 6 Inhibitor, in Combination with Bortezomib and Dexamethasone for Relapsed or Refractory Multiple Myeloma. *Clin Cancer Res,* 23**,** 3307-3315.

Vollmeister, E., K. Schipper, S. Baumann, C. Haag, T. Pohlmann, J. Stock & M. Feldbrügge (2012) Fungal development of the plant pathogen Ustilago maydis. *FEMS Microbiology Reviews,* 36**,** 59-77.

Wäldchen, F., J. Schlegel, R. Götz, M. Luciano, M. Schnermann, S. Doose & M. Sauer (2020) Whole-cell imaging of plasma membrane receptors by 3D lattice light-sheet dSTORM. *Nature Communications,* 11**,** 887.

Walter, T., L. Collenburg, L. Japtok, B. Kleuser, S. Schneider-Schaulies, N. Muller, J. Becam, A. Schubert-Unkmeir, J. N. Kong, E. Bieberich & J. Seibel (2016) Incorporation and visualization of azido-functionalized N-oleoyl serinol in Jurkat cells, mouse brain astrocytes, 3T3 fibroblasts and human brain microvascular endothelial cells. *Chem Commun (Camb),* 52**,** 8612-8614.

Walter, T., J. Schlegel, A. Burgert, A. Kurz, J. Seibel & M. Sauer (2017) Incorporation studies of clickable ceramides in Jurkat cell plasma membranes. *Chem Commun (Camb),* 53**,** 6836-6839.

Warman, N. M. & E. A. B. Aitken (2018) The Movement of Fusarium oxysporum f.sp. cubense (Sub-Tropical Race 4) in Susceptible Cultivars of Banana. *Front Plant Sci,* 9**,** 1748.

Wegel, E., A. Gohler, B. C. Lagerholm, A. Wainman, S. Uphoff, R. Kaufmann & I. M. Dobbie (2016) Imaging cellular structures in super-resolution with SIM, STED and Localisation Microscopy: A practical comparison. *Sci Rep,* 6**,** 27290.

Wei, J., X. Han, J. Bo & W. Han (2019) Target selection for CAR-T therapy. *J Hematol Oncol,* 12**,** 62.

Weston, P. D. & S. Avrameas (1971) Proteins coupled to polyacrylamide beads using glutaraldehyde. *Biochemical and Biophysical Research Communications,* 45**,** 1574-1580.

Wilson, D. P., P. Timms, D. L. McElwain & P. M. Bavoil (2006) Type III secretion, contact-dependent model for the intracellular development of chlamydia. *Bull Math Biol,* 68**,** 161-78.

Wolter, S., A. Loschberger, T. Holm, S. Aufmkolk, M. C. Dabauvalle, S. van de Linde & M. Sauer (2012) rapidSTORM: accurate, fast open-source software for localization microscopy. *Nat Methods,* 9**,** 1040-1.

Wyrick, P. B. (2010) Chlamydia trachomatis persistence in vitro: an overview. *The Journal of infectious diseases,* 201 Suppl 2**,** S88-S95.

Xu, H., Z. Tong, Q. Ye, T. Sun, Z. Hong, L. Zhang, A. Bortnick, S. Cho, P. Beuzer, J. Axelrod, Q. Hu, M. Wang, S. M. Evans, C. Murre, L. F. Lu, S. Sun, K. D. Corbett & H. Cang (2019) Molecular organization of mammalian meiotic chromosome axis revealed by expansion STORM microscopy. *Proc Natl Acad Sci U S A,* 116**,** 18423-18428.

Yakovian, O., R. Schwarzer, J. Sajman, Y. Neve-Oz, Y. Razvag, A. Herrmann & E. Sherman (2018) Gp41 dynamically interacts with the TCR in the immune synapse and promotes early T cell activation. *Sci Rep,* 8**,** 9747.

Yanez, L., M. Sanchez-Escamilla & M. A. Perales (2019) CAR T Cell Toxicity: Current Management and Future Directions. *Hemasphere,* 3**,** e186.

Yavasoglu, I., G. Sargin, G. Kadikoylu, F. K. Doger & Z. Bolaman (2015) Immunohistochemical evaluation of CD20 expression in patients with multiple myeloma. *Rev Bras Hematol Hemoter,* 37**,** 34-7.

Yi, J., A. Manna, V. A. Barr, J. Hong, K. C. Neuman & L. E. Samelson (2016) madSTORM: a superresolution technique for large-scale multiplexing at single-molecule accuracy. *Mol Biol Cell,* 27**,** 3591-3600.

Yu, C., J. Tang, A. Loredo, Y. Chen, S. Y. Jung, A. Jain, A. Gordon & H. Xiao (2018) Proximity-Induced Site-Specific Antibody Conjugation. *Bioconjugate Chemistry,* 29**,** 3522-3526.

Zamoyska, R. (2007) Why is there so much CD45 on T cells? *Immunity,* 27**,** 421-3.

Zeidan, Y. H. & Y. A. Hannun (2007) Translational aspects of sphingolipid metabolism. *Trends Mol Med,* 13**,** 327-36.

Zhang, M., H. Chang, Y. Zhang, J. Yu, L. Wu, W. Ji, J. Chen, B. Liu, J. Lu, Y. Liu, J. Zhang, P. Xu & T. Xu (2012) Rational design of true monomeric and bright photoactivatable fluorescent proteins. *Nat Methods,* 9**,** 727-9.

Ziegler, S., E. Weiss, A.-L. Schmitt, J. Schlegel, A. Burgert, U. Terpitz, M. Sauer, L. Moretta, S. Sivori, I. Leonhardt, O. Kurzai, H. Einsele & J. Loeffler (2017) CD56 Is a Pathogen Recognition Receptor on Human Natural Killer Cells. *Scientific Reports,* 7**,** 6138.

Zola, H. (2004) High-sensitivity immunofluorescence/flow cytometry: detection of cytokine receptors and other low-abundance membrane molecules. *Curr Protoc Cytom,* Chapter 6**,** Unit 6 3.

Curriculum Vitae

Ralph Götz

Martin-Luther-Str.1, 97072 Würzburg, Germany

+49 931 454 60 897. +49 172 991 89 14 (mobile)

ralph.goetz@uni-wuerzburg.de

Education

Since 10/2016: **PhD-Thesis:**	**PhD-student**, Julius Maximilians University, Würzburg, Germany Super-resolution microscopy of plasma membrane receptors and intracellular pathogens
Since 10/2016:	**Member of the graduate school of life sciences**, Julius Maximilians University, Würzburg, Germany
04/2016 – 07/2016: **Project:**	**ERASMUS-Fellowship**, Institute Curie, Paris, France Evaluation of a BRCA2 mutant in cytokinesis
10/2014 – 03/2016: **Master Thesis:**	**Master of Science in biology** (with distinction; second best degree of all students), Julius Maximilians University Würzburg, Germany Influences of Förster resonance energy transfer on super-resolution microscopy (awarded as outstanding Master Thesis)
10/2011 – 09/2014: **Bachelor Thesis:**	**Bachelor of Science in biology**, Julius Maximilians University Würzburg, Germany Characterization of *Xmrk*-expressing melanocytes and evaluation of candidate genes in *Xmrk*-expressing fish
10/2001 – 07/2010:	**High school Wilhelm Hausenstein**, Munich, Germany

Acknowledgements

A special thanks goes to Patrick Eiring and Alexander Kuhlemann who had to tolerate my mood after thousands of not working experiments. I am really happy that I had the privilege to be in the Sauerlab during my thesis.

I would also like to thank my whole family for their everlasting support in every possible way. Thank you, I could always rely on you!

I also consider myself very fortunate to have my wonderful wife Milena (still sounds crazy). Thank you for all your love, support, patience, understanding and listening to all my ideas and problems.

Affidavit

I hereby confirm that my thesis entitled "Super-resolution microscopy of plasma membrane receptors and intracellular pathogens" is the result of my own work. I did not receive any help or support from commercial consultants. All sources and / or materials applied are listed and specified in the thesis.

Furthermore, I confirm that this thesis has not yet been submitted as part of another examination process neither in identical nor in similar form.

Place, Date   Signature

Eidesstattliche Erklärung

Hiermit erkläre ich an Eides statt, die Dissertation „Hochauflösende Mikroskopie von Plasmamembran Rezeptoren und intrazellulären Pathogenen" eigenständig, d.h. insbesondere selbständig und ohne Hilfe eines kommerziellen Promotionsberaters, angefertigt und keine anderen als die von mir angegebenen Quellen und Hilfsmittel verwendet zu haben.

Ich erkläre außerdem, dass die Dissertation weder in gleicher noch in ähnlicher Form bereits in einem anderen Prüfungsverfahren vorgelegen hat.

Ort, Datum   Unterschrift